Toward a better understanding and control of polyurethane composite films behavior for actuators

Yan Zhang

To cite this version:

Yan Zhang. Toward a better understanding and control of polyurethane composite films behavior for actuators. Materials. Université de Lyon, 2021. English. NNT : 2021LYSEI025 . tel-03433375

HAL Id: tel-03433375
https://theses.hal.science/tel-03433375
Submitted on 17 Nov 2021

N°d'ordre NNT : 2021LYSEI025

THESE de DOCTORAT DE L'UNIVERSITE DE LYON
opérée au sein de
l'Institut National des Sciences Appliquées de Lyon

Ecole Doctorale N° ED162
Mécanique, Energétique, Génie Civil, Acoustique

Spécialité / discipline de doctorat : Acoustique

Soutenue publiquement le 29/04/2021, par :

Yan ZHANG

Toward a better understanding and control of polyurethane composite films behavior for actuators

Devant le jury composé de :

CAVAILLE Jean-Yves	Professeur des Universités INSA Lyon	Président
PAPET Philippe	Professeur des Universités Université de Montpellier	Rapporteur
GUIFFARD Benoit	Professeur des Universités Université de Nantes	Rapporteur
BARRAU Sophie	Maître de Conférences, Université de Lille	Examinatrice
LEBRUN Laurent	Professeur des Universités INSA Lyon	Directeur de thèse
SEVEYRAT Laurence	Docteur, Ingénieur de Recherche INSA Lyon	Co-directrice de thèse

Département FEDORA – INSA Lyon - Ecoles Doctorales

SIGLE	ECOLE DOCTORALE	NOM ET COORDONNEES DU RESPONSABLE
CHIMIE	**CHIMIE DE LYON** **https://www.edchimie-lyon.fr** Sec. : Renée EL MELHEM Bât. Blaise PASCAL, 3e étage secretariat@edchimie-lyon.fr	**M. Stéphane DANIELE** C2P2-CPE LYON-UMR 5265 Bâtiment F308, BP 2077 43 Boulevard du 11 novembre 1918 69616 Villeurbanne **directeur@edchimie-lyon.fr**
E.E.A.	**ÉLECTRONIQUE, ÉLECTROTECHNIQUE, AUTOMATIQUE** **https://edeea.universite-lyon.fr** Sec. : Stéphanie CAUVIN Bâtiment Direction INSA Lyon Tél : 04.72.43.71.70 secretariat.edeea@insa-lyon.fr	**M. Philippe DELACHARTRE** INSA LYON Laboratoire CREATIS Bâtiment Blaise Pascal, 7 avenue Jean Capelle 69621 Villeurbanne CEDEX Tél : 04.72.43.88.63 **philippe.delachartre@insa-lyon.fr**
E2M2	**ÉVOLUTION, ÉCOSYSTÈME, MICROBIOLOGIE, MODÉLISATION** **http://e2m2.universite-lyon.fr** Sec. : Sylvie ROBERJOT Bât. Atrium, UCB Lyon 1 Tél : 04.72.44.83.62 secretariat.e2m2@univ-lyon1.fr	**M. Philippe NORMAND** Université Claude Bernard Lyon 1 UMR 5557 Lab. d'Ecologie Microbienne Bâtiment Mendel 43, boulevard du 11 Novembre 1918 69 622 Villeurbanne CEDEX **philippe.normand@univ-lyon1.fr**
EDISS	**INTERDISCIPLINAIRE SCIENCES-SANTÉ** **http://ediss.universite-lyon.fr** Sec. : Sylvie ROBERJOT Bât. Atrium, UCB Lyon 1 Tél : 04.72.44.83.62 secretariat.ediss@univ-lyon1.fr	**Mme Sylvie RICARD-BLUM** Institut de Chimie et Biochimie Moléculaires et Supramoléculaires (ICBMS) - UMR 5246 CNRS - Université Lyon 1 Bâtiment Raulin - 2ème étage Nord 43 Boulevard du 11 novembre 1918 69622 Villeurbanne Cedex Tél : +33(0)4 72 44 82 32 **sylvie.ricard-blum@univ-lyon1.fr**
INFOMATHS	**INFORMATIQUE ET MATHÉMATIQUES** **http://edinfomaths.universite-lyon.fr** Sec. : Renée EL MELHEM Bât. Blaise PASCAL, 3e étage Tél : 04.72.43.80.46 infomaths@univ-lyon1.fr	**M. Hamamache KHEDDOUCI** Université Claude Bernard Lyon 1 Bât. Nautibus 43, Boulevard du 11 novembre 1918 69 622 Villeurbanne Cedex France Tél : 04.72.44.83.69 **hamamache.kheddouci@univ-lyon1.fr**
Matériaux	**MATÉRIAUX DE LYON** **http://ed34.universite-lyon.fr** Sec. : Yann DE ORDENANA Tél : 04.72.18.62.44 yann.de-ordenana@ec-lyon.fr	**M. Stéphane BENAYOUN** Ecole Centrale de Lyon Laboratoire LTDS 36 avenue Guy de Collongue 69134 Ecully CEDEX Tél : 04.72.18.64.37 **stephane.benayoun@ec-lyon.fr**
MEGA	**MÉCANIQUE, ÉNERGÉTIQUE, GÉNIE CIVIL, ACOUSTIQUE** **http://edmega.universite-lyon.fr** Sec. : Stéphanie CAUVIN Tél : 04.72.43.71.70 Bâtiment Direction INSA Lyon mega@insa-lyon.fr	**M. Jocelyn BONJOUR** INSA Lyon Laboratoire CETHIL Bâtiment Sadi-Carnot 9, rue de la Physique 69621 Villeurbanne CEDEX **jocelyn.bonjour@insa-lyon.fr**
ScSo	**ScSo*** **https://edsciencessociales.universite-lyon.fr** Sec. : Mélina FAVETON INSA : J.Y. TOUSSAINT Tél : 04.78.69.77.79 melina.faveton@univ-lyon2.fr	**M. Christian MONTES** Université Lumière Lyon 2 86 Rue Pasteur 69365 Lyon CEDEX 07 **christian.montes@univ-lyon2.fr**

*ScSo : Histoire, Géographie, Aménagement, Urbanisme, Archéologie, Science politique, Sociologie, Anthropologie

To all the great teachers and nice friends who appear in my life

I. Acknowledgement

The past 42 months made an important and unforgettable journey in my life, in terms of not only research but also the building of my inner spirit. I wish to take this opportunity to express my appreciation to all the people who have contributed to the success of this thesis, as well as to my French experience.

I have to send acknowledgments firstly to my thesis advisor, Prof. Laurent LEBRUN. The logic he follows to analyze the scientific issues, as well as the honesty and caution he insists to make scientific explanations, have had a significant influence on my thought process and my research approach. I sincerely thank him for the knowledge he taught and the scientific ideas he brought, in addition to the efforts he made to encourage me by making compliments to my work.

I could not express enough my gratitude to Dr. Laurence SEVEYRAT, my co-advisor. Her devotion of time on teaching and supervising me has ensured the achievement of this thesis. I thank her for her endless patience throughout the whole thesis, in showing me the experimental techniques, helping me on results analysis and correcting the manuscript. I also thank her for her care of my feelings. I have learned a lot from her discipline and self-organization that help to manage many mission at the same time, and I admire her “super power” to catch every detail in one sight.

I would like also to thank warmly the rest of the jury members: Dr. Sophie BARRAU, Prof. Jean-Yves CAVAILLE, Prof. Benoit GUIFFARD and Prof. Philippe PAPET, for their detailed reviews, valuable questions and interesting discussions, which helped to improve the quality of this thesis.

I wish to thank Prof. Laurent LEBRUN and Dr. Jean-Fabien CAPSAL for accepting me as the candidate of this thesis. I also wish to thank China Scholarship Council (CSC) for their financial support during my phD studies.

A special thanks to Ms. Véronique Perrin, engineer in the technical group, who has much contributed to the characterization techniques and numerical works of this thesis. She is always reliable and ready to help when I faced difficulties.

My appreciation to Dr. Gildas COATIVY and Prof. Claude RICHARD for the exchanges on the experimental strategies and techniques, which have inspired part of the work in this thesis. My thanks as well to Prof. Lionel PETIT and Prof. Michaël LALLART for the short but straightforward discussions we had.

My thanks to Mr. Frédéric DEFROMERIE, the technician in LGEF, for the masks he made and the French practice he gave. I could neither forget my gratitude to Ms. Evelyne DORIEUX, our excellent and elegant secretary, for her efficient help in the complicate administrative tasks, also for her kindness and friendship.

The warm and diverse ambience in LGEF makes it such a special laboratory more than only a working place. I appreciate the nice time we spent together at the home of Laurence & Francis, Quyen & Pierre-Jean, Véronique, David, Lijuan & Michaël, Benjamin & Vilma. My thanks also to Mama Zina for her delicious meals and her supports.

I am particularly grateful to the nice colleagues and friends, who have made this period a beautiful journey in my life. Thanks to Thomas for the cultural exchange, the French help in administration stuff and the beer time. Thanks to Francesco and Foamie, my electroactive gang who never stop talking and singing, for taking care of my feelings, sharing the stories and bringing me to friends. I feel the room is full when they are there. Not to forget the gratitude to my sweet friend Annalisa and Ong for embracing me with the endless kindness and love in their hearts. Thanks to Bhaawan, my most handsome Indian guy, and to Giulia, my funny and beautiful Italian girl, for your suggestions, also for the wine and talks together. Thanks also to my Chinese gang: Ziyin, Xiaoting and Yunayuan for the delicious food, games and karaoke together; to Hiba, Amaury, Giulia, Omar for the unforgettable time we spent together. I wish to spend more time with these great friends.

I take the chance to express my gratitude to my friend Yijian, who has always provided her "blind" confidence on me and always tries to convince me that I could achieve everything. Thanks also to Zhiheng, Yijun (Tortoise) and Chengeng (Elephant) for their accompany and encouragement during my thesis writing.

Finally yet importantly, my gratefulness with love to my family, who have been providing their unconditional support, trying to take care of me with their method throughout my life. Their love have allowed me to grow up to who I am today.

Again, my acknowledgement to all the great teachers and nice friends who came and will come to my life, I will become a better person thanks to you.

II. Résumé

Les polymères électroactifs (EAPs) trouvent de nombreuses applications en tant qu'actionneurs souples, compte tenu de leur légèreté, de grandes déformations sous champ électrique et de la facilité d'être élaborés sous diverses formes. Parmi les EAPs diélectriques, le polyuréthane est intéressant, de par ses propriétés diélectriques et mécaniques, un faible coût et des propriétés modulables via la composition et l'incorporation de charges.

Les travaux de recherche décrits dans cette thèse ont pour objectif une meilleure compréhension et un meilleur contrôle du comportement de films composites à base de polyuréthane.

La mesure du couplage mécanique est délicate et complexe. Une large gamme de valeurs du coefficient électromécanique, s'étalant sur plusieurs décades, est présentée pour le polyuréthane dans la littérature. Avec deux techniques de mesures (bancs de mesure développés au laboratoire) et des simulations Comsol, il a été obtenu des valeurs de coefficients sur une gamme beaucoup plus réduite, et indiquant un rôle considérable du mécanisme de Maxwell par rapport au phénomène d'électrostriction.

Des conditions d'élaboration et de mesures bien contrôlées sont importantes, en termes notamment de taux d'humidité et de niveaux de champs électriques.

Une étude a ensuite été menée sur le rôle des nanocharges sur les propriétés de composites polyuréthane / nanoplaquettes de graphène fonctionnalisé oxygène. Une augmentation de la constante diélectrique et un faible renforcement mécanique ont été obtenus, mais la performance électromécanique n'est pas améliorée. Les raisons possibles de ces résultats discordants ont été examinées avec des analyses multi-échelles. Une attention particulière a été portée sur les mécanismes de conduction et sur les polarisations dipolaires et interfaciale de type Maxwell Wagner Sillars. La faible performance peut venir de l'adhésion modérée entre le polymère et le graphène, mais aussi de la compétition entre l'augmentation de la constante diélectrique et la diminution du champ électrique réellement vu par le polymère.

Mots-clés

Polymère électro-actifs, Polyuréthane, Graphène fonctionnalisé, Couplage électromécanique, Propriété électrique, Nanocomposites, Spectroscopie diélectrique.

III. Abstract

The applications of electroactive polymers (EAPs) as soft actuators are numerous due to their lightweight, large electric field-induced deformation, and easy preparation in various shapes. Among dielectric EAPs, the polyurethane (PU) is a promising candidate due to its dielectric and mechanical properties, low cost, and tunable properties through composition control and incorporation of fillers.

Research described in this thesis aims at a better understanding and control of polyurethane composites films behavior.

Measuring the electromechanical coupling is delicate and complex. A wide range over several decades of the electromechanical coefficient values can be found in the literature for the polyurethane. With the help of two measuring technologies (lab-built benches) and Comsol simulations, it was firstly obtained a limited range for the coefficient values, and proved a substantial role of the Maxwell mechanism in relation to the electrostriction phenomenon.

Well-controlled elaboration and measuring conditions are of prime importance, in terms of, for instance, humidity and electric fields levels.

An investigation of the role of the nanofillers on the properties of oxygen-functionalized graphene nanoplatelets / polyurethane composites was then carried out. A large increase in dielectric constant and a slight mechanical reinforcement were obtained, whereas there was no improvement in electromechanical performance. The possible reasons for these discordant results were thus investigated using multiscale studies. Specific attention was paid on the role of the conduction mechanism and the dipolar and Maxwell Wagner Sillars interfacial polarizations. The discrepancy could be due to the moderate adhesion between the polymer and the graphene nanoplatelets, but also to the competition between the increased dielectric constant and the decreased electric field value seen by the polymer.

Key words

Electroactive polymers, Polyurethane, Functionalized graphene, Electromechanical coupling, Electrical properties, Nanocomposites, Dielectric spectroscopy.

IV. Résumé de mémoire

Introduction

Compte tenu de leur légèreté, leur flexibilité, leur facilité d'élaboration sous différentes tailles et formes et leur grande déformation sous champ électrique, les polymères électroactifs (EAPs) sont considérés comme une bonne alternative aux céramiques piézoélectriques ou aux alliages à mémoire de forme pour les actionneurs flexibles. La recherche sur les EAPs s'est intensifiée au cours des 20 dernières années.

Les EAPs peuvent être divisés en deux familles, à savoir les EAPs ioniques et les EAPs électroniques. Les premiers présentent l'avantage de grandes déformations, de faibles niveaux de champs électriques, une bonne biocompatibilité, ils sont utilisés dans l'administration de médicaments, les micro-pompes, etc. Cependant, ils sont limités par une faible force, une courte durée de vie et la nécessité d'un environnement humide. Les EAPs électroniques, tels que les polymères piézoélectriques et diélectriques, présentent une large gamme de déformations et de forces bloquées. De plus, leurs réponses électromécaniques sont considérées comme rapides. Les EAP électroniques sont donc plutôt utilisés dans la robotique mimétique, les pinces souples, etc.

Parmi les EAPs électroniques, le polyuréthane thermoplastique (PU) est un matériau prometteur. Avec une structure spécifique alliant des segments rigides et des segments souples, le PU présente une permittivité électrique élevée par rapport aux autres élastomères diélectriques. Il montre également de bonnes performances en termes de déformations et de forces bloquées, un faible coût et il est facilement disponible sur le marché.

L'utilisation des EAPs électroniques nécessite toutefois l'application d'un champ électrique élevé. Des efforts considérables ont été faits pour améliorer l'efficacité du couplage électromécanique de manière à diminuer le niveau de ce champ. Le coefficient de couplage électromécanique augmente avec la permittivité diélectrique et diminue avec le module élastique des EAP. L'incorporation de charges conductrices est un moyen possible d'augmenter la permittivité. Les charges nanométriques à grande surface spécifique telles que les nanotubes ou le graphène sont d'un grand intérêt. Cette thèse portera sur les nanoplaquettes de graphène fonctionnalisé à l'oxygène (OFG) incorporées dans la matrice de polyuréthane.

La motivation de cette thèse est d'aller vers une meilleure compréhension du comportement des films composites à base de polyuréthane, afin d'obtenir un meilleur contrôle des performances d'actionnement. Bien que de nombreuses études aient été menées, l'origine de la déformation induite par le champ reste controversée, et avec différents types de méthodes de caractérisation appliquées, les valeurs rapportées du coefficient électromécanique montrent une grande dispersion. Deuxièmement, des recherches détaillées sur le rôle des charges sur les propriétés macroscopiques des composites font parfois défaut dans la littérature. L'objectif de cette thèse est donc d'apporter des réponses aux deux questions suivantes : est-ce le phénomène d’électrostriction ou le mécanisme de Maxwell qui est responsable de la déformation induite par le champ électrique ? Et quel est le rôle des nanocharges sur les propriétés des nanocomposites?

Le chapitre 1 présente l’état de l’art

Nous présentons d’abord quelques généralités sur les actionneurs. Un actionneur est un dispositif qui transforme l’énergie qui lui est fournie en une action mécanique. L’énergie peut être électrique, magnétique, thermique, pneumatique ou encore hydraulique. Parmi les actionneurs utilisant l’énergie électrique, les polymères électro-actifs (EAPs) offrent de nombreux avantages tels que la flexibilité, de larges déformations et une facilité de fabrication sous différentes formes.

Les deux grandes familles d’EAP sont les EAPs électroniques et les EAPs ioniques. Les caractéristiques notables, plusieurs exemples de matériaux et d’applications sont présentés pour les 2 familles.

Avec d’autres polymères tels que les silicones, les acrylates, le PVDF et ses copolymères…, le polyuréthane fait partie des EAPs électroniques qui contrairement aux polymères ioniques doivent être soumis à un champ électrique.

Les polyuréthanes sont généralement issus de la réaction d’isocyanates avec des alcools. De par leur structure et la composition des monomères qui les constituent présentent une séparation de phases due à l’immiscibilité des segments rigides (SR) et des segments souples (SS). Une large gamme possible de propriétés peut être obtenue en jouant sur la nature des monomères segments, la longueur des segments rigides, la masse molaire des segments souples… Des liaisons hydrogènes venant lier les SR et les SS en plus des liaisons covalentes jouent aussi un rôle important dans la microséparation de phases et donc dans les propriétés.

Les mécanismes de polarisation dans un polymère diélectrique tel que le polyuréthane sont les suivants :

La polarisation électronique est due au déplacement et à la déformation des nuages électroniques qui sont décentrés par rapport aux noyaux des atomes. Ces deux mécanismes de polarisation sont très rapides. La polarisation dipolaire ou d'orientation se produit dans les polymères contenant des molécules avec des moments dipolaires permanents. La polarisation interfaciale a lieu dans des matériaux hétérogènes, ayant des phases de permittivité différente, conduisant à une accumulation de charges aux interfaces.

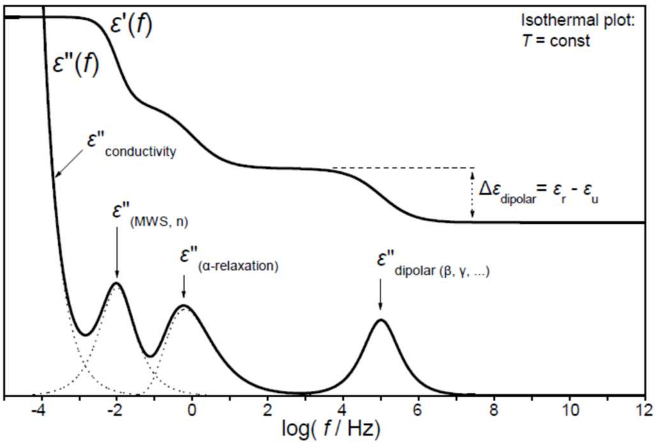

Fig. IV.1. Représentation schématique de la dépendance en fréquence de ε’ et ε, montrant les pics de conductivité et de relaxations diélectriques relatives aux mécanismes de polarisation

L’étude de la permittivité diélectrique en fonction de la fréquence permet d’étudier ces mécanismes de polarisation. Le modèle d’Havriliak Negami a été utilisé pour l’étude des relaxations. Les temps de relaxation dépendent de la température, ils peuvent suivre une loi d’Arrhénius ou une loi non-linéaire de type Vogel-Fulcher-Tamman (VTF).

La conductivité est étudiée aussi sur la gamme de Fréquence ; elle suit la loi phénoménologique de Jonscher ; l’étude de la partie continue (σ_{DC}) et la valeur des coefficients de la loi renseignent sur le mécanisme de transports de charges qui peut être de type électronique ou de type ionique.

La déformation montre une dépendance quadratique avec le champ électrique appliqué. L’origine de cette déformation reste controversée dans la littérature pour le polyuréthane ; il est possible de trouver des valeurs de coefficients électromécaniques M_{33} ou M_{31} s’étalant entre 10^{-19} et 10^{-13} m^2 M^{-2}. Certains auteurs affirment que le mécanisme prépondérant est lié à l’effet électrostatique de Maxwell (attraction coulombienne entre les électrodes) alors que d’autres indiquent que le plus important est le phénomène d’électrostriction, phénomène intrinsèque dépendant des variations de propriétés diélectriques.

La déformation sous champ électrique dépendant des propriétés diélectriques, une voie possible d’amélioration des performances d’actionnement est d’augmenter la permittivité. C’est possible par exemple par l’incorporation de nanocharges conductrices. Le fait d’utiliser des nanocharges fonctionnalisées permettra d’améliorer la dispersion dans la matrice polymère.

Le chapitre 2 décrit les matériaux et méthodes utilisés dans la thèse.

La première partie est consacrée à la description des matériaux et des techniques de fabrication des films composites.

Le polyurethane utilisé est fourni par la société Lubrizol (référence Estane 58887 NAT038). Les segments rigides sont constitués de MDI (diisocyanate de diphénylméthane) et de l'allongeur de chaines BDO (butane 1 diol) et les segments souples de PTMO (oxyde de polytetraméthylène). Ce polymère industriel contient aussi des additifs de nature inconnue.

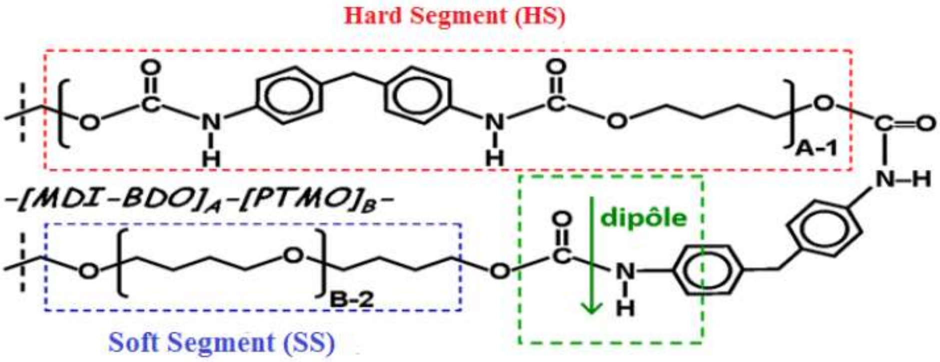

Fig. IV.2. Composition des segments durs et souples du polyuréthane Estane 58887 NAT038

Les nanocharges utilisées sont des nanoplaquettes de graphène fonctionnalisées par plasma (fonctionnalisation oxygène et azote), de taille comprise entre 0.3 et 5 µm et d'épaisseur inférieure à 50 nm. Des composites ont aussi été élaborés avec des particules de $BaTiO_3$ de diamètre moyen 500 nm.

Les films sont réalisés par voie solvant. La dispersion des charges dans le solvant DMF se fait à l'aide d'une sonde à ultra-sons (Hielscher UP400S) et l'ensemble est mélangé à la solution de polyuréthane (granules préalablement dissous dans le DMF) dans un dispositif de chauffage à reflux (température : 80°C). Les films sont déposés à l'aide d'un applicateur de films puis subissent un recuit à 60°C pendant 20 h suivi d'un second traitement à 125°C pendant 3 heures. L'épaisseur finale des films est d'environ 100 µm.

Les films sont ensuite découpés en diverses formes et dimensions selon le type de caractérisations ; et pour certaines d'entre elles, les échantillons sont recouverts d'un dépôt conducteur d'or par pulvérisation cathodique (Cressington HR208) d'épaisseur d'environ 25 nm.

La seconde partie du chapitre décrit les outils de caractérisation.

La microscopie Electronique à Balayage est utilisée pour observer la distribution des charges dans les composites. 2 microscopes ont été utilisés : Zeiss Supra 55 VP et Hitachi Flex SEM 1000.

La calorimétrie différentielle à balayage apporte des informations sur la microstructure du polymère. L'appareil utilisé est le DSC 131evo de Setaram. Les échantillons placés dans des creusets en aluminium, sont refroidis à 120°C puis chauffés à 220°C avant d'être refroidis, avec des vitesses de 10°C/min.

Les modules d'Young Y ont été déterminés à partir des courbes contrainte/déformation. Les expérimentations sont réalisées à l'aide d'une table de translation Newport, équipée d'un micro-contrôleur de déplacement XPS et d'un capteur de force (Doerler Mesures LC102TC).

Les propriétés électriques (permittivité diélectrique ε, facteur de pertes, conductivité σ…) sont analysées par spectrométrie diélectrique, par l'analyseur d'impédance Schlumberger Solartron 1255 et l'interface diélectrique 1296, sur la gamme de fréquences 0.1-1 MHz. Les mesures en température ont été effectuées dans un cryostat (Optistat DN2 oxford instrument) relié au contrôleur de température Oxford ITC503. La permittivité a aussi été mesurée à haut niveau de champ électrique avec le même ensemble et un amplificateur de tension Trek 10/10B.

Les mesures de déformation sous champ électrique permettant de déterminer le coefficient électromécanique M_{31} ont été réalisées par 2 méthodes. La première est la méthode dite « bender » : le polymère électrodé est collé sur un substrat. Il est clampé d'un côté et libre de l'autre. Il est soumis à un champ électrique qui provoque un fléchissement de l'ensemble. Le déplacement est mesuré en bout de poutre par un capteur laser (3RG7056-3CM00-PF Pepperl+Fuchs). A partir du déplacement et d'un facteur prenant en compte la géométrie du système et les propiétés des matériaux, la déformation S_{31} est calculée. permettant d'accéder au coefficient M_{31}.

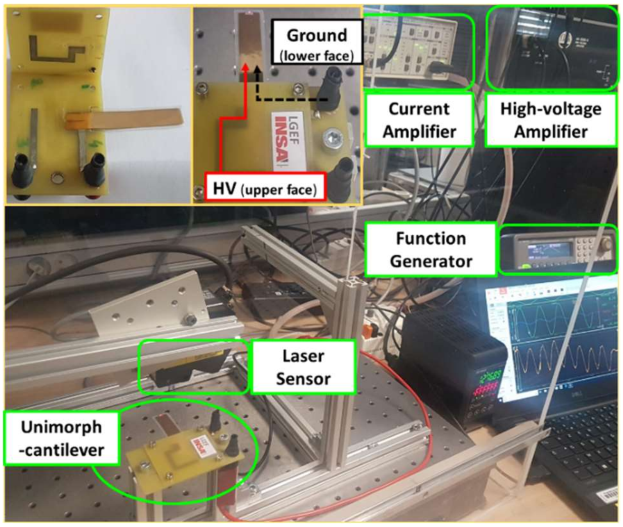

Fig. IV.3. Photographies du banc de mesure de déformation sous champ électrique par la méthode Bender

La seconde est la méthode dite « strain-stress ». C'est le même banc de mesure que celui utilisé pour la mesure du module d'Young. Les déformations sont déterminées avec et sans champ électrique. La différence permet d'accéder au S_{31}. Le coefficient M_{31} est ensuite calculé par l'équation : $S_{31} = M_{31}E^2$.

Certaines caractérisations ont été effectuées sous différents taux d'humidité, obtenus avec l'utilisation de solutions salines dans des enceintes entourant les bancs de mesures.

Le chapitre 3 traite du couplage électromécanique dans le polyuréthane.

Dans la littérature, les coefficients électromécaniques du polyuréthane présentent de grandes disparités, avec des valeurs s'étalant entre 10^{-19} et 10^{-13} m^2 V^{-2}, et très différentes selon le type de mesures utilisé. L'origine du mécanisme de déformation sous champ électrique reste ainsi controversée : plusieurs auteurs affirment que le mécanisme est dû à l'attraction électrostatique des charges libres entre les électrodes, alors que d'autres indiquent que l'électrostriction est le phénomène prépondérant.

Il est donc primordial de disposer d'une méthode de mesure fiable. Dans ce chapitre, 2 méthodes sont proposées pour la détermination du coefficient M_{31} : la méthode « Bender » et la méthode « strain/stress » (ou contrainte/déformation).

Dans la méthode « bender », le film de polyuréthane électrodé est collé sur un substrat puis soumis à un champ électrique. La mesure de déplacement est effectuée par un capteur laser en bout de poutre, à 0.1 et 1Hz, loin de la fréquence de résonance de l'ensemble déterminée par élément fini (Comsol).

La déformation S_{31} est calculée à partir du déplacement et d'un facteur dépendant des propriétés physiques des 2 couches considérées. Elle est proportionnelle au carré du champ électrique. Les sources d'incertitude liées à la détermination de ces propriétés sont analysées, ainsi que l'influence de divers paramètres tels que la nature et l'épaisseur du substrat ou encore l'épaisseur de l'électrode d'or. En tenant compte de la dispersion obtenue sur les mesures expérimentales de déflection et les incertitudes sur les paramètres utilisés dans le K_{DS}, le coefficient M_{31} varie entre 0.5 et 2.3 × 10^{-18} m^2 V^{-2}, ce qui est plus précis que la gamme rapportée dans la littérature.

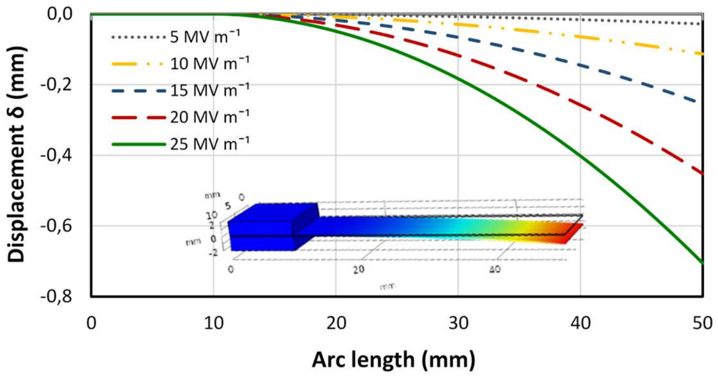

Fig. IV.4. Déflection simulée selon de la poutre constituée du polymère collé sur un substrat, pour des champs électriques variant entre 5 et 25 MV m^{-1}

Dans la méthode « strain-stress », le film polymère, soumis à de faibles niveaux de contraintes, se déforme linéairement. C'est le principe de mesure du module d'Young. La déformation S_{31} correspond à l'écart entre l'écart entre la déformation sans champ électrique et celle avec champ électrique. Le coefficient M_{31} obtenu varie entre 0.6 et 1.5 × 10^{-18} m^2 V^{-2}. Cette méthode est un plus simple à mettre en œuvre puisqu'elle ne nécessite pas le collage sur un substrat mais la mesure des déformations pour les faibles valeurs de champs électriques est moins précise.

Les déformations mesurées avec les 2 types de méthodes ont été comparées aux déformations de Maxwell simulées par Comsol avec l'utilisation de la physique « forces électromécaniques ». Elles sont dans la même gamme de valeurs indiquant que le mécanisme de Maxwell joue un rôle considérable dans le couplage électromécanique.

Table.IV.1. Coefficients électromécaniques obtenus à partir des méthodes Bender et strain-stress, et calculés à partir de la contribution de Maxwell.

	M_{31}* (m^2 V^{-2})
Bender method	**0.5–2.3 × 10^{-18}**
Strain-stress method	**0.6–1.5 × 10^{-18}**
Maxwell contribution	**0.4–1.3 × 10^{-18}**

Les M_{31} expérimentaux ont des valeurs comprises entre 0.5 et 2.3 10^{-18} m^2 V^{-2}, ce qui est plus précis que la gamme de valeurs reportée dans la littérature (10^{-19} à 10^{-13} m^2 V^{-2}). Pour augmenter encore la précision, la prochaine étape est de déterminer les propriétés diélectriques et mécaniques sous haut niveau de champ électrique, pour être plus proche des conditions de fonctionnement des actionneurs.

Le chapitre 4 traite de l'origine de la dispersion de la performance électromécanique du polyuréthane.

La performance électromécanique dépend du ratio constante diélectrique sur module d'Young. Si le module d'Young ne varie pas avec le champ électrique, ce n'est pas le cas de la permittivité. L'objectif du chapitre est d'étudier les propriétés électriques sous champ. On s'est aussi aperçu pendant la thèse que le procédé d'élaboration et les conditions de mesure en termes de température et d'humidité pouvaient avoir une influence sur les propriétés. C'est l'objet de la seconde partie du chapitre.

Le polyuréthane présente une valeur de permittivité plus forte à haut champ électrique qu'à bas niveau, ce qui peut expliquer la sous-estimation de M_{31} par le modèle électrostatique du chapitre 3. À champ électrique élevé, la valeur de permittivité est sensible à plusieurs facteurs, notamment les formes et la force du champ électrique, la période de mesure, le procédé d'élaboration, l'humidité et la température. Cette sensibilité explique l'origine de la dispersion du M_{31}, et confirme l'importance de mesurer les propriétés diélectriques des EAP dans les mêmes conditions que celles utilisées pour la mesure du couplage électro-mécanique.

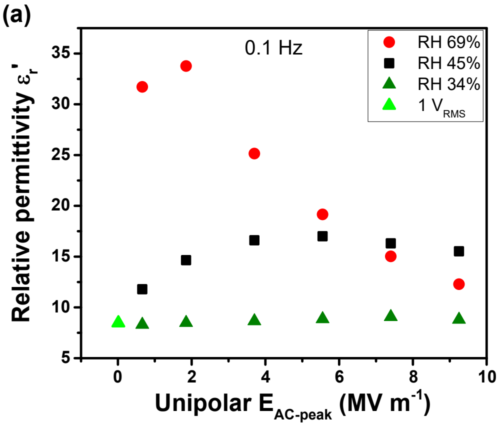

Fig. IV.5. Permittivité diélectrique relative en fonction du champ électrique à différents taux d'humidité.

Nous avons obtenu des films polyuréthane de différentes couleurs allant de l'incolore au jaune pâle. Les analyses DSC ont montré une petite modification de la structure qui peut expliquer des comportements différents sous champ électrique. Nous avons montré que le procédé d'élaboration doit être encore plus contrôlé en termes de température, de conditions de mélange et d'exposition à la lumière, pour limiter le jaunissement et donc la possible modification de la séparation de phases segments rigides / segments souples. Le problème des additifs inconnus utilisés par le fournisseur industriel peut également jouer un rôle.

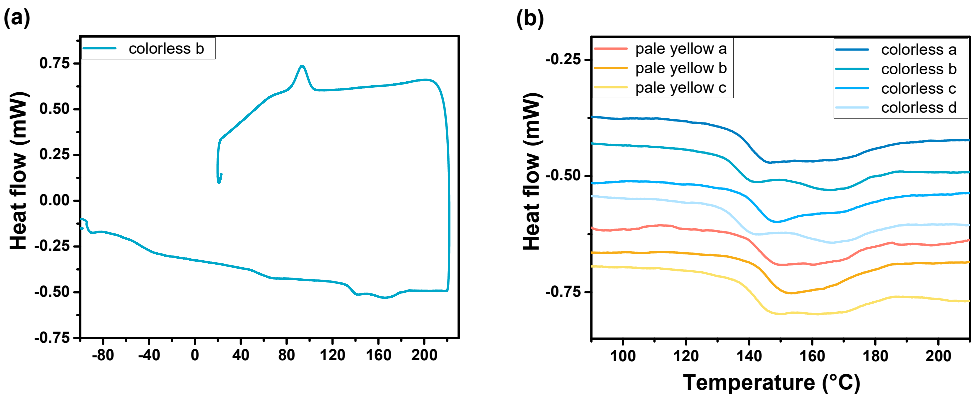

Fig. IV.6. Analyse DSC des films de polyuréthane de différentes couleurs : a) exemple d'un thermogramme sur toute la gamme de températures b) endothermes bimodaux sur la gamme 100-200°C.

La valeur de permittivité du polyuréthane est influencée par un effet conjoint de l'humidité et du champ électrique. L'eau absorbée par le polymère peut contribuer à la polarisation globale. L'effet plastifiant de l'eau est en accord avec la diminution des valeurs du module de Young.

Avec un meilleur contrôle des conditions d'élaboration et de mesures, il est montré pour le PU étudié (PU 87) et pour 2 autres PU présentant différents taux de segments rigides/segments souples que les valeurs des coefficients M31 expérimentaux et prédits sont très proches.

Les propriétés diélectriques montrant une assez forte variation autour de la température ambiante, des études complémentaires liant mesures sous haut champ et sous différentes températures seraient utiles.

<u>Le chapitre 5 présente l'effet des charges sur les propriétés des composites et les possibles origines de l'amélioration limitée du coefficient électromécanique.</u>

Incorporer des nanocharges conductrices est normalement une méthode efficace pour améliorer les propriétés d'actionnement, compte tenu des fortes valeurs de permittivités attendues et d'un renforcement mécanique modéré. Pourtant dans la littérature même avec des permittivités fortement augmentées le gain sur le coefficient électromécanique est souvent très limité. L'objectif de ce chapitre a donc été d'élaborer une série de composites polyurethane / nanoplaquettes de graphène fonctionnalisé (PU/OFG) et d'analyser les origines possibles de la faible performance électromécanique.

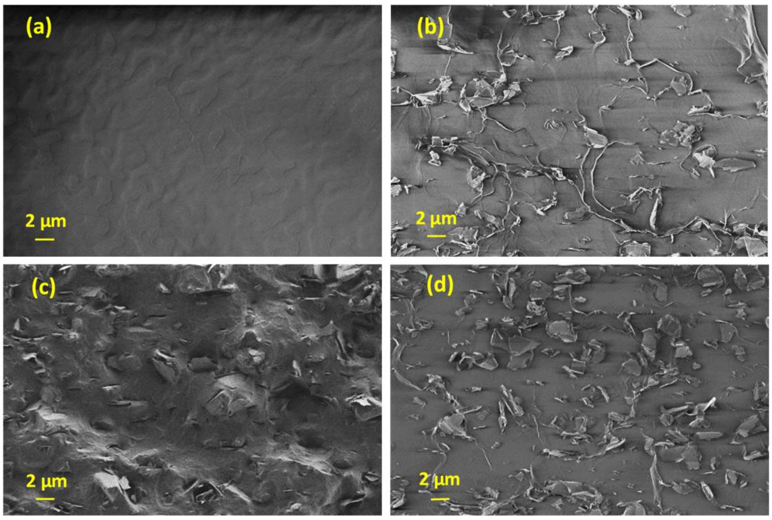

Fig. IV.7. Images MEB sur échantillons cryofracturés : (a) PU pur, (b) 5.40 wt% OFG, (c) 10.25 wt% OFG, (d) 13.13 wt% OFG

La distribution 3D des nano-plaquettes dans les composites a été confirmée par des observations au Microscope Electronique à Balayage (MEB) et par les paramètres de la loi de percolation. Le renforcement mécanique est resté modeste probablement en raison d'une adhérence modérée entre le graphène et le polymère, comme le montre les images MEB et l'analyse des propriétés mécaniques avec le modèle Halpin-Kardos.

Les expériences DSC ont révélé que la microstructure du polyuréthane n'était que légèrement affectée par la présence de graphène fonctionnalisé.

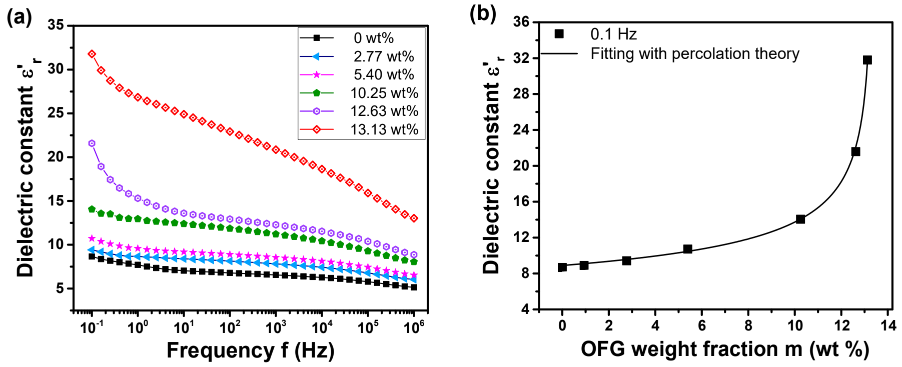

Fig. IV.8. Variation de la permittivité en fonction de la fréquence (a), et du taux de graphène (b)

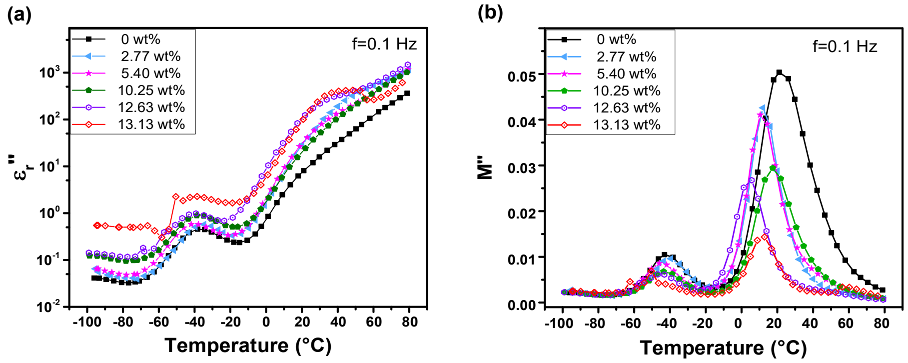

Fig. IV.9. Relaxations diélectriques at 0.1 Hz en fonction de la température (a) partie imaginaire de la permittivité (b) partie imaginaire du module électrique

Comme attendu, une forte augmentation de la permittivité a été obtenue au voisinage de la percolation, ainsi qu'une diminution en fonction de la fréquence. La variation de la conductivité DC a montré que les nano-plaquettes se comportent comme des pièges pour les espèces mobiles chargées. L'énergie d'activation obtenue se situe entre 0,7 à 0,9 eV, quelle que soit la teneur en graphène ce qui va dans le sens d'une origine ionique de la conduction.

Une étude détaillée a été réalisée sur les pics de relaxation diélectrique de -94 ° C à 80 ° C à basse fréquence, après suppression de la contribution de la conductivité DC. Le fitting des relaxations avec l'équation d'Havriliak-Negami a indiqué une contribution des OFG à la polarisation de type Maxwell Wagner Sillars et à la relaxation dipolaire α. La polarisation MWS est plus importante à température ambiante.

Un effet bénéfique de l'introduction de l'OFG dans la matrice PU est qu'elle stabilise les propriétés diélectriques sous champ électrique et sous différents taux d’humidité. Contrairement au PU pur, la permittivité des composites sous haut champ électrique n’est pas augmentée. Cela peut expliquer en partie les valeurs de M_{31} obtenues plus faibles. Et même en contrôlant bien les conditions de mesures, le M_{31} expérimental reste en dessous du M_{31} attendu dans le cas des composites.

Une explication d'origine possible de cet écart est que la polarisation interfaciale a pu faire diminuer le champ électrique réellement vu par le composite, et vient donc contrebalancer l'augmentation de la permittivité. D'autres facteurs, comme une adhésion interfaciale mécanique modérée ainsi que des fluctuations de température autour du maximum du pic de relaxation, pourraient également expliquer les valeurs des coefficients M_{31}.

Conclusions et perspectives

Les conclusions de la thèse résument les points essentiels qui apportent des réponses aux deux questions : quel est le mécanisme responsable de la déformation induite par le champ dans le polyuréthane ? Comment les nanocharges conductrices influencent les propriétés électromécaniques ? Elles soulignent également l'importance de contrôler soigneusement les conditions expérimentales utilisées lors du procédé d'élaboration et lors de la mesure des propriétés.

Les méthodes « Bender » et « strain-stress » (déformation-contrainte) proposées ont permis de caractériser le couplage électromécanique des EAP. La comparaison des valeurs du coefficient M_{31}, simulées par Comsol et mesurées expérimentalement, conclut à la contribution majeure de l'effet Maxwell par rapport au phénomène d'électrostriction. Les deux méthodes conduisent à des valeurs M_{31} de PU de même ordre de grandeur (10^{-18} m^2 V^{-2}), ce qui est plus précis que celles rapportées dans la littérature (10^{-19} à 10^{-13} m^2 V^{-2}). Toutefois une dispersion des résultats expérimentaux est observée selon les échantillons.

Alors que le coefficient M_{31} est mesuré à des niveaux élevés de champs électriques, la valeur prédite trouvée dans la littérature est le plus souvent obtenue à partir de la permittivité et du module de Young mesurés à de faibles niveaux. Pour le polyuréthane étudié, l’écart observé entre le M_{31} mesuré et le M_{31} calculé n’est pas dû au module d’Young, qui est indépendant du champ électrique ; mais il est en partie dû aux propriétés diélectriques, qui varient avec les caractéristiques du champ électrique (forme du signal, amplitude, fréquence et durée d'application).

De plus, à des champs électriques élevés, la valeur de permittivité est sensible à d'autres facteurs, notamment l'humidité, le procédé d'élaboration et les conditions de température. La valeur de permittivité est influencée par un effet conjoint de l'humidité et du champ électrique, qui font varier le temps nécessaire pour atteindre l'état d'équilibre. L'eau absorbée dans le PU agit comme plastifiant et peut contribuer à la polarisation globale. Le procédé d'élaboration pourrait affecter le nombre et le type de liaisons hydrogène qui relient les segments rigides et souples, et peut donc modifier la permittivité. Un pic de relaxation diélectrique étant présent au voisinage de la température ambiante, une petite fluctuation de température peut donc affecter significativement les propriétés du PU.

Avec des conditions contrôlées de taux d'humidité et d'application du champ électrique, un bon accord a été obtenu entre les valeurs M_{31} mesurées et calculées, pour le PU étudié et deux autres PU présentant un taux HS / SS différent.

Des nanocomposites PU / OFG avec une teneur en OFG allant de 2,77% à 13,13% en poids ont été préparés en utilisant un procédé de coulage en bande. Les caractérisations expérimentales et le traitement des données à l'aide de lois physiques dédiées révèlent que les nanoplaquettes fonctionnalisées sont dispersées de manière homogène avec une distribution en trois dimensions, mais avec une cohésion interfaciale modérée avec la matrice PU.

Par rapport au PU pur, la permitivité est multipliée par quatre avec 12,63% en poids d'OFG, juste avant le seuil de percolation (13,34% en poids). La spectroscopie diélectrique a mis en évidence que les OFG contribuent à la polarisation interfaciale et à la polarisation dipolaire (relaxation α) en augmentant la rigidité diélectrique. À faible et moyenne teneur en OFG, la contribution à la polarisation dipolaire est plus significative que celle à la polarisation MWS. En utilisant des nanocharges conductrices, une augmentation plus élevée de la rigidité diélectrique MWS était attendue. Une explication possible pourrait être que la distribution volumique aléatoire des nanocharges n’a pas permis une orientation des dipôles engagés dans la polarisation interfaciale, en particulier à faibles teneurs.

La conductivité DC est également modifiée par l'incorporation de nanocharges. Elle diminue avec l'incorporation des OFG pour un taux inférieur à 10,25% en poids certainement en raison de la couche de fonctionnalisation, puis augmente pour des taux plus élevés. La valeur de l’énergie d'activation obtenue pour le mécanisme de conduction est plutôt en accord avec une origine ionique.

L’augmentation significative de la permittivité et le renforcement mécanique modeste conduisent bien à une augmentation du M_{31} calculé, mais ce n’est pas le cas pour le coefficient expérimental, même avec des conditions contrôlées. Des résultats similaires ont été obtenus avec des nanoplaquettes de graphène fonctionnalisées avec groupement ammoniac, et avec des charges isolantes de titanate de baryum, mettant en évidence que le comportement observé n'est pas lié au type de charges ou à la fonctionnalisation.

Un effet bénéfique de l'introduction d'OFG dans la matrice PU est de stabiliser les propriétés diélectriques, en ce qui concerne le taux d'humidité et l'amplitude du champ électrique. Pourtant c'est aussi l'une des raisons qui explique le faible couplage électromécanique obtenu pour les composites, puisque leur permittivité sous fort champ électrique n'est pas augmentée comme c'est le cas du PU pur.

Une autre explication possible de l'écart observé entre le M_{31} mesuré et calculé est que la polarisation interfaciale réduit le champ local et contrebalance l'augmentation de la permittivité. La cohésion modérée entre OFG et matrice PU pourrait également jouer un rôle.

Cette thèse montre les limites de la méthode d'incorporation de nanocharges pour une amélioration des performances électromécaniques du polyuréthane. Du fait de l'hétérogénéité du polyuréthane, ce matériau présente déjà une bonne valeur de coefficient M_{31}.

Les objectifs de la thèse étaient certainement trop ambitieux en raison de la nanostructure très complexe du polyuréthane et du fait que ce polymère industriel contient des additifs de nature inconnue.

Le polyuréthane lui-même est complexe et présente un bon couplage électromécanique. Des recherches supplémentaires sont nécessaires pour une compréhension plus approfondie de la déformation sous champ électrique, en particulier en termes de transports de charges électriques, tels que la diffusion d'ions. Elle nécessitera une parfaite maîtrise de la composition et des conditions de mesure. Il faudrait se rapprocher d'un laboratoire maîtrisant la technologie de fabrication du polyuréthane pour éviter l'utilisation d'additifs et bien contrôler la composition. Certaines modifications de la microstructure doivent également être envisagées, par exemple jouer sur le taux de microséparation de phases, le choix des monomères de départ ou encore plastifier le polyuréthane.

Concernant le rôle réel des charges, il apparaît primordial de considérer des polymères moins complexes, histoire d'éviter un éventuel effet de couplage entre les hétérogénéités microstructurelles intrinsèques et extrinsèques. L'incorporation de charges dans des matériaux simples ou modèles, avec une composition et une architecture contrôlées, peut aider à relever certains des défis tels que le rôle exact de la polarisation interfaciale et l'effet de l'organisation des nano-charges au sein de la matrice sur la distribution des dipoles.

La polarisation d'électrode devrait aussi être considérée. Elle pourrait être étudiée en modifiant la nature et la géométrie des électrodes, et en faisant varier l'épaisseur du film EAP.

Les performances électromécaniques d'un actionneur flexible ne dépendent pas seulement des propriétés intrinsèques du polymère, mais également de la structure géométrique. Les conditions aux limites jouent un rôle important sur les caractéristiques. Une étude préliminaire a été réalisée et a abouti à des électrodes à lignes espacées imprimées sur une surface en polyuréthane. A l'aide de l'impression 2D et 3D, il serait intéressant d'améliorer les performances de l'actionneur en optimisant la compliance des électrodes.

Pour toutes ces perspectives, des caractérisations plus avancées devraient être menées pour analyser en profondeur les matériaux au niveau de l'interface. Et le développement d'outils numériques tels que les calculs par éléments finis s’avèrera fort utile pour la suite des recherches.

V. Introduction

With their lightweight, flexibility, ease of elaboration into different sizes and shapes, and large electric-field-induced strain, the electroactive polymers (EAPs) are considered as a promising alternative to the piezoelectric ceramics or shape memory alloys for flexible actuators. Research on EAPs have boosted in the past 20 years.

The EAPs can be divided into two families, namely Ionic EAPs and electronic EAPs. The first benefits from the great strain, low operating voltage, and good biocompatibility, are used in drug delivery, micropumps, etc. However, they are limited by the low force, short lifetime, and requested wet condition. The electronic EAPs, such as piezoelectric and dielectric polymers, present a wide range of strains and blocking forces. In addition, their electromechanical responses are considered to be rapid. Electronic EAPs are therefore widely used in mimetic robotics, soft grippers and so on.

One promising candidate of electronic EAPs is the thermoplastic polyurethane (PU). With a unique mixing structure of hard segments and soft segments, PU shows a high permittivity compared to other dielectric elastomers. It also shows a good combination of strain and blocking force, low cost and easy accessibility in commercial market, which are favorable to actuator applications.

One common limit for electronic EAPs is the need for a high electric field. Considerable attempts have been made to improve the electromechanical coupling efficiency so as to decrease the operating voltage. The electromechanical coupling coefficient increases with the dielectric permittivity and decreases with the elastic modulus of the EAPs. The incorporation of conductive fillers is one possible way to increase the permittivity. Nano-sized fillers with large specific surface area such as nanotubes or graphene are of great interest. This thesis will focus on oxygen functionalized graphene (OFG) nanoplatelets incorporated into the polyurethane matrix.

The motivation of this thesis is toward a better comprehension of polyurethane composite films, so as to achieve a better control of the actuating performance. Though numerous studies in the actuating performance were conducted, it was firstly noticed that, the origin of the field-induced strain remains controversial, and with different types of characterization methods applied, the reported values of electromechanical coefficient show a large dispersion. Secondly, detailed investigations of the fillers' role on the macroscopic properties of composites are sometimes missing in the literature. Therefore, the aim of this thesis is to provide answers to the two following questions: Is it the electrostrictive phenomenon or the Maxwell mechanism responsible for the field-induced strain? In addition, what is the role of the nanofillers in the properties of nanocomposites?

With this aim, the thesis is arranged as follow:

The first chapter provides general introduction of the EAPs for flexible actuator applications, and presents the properties of polyurethane. Through a literature study, the scientific questions we interest in are posed.

The second chapter presents the elaboration of PU/OFG nanocomposites, and the characterization techniques from microstructural analysis to macroscopic mechanical, electrical and electromechanical properties. Detailed information on the experimental setups and on the measuring conditions is given.

The chapter 3 is devoted to proposing reliable characterizations for the electromechanical coefficient (M_{31}) determination. Bender method and strain-stress method are proposed and validated, with the boundary conditions, the influence of electrodes, and the error sources considered. The experimental values are then compared with the values simulated by Comsol Multiphysics finite-element based software, so as to address the mechanism of the electromechanical coupling.

The chapter 4 is focused on the electric field dependence of the PU dielectric properties. At the same time, the impact of the elaboration process humidity and temperature on the dielectric properties under high electric field is also studied; microstructural characterizations are conducted to understand the impact of these factors.

Using Bender method and controlled measurement conditions, the objective of chapter 5 is to verify the contribution of OFG on the mechanical, electrical and electromechanical properties. The properties of composites as a function of OFG weight fraction are studied with the help of multi-scaled characterizations. Experimental results were compared with models from the literature.

At the end, a general conclusion will sum up the most important achievements of this thesis research. Future challenges and prospects will be then outlined.

VI. Table of contents

Chapter 1. State of Art

The aim of this chapter is to present the state of art. After a brief overview on electroactive polymers and several application examples, the polyurethane material is introduced, in terms of its specific structure and mechanical properties. Mechanisms of polarizations and conductions are then described. Next, electric field induced deformations are examined, with their controversial origin between the Maxwell effect and the electrostriction phenomenon notified. At last, the possible ways to improve the electromechanical coupling are presented.

1.1 Flexible actuators

1.1.1 General information on actuators

An actuator is a device that moves or controls some mechanism, by turning the control signal into a mechanical action. Different types of energies can be used, such as electric, magnetic, thermal, pneumatic or hydraulic energies. As major categories of actuator materials, the following can be mentioned: shape memory alloys (SMAs), magnetostrictive alloys (MSAs), electroactive ceramics (EACs) and electroactive polymers (EAPs)[1–4] The shape memory alloys such as gold-copper alloy, indium-titanium alloy and nickel-titanium alloy could generate relative large strain and go back to the rest state by heating and cooling. However, they are limited by the time request to cool down and return to the rest position. MSAs and EACs both suffer from high stiffness and consequently small strain, in addition, EACs often have trouble with the fragility, which make them not ideal materials for artificial muscles application. The main advantages of EAPs are their lightweight, flexibility, ease of elaboration in different sizes and shapes, and the large electric-field-induced strain. EAPs are therefore of great research interest for soft robotics and biomimetics fields [5–11]. Table 1.1 present a generic comparison in terms of actuating performances among EAPs, MSAs and EACs.

Table. 1.1. Characteristic performances of EAPs, SMAs and EACs as actuators[2] .

	EAPs	SMAs	EACs
Strain	**over 300 %**	**< 8%, short fatigue time**	**0.1 -0.3 %**
Blocking force	**0.1 -25**	**200**	**30-40**
Response time	**µsec to min**	**msec to min**	**µsec to sec**
Density	**1-2.5 g cm^{-3}**	**5-6 g cm^{-3}**	**6-8 g cm^{-3}**
Operating voltage	**1-150 MV m^{-1}**	**5 V**	**50-800 V**
Power consumption	**mW**	**W**	**W**
Fracture behavior	**Elastic**	**Elastic**	**Fragile**

1.1.2 Electroactive polymers

The history of EAPs could date back to 1880 when Röntgen succeeded to observe a deformation on a pre-stretched natural rubber upon electrification with sprayed-on charges. Later in 1949, Kuhn and later Katchalsky observed the chemical-induced deformation in synthetic polyelectrolyte gels. The collagen filaments were found to expand or contract depending on the degree of acidity of the solution. However, not until the last 20 years great research and industrial interests boosted in the electric field stimulated polymers[12]. A summary of different EAPs proposed by Bar-Cohen in the beginning of 21st century[13] is widely adopted by researchers in this field. EAPs could be divided into two types, Ionic EAPs including Ionic gels, ionomeric polymer-metal nanocomposites (IPMCs), conductive polymers (CPs) and carbon nanotubes (CNTs); and electronic EAPs including piezoelectric polymers, dielectric polymers and electrostrictive grafted polymers.

Table 1.2 [13,14] lists the categories and representative examples of ionic and electronic EAPs, and made a brief comparison between the ionic and electronic EAPs, in terms of the advantages and disadvantages for flexible actuators application.

Table. 1.2. Main ionic, electronic EAPs and their advantages & disadvantages

EAP type	Reported materials	Pros and Cons
	Electronic EAPs	
Piezoelectric polymers	PVDF (PolyVinylidene Fluoride) trifluoroethylene), P(VDF-TrFE)	Pros: Rapid response Hold under DC activation Large actuating force High energy density Long lifetime Cons: High fields required No effect of voltage polarity
Dielectric elastomers	Silicones, Polyurethanes, acrylates, natural rubber	
Electrostrictive grafted elastomers	Flexible backbone + graft polymer	
	Ionic EAPs	
Ionic gels	Poly(vinyl alchohol) gel with dimethyl sulfoxide, poly(acrylonitrile) with conductive fibers	Pros: Bi-directional actuation Low field request Cons: Only in wet state Encapsulation/barrier layer required Low efficiency Do not hold in DC actuation Relative low blocking force In aqueous systems, the material sustains hydrolysis at >1.23V
Ionomeric polymer-metal nanocomposites (IPMCs)	Base ionomers: Nafion® (perfluorosulfonater), Flemion® (perfluorocarboxylate); Cations: tetra-n-butylammnium, Li^+, and Na^+; Metal: Pt and Au	
Conductive polymers (CPs)	Polypyrrole, poly(ethelyne dioxythothiophene), poly(p-phenylene vinylene)s, polyaniline and polythiophenes	
Carbon nanotubes (CNTs)-electrolyte	Single and multiwalled carbon nanotubes in contact with liquid or solid electrolyte	

1.1.2.1 Ionic EAPs

In ionic EAPs, the actuation is caused by the displacement of ions inside the polymer. One essential advantage is the low electric field requested, typically a few V. However, the main drawbacks that limit their application as flexible actuators are on one hand the short lifetime, and on the other hand the constraints due to the electrochemical mechanism, i.e., low blocking force, possible degradation of material or electrodes[12].

Ionic gels

The ionic gels consists of cross-linked polymers swollen in solvent, with environmental stimulation such as temperature, pH, electric field and the introduction of specific ions, the polymer gels expel the solvent and change volume[15,16].

The deformation in such polymer gels is much higher comparing with other EAPs. Their behavior can be well modelled[17], and the deformation change direction with the polarity of electric field[15].

Ionomeric polymer-metal composites

Typical ionic polymer-metal composites (IPMCs) reported are based on the ion-exchange membranes are Nafion® (perfluorosulfonate, Dupant) and Flemion® (perfluorocarboxylate, Asahi Glass, Japan)[18]. IPMCs consist of a thin ionomeric membrane and counter-ions, with platinum or gold electrode plated on both surface of the membrane. The electromechanical deformation principle in IPMC is presented by an example in Fig. 1.1. The ionic groups tend to aggregate and form clusters. These clusters are are fully interconnected and saturated by water readily. The ionomeric membrane shows high permeability to water and cations but not anions. When an electric field is applied, due to the electro-osmosis of cations, their solvent water gathers at cathode and depeltes at anode, causing the membrane to bend[19].

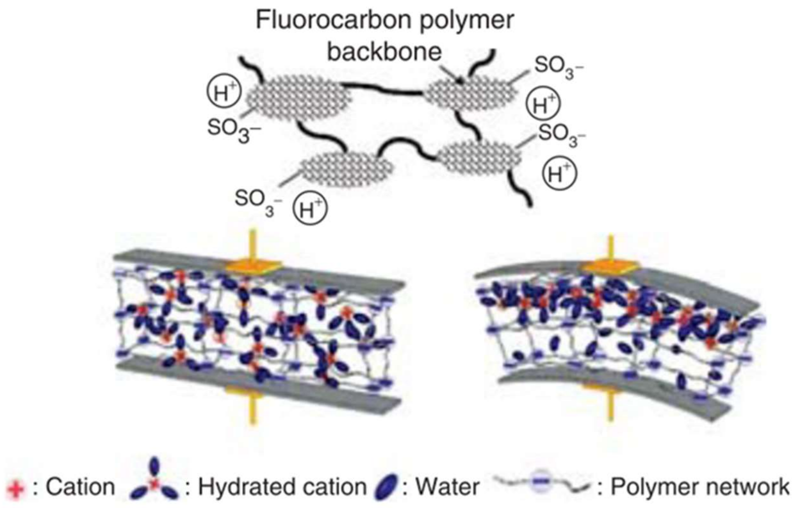

Fig.1.1 Ionic Polymer-Metal Composites (IPMC) actuation principle[13].

IPMC could generate large deformation with the electric field in order of 1 V. The ideal work environment for IPMCs is wet environment; therefore, numerous applications in biomimetic filed have been studied. The applications include but not limited to underwater robotic fish, micropumps, and biomedical applications [20–22]. The main challenges for IPMCs are the limited blocking force, the water permeability of the coating as well as the permanent deformation under DC voltage[2].

Conductive polymers

Polymers such as polysulfurinitride, polypyrrole, poly(ethelyne dioxythothiophene), poly(p-phenylene vinylene)s, polyaniline and polythiophenes are known as conductive polymers (CPs). These polymers are often semiconductor naturally, and require chemical or electromechanical doping to become coductors[23,24]. Their conductivity can reach 10^2 -10^3 S cm^{-1}. To be used as actuators, CPs are associated with two electrodes and electrolyte to generate oxidation-reduction reactions. With the application of a voltage, the oxidation-reduction reactions happen in accompany with the addition or removal of electrolyte from the polymer chain, leading to the volume change of the membrane.

The actuators made of CPs exhibit drawbacks of low output force and stiffness, therefore efforts has been focused on improving stiffness without hindering much the deformation[25]. Recent research makes CP actuators possible to be used in both aqueous and dry environments, which has widen the application field in drug release, mechanical sensing and micro-robotic manipulation systems[26].

Carbon nanotubes

The working principle of carbon nanotubes (CNTs) is similar to that of CPs, they are in contact with liquid or solid electrolyte. Fig. 1.2 presents the working principle of CNT-electrolyte actuator. As shown in Fig. 1.2 (a), a potential injects charges of different signs in the two CNT electrodes. These indicated charges are compensated by the ions from the electrolyte, and form charge double layer on each electrode. Fig. 1.2 (b) described an example of bimorph CNT actuator: the two CNT electrodes are attached by adhesive tape, when voltage is applied, charge double layer forms on each electrode. The cantilever bends due to the different field-induced strain in the two electrodes. The working voltage is as small as 1 V, the generated strain is relative small as well, between 0.1% and 1 %[27].

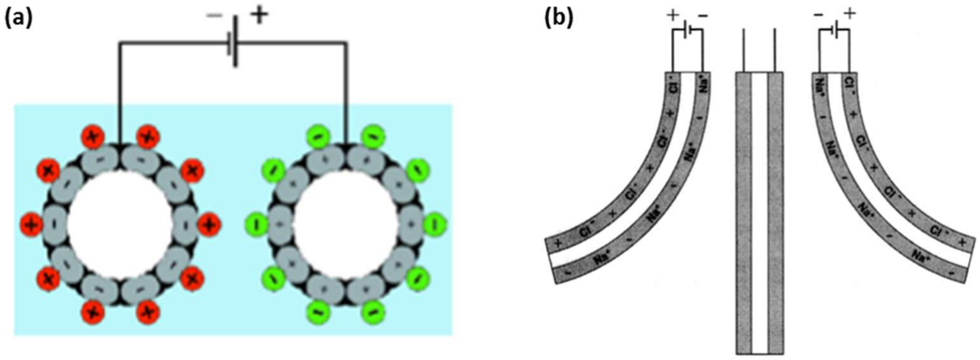

Fig. 1.2. Working principle of the carbon nanotube actuator: (a) charge injection, (b) cantilever based actuator operating in aqueous NaCl, with reversed voltage and without voltage[27].

1.1.2.2 Electronic EAPs

In contrast to the ions diffusion mechanism in the ionic EAPs, the electronic EAPs are driven by an electric field. The benefits of the electronic EAPs mainly lie on the short response time, high strain and force achieved, as well as long lifetime. However, comparing with ionic EAPs, the main drawback of electronic EAPs is the high electric field required. Therefore, researches on thin EAPs films and improving the electromechanical coupling efficiency are of great interest.

Piezoelectric polymers

The piezoelectric effect refers to an electric response generated by a material upon a mechanical stimulation. For actuators, it's the inverse effect which is used, i.e., mechanical change under electric field. Thanks to the lightweight and lower stiffness compared with ceramic, piezoelectric polymers provide solutions for the development of sensors and actuators. The most representative piezoelectric polymers are PVDF and PVDF-based copolymers, the odd-numbered polyamides and several polymer composites[28,29]. Piezoelectric polymers are able to generate a relative high strain (2%) compared with electroactive ceramics (0.2%). The actuating force of PVDF are high, compared with ionic EAPs thanks to the high elastic modulus. Nevertheless, large electric fields are needed.

Dielectric elastomers

Dielectric elastomers (DEs) are type of soft and insulating polymers. When dielectric elastomers are sandwiched between two compliant electrodes, and submitted to an electric field, a statistic columbic force is generated by the accumulated charges on the electrodes. This force compresses the dielectric elastomers in thickness, and assuming that the volume of elastomers is incompressible, an expansion can be observed in surface. The strain is proportional to the square of electric field. A schematic illustration of the mechanism is presented in Fig. 1.2[12].

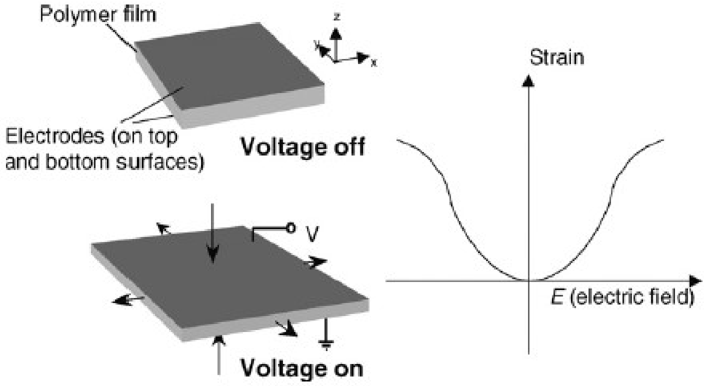

Fig. 1.3. Representation of the field-induced strain in a dielectric EAP[12].

Various polymers such as polyurethane, silicone and acrylic elastomers are of this category. Due to the low elastic modulus and the ability to sustain high electric field, DEs could generate very high strain (100% for silicone and acrylic materials). The great deformation leads to specific energy density more significant than any other electronic EAPs, making them promising candidates for various applications. However, it is worth noting that the mechanism of the electromechanical coupling is not yet clarified. In certain polymers such as polyurethane, the contribution mechanism of the field-induced strain is controversial between Maxwell and electrostriction[30–33].

The efforts have been devoted into the configuration and fabricating methods for wild applications, such as biomimetic robots, artificial eyes, haptic devices, live optical surfaces et.al[34–37].

Electrostrictive graft polymers

Fig. 1.4 presents the typical structure of the grafted polymer. It is made up of two parts: the flexible backbone and the side chains (grafts). The grafts can create three-dimensional cross-link sites between polymer chains, and form polar crystalline. The polar crystalline are reoriented with the presence of electric field, contributing to the field-induced strain.

Similar as dielectric elastomers, the field-induced strain in electrostrictive graft polymers are in proportional to the square of electric field, whereas the strain is dominated by the reorientation of the crystalline or semi-crystalline structure with in the polymer. The introduction of grafts could therefore increase significantly the electromechanical coupling efficiency in EAPs[38,39].The PVDF-based materials consist the main candidates of the electrostrictive graft polymers[13,40]. For example, a poly(vinyldene fluoride-trifluorethylene) mixed with graft elastomer powder lead to higher strain response predominated by electrostrictive force[39].

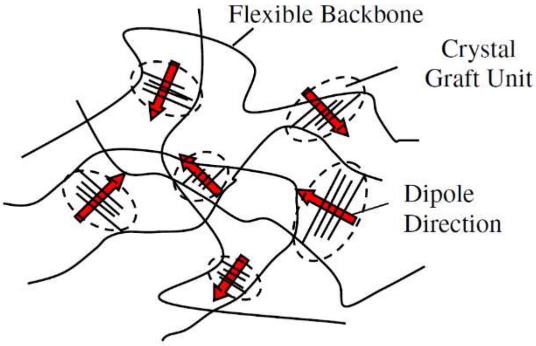

Fig. 1.4. Schema of graft elastomer structure.[41]

1.1.3 Applications of EAP actuators

With the capability to achieve great strain and rapid response time, flexible actuators made of EAPs have motivated numerous studies in wide application fields. This section list a few examples in different fields.

In roboticists, achieving lifelike motion has long been a desire. For example in entertainment industry, their need for humanoid robots and robotic creatures leads to strong motivation for developing lifelike robots. EAPs provide a possible solution to mimic nature muscles.

Fig. 1.5 shows the photos of a different legged robot dubbed Skitter[42]. The skitter is based on a research of cockroach locomotion. In Skitter, six rolled acrylic DE actuators were used, providing six single-degree-of-freedom legs. It can reach a maximum speed of 7 cm s^{-1}, and able to rotate back when obstacles appear in forward direction.

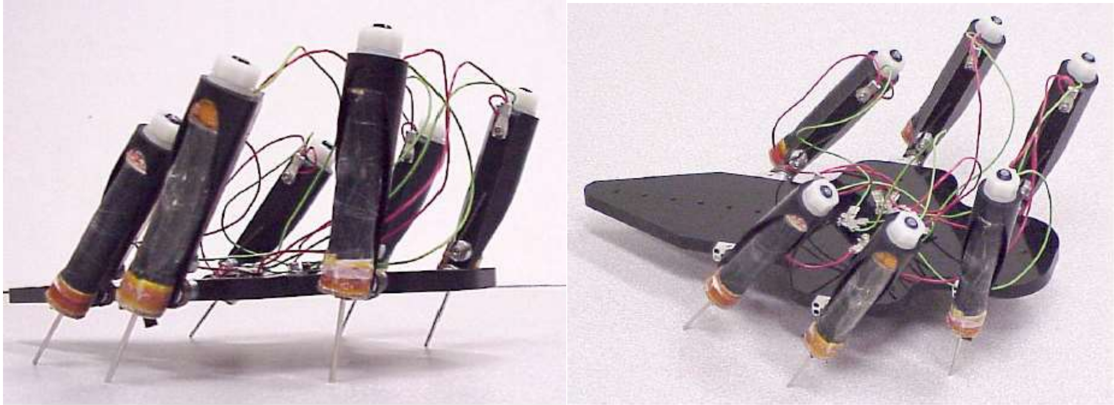

Fig. 1.5. Skitter robot using six rolled actuators[42]

Another important application for EAPs is in biomedical field. With the low driven voltage, large strain and ability to operate in electrolyte, IPMCs show great potential in medical devices.

Fig. 1.6 depicts the application of polypyrroles (PPy)/Au composites actuator as a blood vessel connector[43]. The PPy/Au bilayer is curled into a roll in the reduced state is inserted halfway into one end of a severed blood vessel, then the other end of the vessel is pushed over the other end of the rolled tube. With the oxidation of PPy, the tube expands in a few minutes and hold the two vessels together.

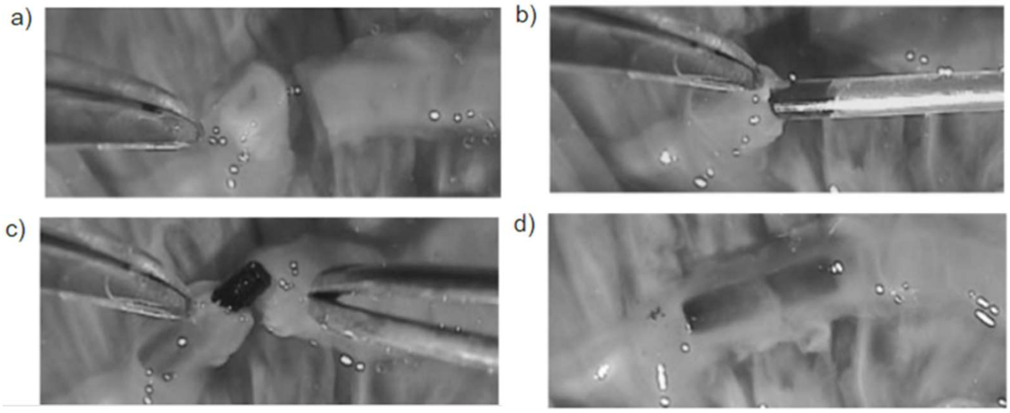

Fig. 1.6. Application of PPy/Au composites as a blood vessel connector[43].

Grasping and manipulations are canonical challenges in robotics, they can be simplified with the help of EAP actuators. Compared with rigid robots, soft grippers benefit from the compliance of EAPs, allowing them to adapt to various objects. Fig. 1.7 presents a group of soft gripper applications.

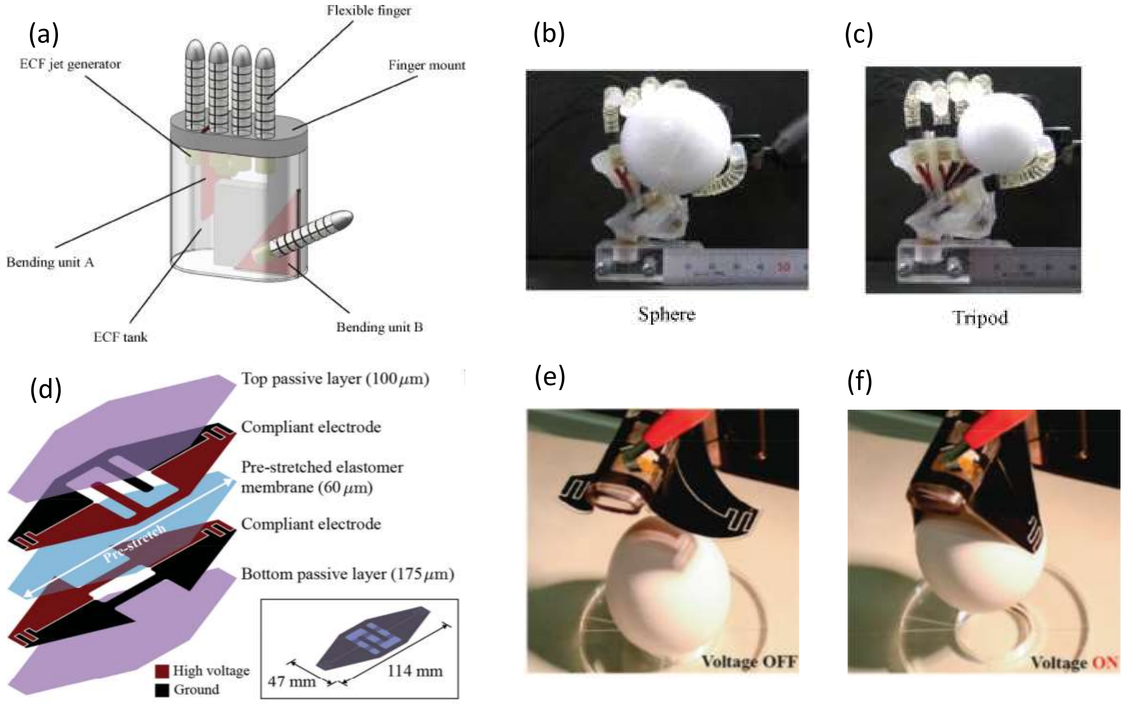

Fig. 1.7. Applications of EAP actuators as soft grippers. (a) structure of a robot hand; (b), (c) precision grasp of the robot hand [44]*; (d) structure of an electroadhesion-enabled soft gripper; (e), (f) the griper picking up an egg with application of electric field*[45].

1.1.4 Choice of polyurethane

As mentioned in 1.1.2.2, the dielectric elastomers are receiving much interest and are increasingly being used for the large strain and energy density.

Among the electronic EAPs, the polyurethane (PU) is a promising candidate due to its dielectric and mechanical properties, low cost, and tunable properties through composition control and incorporation of fillers. With the unique microphase separation, it shows favorable properties towards sensors and actuators application[46].

Another motivation is that our laboratory has acquired a good knowledge on PU material, and one of the objectives was a better understanding of the deformation mechanisms involved in this complex polymer and its composites.

1.2 Polyurethane

1.2.1 Structure and properties

Polyurethane is a category of polymer with repeating urethane group in its structure. Different from the other polymers, which are often synthesized from one single monomer, the structure of PU, is complex since they are generally made of two monomers, and sometimes in addition of a chain extender.

PU are generally polymerized by the reaction of isocyanates with alcohols. The nature of the monomer is diverse; Fig. 1.8 summarizes some commercial available PU and the monomers in their composition.

The polyol part (SS) can be made of polyether, polycarbonate or polyester group, the diisocyanate part (HS) can be an aromatic group such as methylene diphenyl 4,4’-diisocyanate (MDI) or aliphatic group as hydrogenated methylene diphenyl 4,4’-diisocyanate (HMDI). The variety of suitable monomers enables numerous possibilities to tailor the polymer backbone.

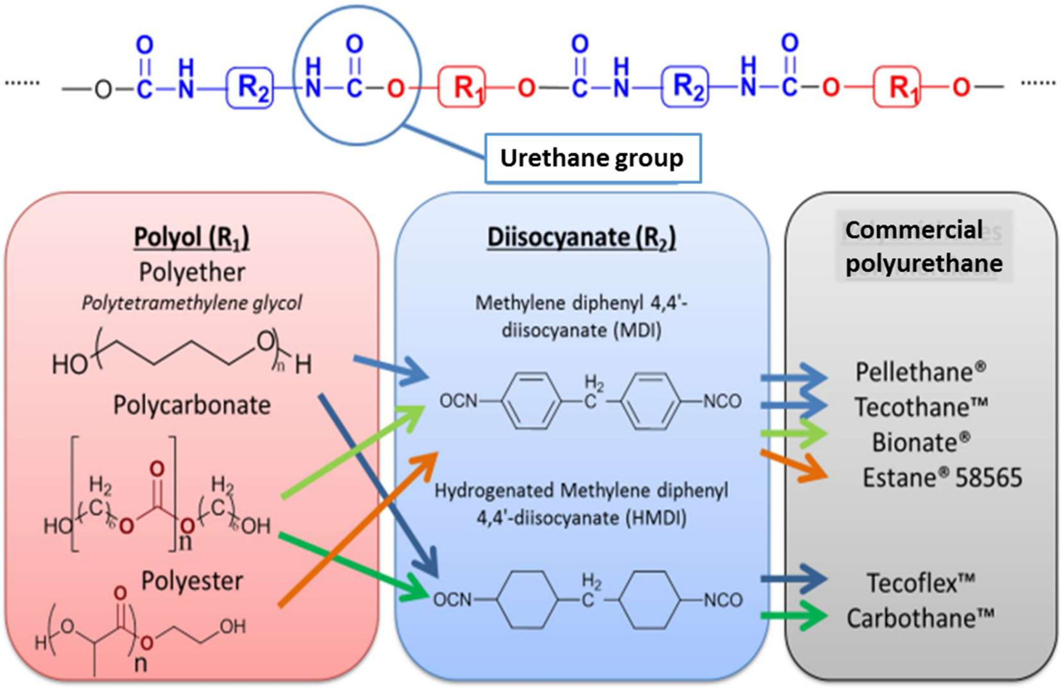

Fig. 1.8. Examples of commercial available polyurethanes obtained from different raw materials[47]*.*

This urethane group act as hard segments (HS), responsible for the stiffness and stability. The polyol serves as soft segments (SS), and provides flexibility to the polyurethane. These two segments are thermodynamically incompatible, which leads to the existence of two separated phases and mixed phase as shown in Fig. 1.9. The degree of separation and domain formation depends on the HS and SS nature and sizes, the type of the diisocyanate and macrodiol used to produce prepolymers, the type of the chain extender, and the molecular mass of the SS.

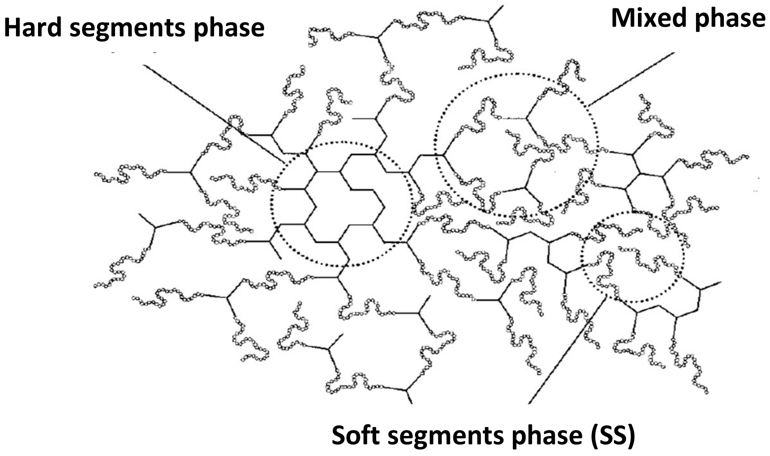

Fig. 1.9. Schematic presentation of the micro phase separation in polyurethane[48]*.*

There can be considerable hydrogen-bonding and/or crystallization of the polyurethane groups which may physically crosslinked network. There is therefore a combination of chemical (covalent) and physical (van der Waals) bonds in the network, which link the HS and the flexible SS together. Fig. 1.10 illustrates the possible interactions in the case of a MDI based polyurethane. Phase separation can also be influenced by the hydrogen bonds[49] .

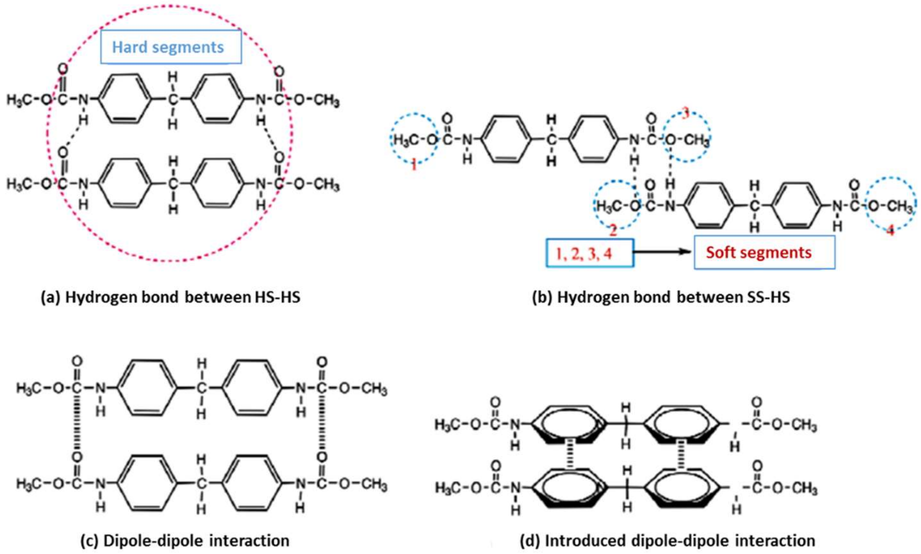

(a) Hydrogen bond between HS-HS

(b) Hydrogen bond between SS-HS

(c) Dipole-dipole interaction

(d) Introduced dipole-dipole interaction

Fig. 1.10. Possible interaction in MDI-based polyurethane[50]*.*

Dielectric and mechanical properties can be control through this large variety of composition. For example, the dielectric constant was found to vary linearly with the urethane density in a homologous series of PU[51] .

A large series of Young's modulus values is available, depending on the type of the hard and soft segments, the HS length, the ratio HS/SS.

1.2.2 Mechanisms of polarizations

Different types of polarizations can occur in dielectric materials when they are submitted to an electric field. The polarization mechanisms are summarized in Fig. 1.11.

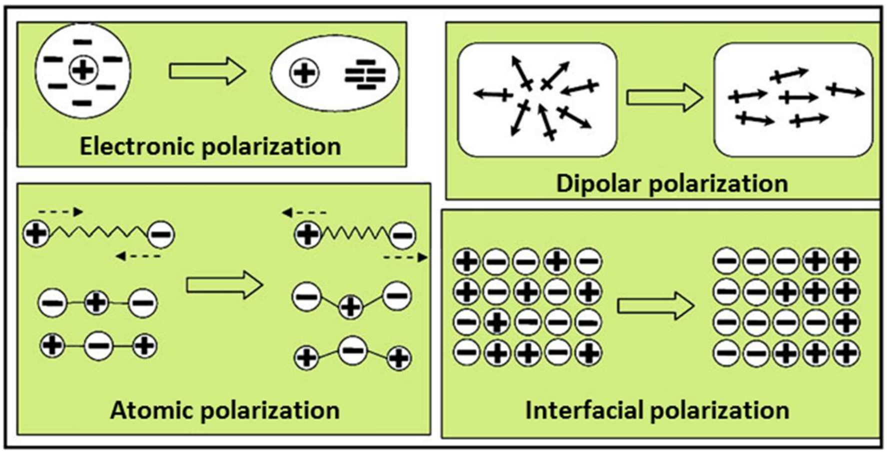

Fig. 1.11. Schematic representation of the polarization mechanisms in dielectric polymers[52].

Electronic polarization is related to the displacement and the deformation of the electron clouds around each atom. Atomic (or ionic) polarization concerns materials composed of different atoms. The ions and their accompanied electron clouds move with the electric field, leading to a distortion of atoms position and causing the atomic polarization. These two polarization mechanisms are very fast.

Dipolar or orientational polarization occurs in polymers containing permanent dipole moments. Interfacial polarization happens at internal interfaces in heterogeneous materials. Due to the polar and heterogeneous nature of PU, the last two polarization mechanisms are of particular importance. They are detailed in follow.

Electrode polarization can also play a role: due to the different conductive nature of electrode and dielectrics, the free charge carriers in the dielectrics tends to accumulate at the electrode/dielectrics interfaces and form electric double layers. The applied electric field drops quickly in these double layers, and sometimes may cause difficulty in the interpretation of other polarizations, especially at low frequencies[53].

1.2.2.1 Dipolar polarization

Dipolar polarization, also known as orientational polarization, happens only in materials with permanent dipoles. Note that there is difference between permanent dipoles and spontaneous dipoles. Permanent dipoles are normal dipoles due to the polarity of molecules, while spontaneous dipoles exist only in ferroelectric or piezoelectric materials.

The dipoles are randomly arranged without electric field due to the thermal agitation. When electric field is applied, the molecules possessing a permanent dipole moment experience a torque, tending to align themselves to the field direction, leading to dipolar polarization. The rotation of molecules depends on the neighboring molecular in a viscous medium, so it is highly depending on temperature.

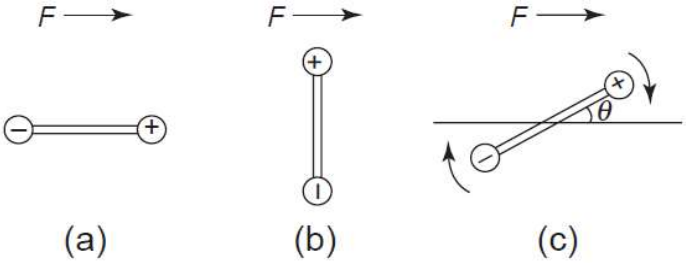

Fig. 1.12. The orientation of a dipole; (a) stable position, (b) unstable position, (c) orienting to the field direction[54]*.*

Dipoles such as C-O, C=O, C-N, O-H, N-H[55] exist in polyurethane backbones, their alignment to the electric field contribute to the dipolar polarization. Below glass transition temperature, γ polarization, the crankshaft motion of monomeric units in the main chain, and β polarization, the motion of polar carbonyl groups are responsible for the dipolar polarization[56]. Above glass transition temperature, α polarization, the segmental motion of the polymer chain could happen in amorphous phase.

1.2.2.2 Interfacial polarization

The interfacial polarization (also known as Maxwell-Wagner-Sillars polarization or MWS polarization) is attributed to the internal interfaces in heterogeneous materials. It happens when conductivity changes across the interfaces. With applied electric field, charge carriers in dielectrics accumulate at the interfaces, leading to interfacial polarization.

In polyurethane, the hard segments and soft segments exhibit very different conductive properties, which is favorable to interfacial polarization between the microphases. Space charges and ions could be trapped in the amorphous or polycrystalline phase, which in terms of PU, is the SS domain. In addition, the incorporation of fillers into PU matrix is generally believed to increase the heterogeneity.

Fig. 1.13. depicts a schematic presentation of the interfacial polarization.

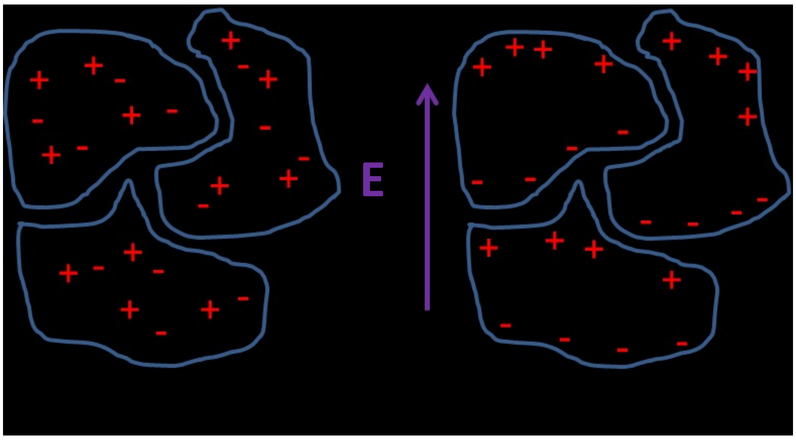

Fig. 1.13. Schema of the interfacial polarization in dielectric materials[57]

1.2.2.3 Havriliak-Negami model for relaxation analysis

The different polarization mechanisms contribute to the dielectric properties.

The permittivity can be described by the following formalism:

$$\varepsilon(\omega) = \varepsilon' - i\varepsilon''(\omega) \tag{1.1}$$

The real part of complex permittivity ε' refers to the energy storage capacity of the dielectric. The imaginary part ε" defines the dielectric losses. The portion of the dissipated energy is defined by the dissipation factor *tanδ*:

$$tan\delta = \frac{\varepsilon(\omega)''}{\varepsilon(\omega)'} \tag{1.2}$$

The permittivity depends on the frequency due to the relaxation phenomena of polarizations.

Fig. 1.14 gives a schematic presentation of the frequency dependence of ε' and ε" associated to typical relaxations in polymer.

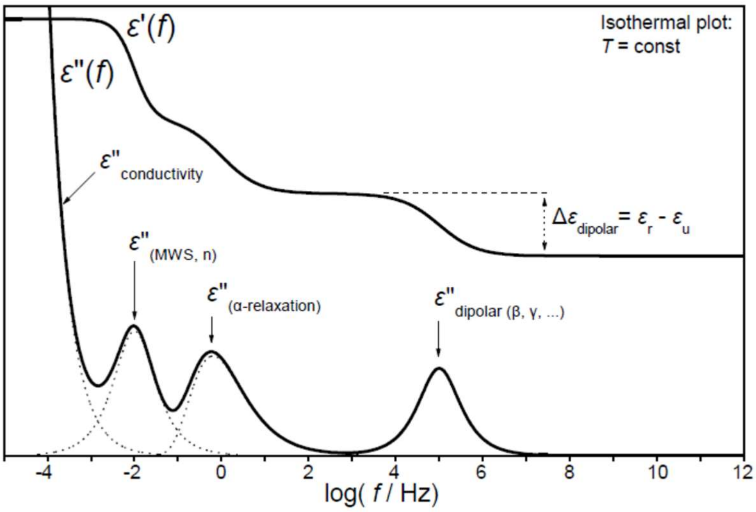

Fig.1.14. Schematic representation of the frequency dependence of ε' and ε", showing conductivity and typical relaxations peaks related to polarization mechanisms[58].

In polyurethane, four main phenomena can contribute to the permittivity in the temperature (near ambient) and frequency (low frequency) range where polyurethane actuators work, namely, dipole polarization, interfacial polarization, electrode polarizationand DC conduction[55,59].

In frequency domain, despite that Cole-Cole[60] and Cole-Davidson[61] models are widely applied on the complex permittivity to discuss the structural details in the case of simple molecules, they do not always fit the experimental data in the case of polymers. Havriliak and Negami[62] proposed a model taking into account the two models above, and proved that it is capable to predict precisely the permittivity of many polymers. The Havriliak-Negami equation has been widely used in polarization analysis for polymers[63–66].

The model is shown in equation (1.3)[62,67,68]:

$$\varepsilon(\omega) = \varepsilon_{\infty j} + \sum_j \frac{\Delta\varepsilon_j}{\left[1+(i\omega\tau_j)^{\alpha_j}\right]^{\beta_j}} \tag{1.3}$$

where ε_∞ is the dielectric constant at high angular frequency (ω) far from the relaxation peak, $\Delta\varepsilon$ is the dielectric increment of strength, τ is the characteristic relaxation time, and α and β are related to the symmetric and asymmetry broadening of the relaxation time distribution.

For the Havriliak–Negami equation reduces to the Cole–Cole equation, for it goes to the Cole–Davidson equation. For α=1 and β=1, the equation corresponds to the Debye model. The shape parameters α>0 and α, β≤1 are related to the ε” behavior as a function of angular frequency ω:

$$\varepsilon''\sim\omega^{m}, \text{ for } \omega<<1/\tau, \text{ with } m=\alpha \tag{1.4}$$

$$\varepsilon''\sim\omega^{-n}, \text{ for } \omega<<1/\tau, \text{ with } n=\alpha\beta \tag{1.5}$$

Applying the Havriliak-Negami analysis on each relaxation process allows one to determine the relaxation parameters. The real and imaginary parts of the permittivity can be expressed as follow:

$$\varepsilon^{'}(\omega) - \varepsilon_{\infty} = \gamma^{-\frac{\beta}{2}}\left(\varepsilon_0 - \varepsilon_{\infty}\right) cos\beta\theta \tag{1.6}$$

$$\varepsilon^{"}(\omega) = \gamma^{-\frac{\beta}{2}}\left(\varepsilon_0 - \varepsilon_{\infty}\right) sin\beta\theta \tag{1.7}$$

with

$$\gamma = [1 + (\omega\tau_0)^{1-\alpha} sin\alpha\left(\frac{\pi}{2}\right)]^2 + [(\omega\tau_0)^{1-\alpha} cos\alpha\left(\frac{\pi}{2}\right)]^2 \tag{1.8}$$

and

$$\theta = arc\tan[\frac{(\omega\tau_0)^{1-\alpha} cos\alpha(\frac{\pi}{2})}{1+(\omega\tau_0)^{1-\alpha} sin\alpha(\frac{\pi}{2})}] \tag{1.9}$$

1.2.2.4 Temperature dependence of the relaxation times

The relaxation times are temperature dependent. The dependence can be of Arrhenius type or Vogel-Tamman-Fulcher (VTF) type.

When the logarithmic plot of the relaxation time (log τ) show a linear relation with the reciprocal of temperature (1/T), it follows the Arrhenius law, and can be written as follow:

$$\tau = \tau_0 e^{(\frac{E_a}{K_B T})} \tag{1.10}$$

where τ_0 is the pre-exponential factor, E_a is the activation energy, and K_B is the Boltzmann constant. The Arrhenius dependence of relaxation time indicates a non-cooperative process. In polymers, γ and β relaxation often follows Arrhenius law.

The nonlinear evolution of relaxation time log τ versus 1/T follows the VTF equation:

$$\tau = \tau_0 e^{\left(\frac{B}{T-T_0}\right)} \tag{1.11}$$

where τ_0 is the prefactor, B is the pseudo-activation energy and T_0 is the equilibrium glass transition temperature. The nonlinear behavior is often attributed to the cooperative motion of polymer chain [69,70]. α relaxation often obeys VTF law.

1.2.3 Mechanisms of conduction

The phenomenological jonscher's law can be used to describe the conduction in disordered solids.

Under AC voltage, the complex conductivity of polymer can be written as:

$$\sigma(\omega) = \sigma' - i\sigma''(\omega) \tag{1.12}$$

According to Jonscher's law[71], the AC conductivity σ' is made up of two parts: the frequency-independent part σ_{DC}, and a second part obeying a power law as a function of angular frequency.

The relation is described in equation (1.13), where A, ω and n are respectively temperature dependent parameter, angular frequency and power exponent.

$$\sigma' = \sigma_{DC} + A\omega^n \tag{1.13}$$

Two conduction mechanism are possible, depending on whether it is considered a transport from trapping sites to trapping sites (hopping) or by favoring trapping sites to delocalized states (bands transport). The universal Jonscher's law is similarly manifested in materials subject to electronic or ionic transport, it is therefore often difficult to identify the mechanism.

In original Jonscher's law, the exponent is limited to $n \leq 1$, $0.5<n<0.9$ corresponds to carrier transport: hopping electrons between crystalline and amorphous. Reports on n value higher than unity exist in polymer[72,73], ion-conducting glasses[74], and mixed crystal[75]. Kumar[76] reported recently that n is T and f dependent. It is illustrated that the exponent value $n = 0$ indicates the dc conduction/hopping of the ionic motion, $n < 1$ represents the correlated ion motion while $n \geqslant 1$ represents the caged motion of the ions [76,77].

1.2.4 Deformation under electric field

When an EAP film is submitted to an external electric field, a compress stain in the direction of electric field (S_{33}) and an elongation stain perpendicular to the electric field (S_{31}) could be observed. Fig. 1.15 shows a schematic presentation of the field-induced strain.

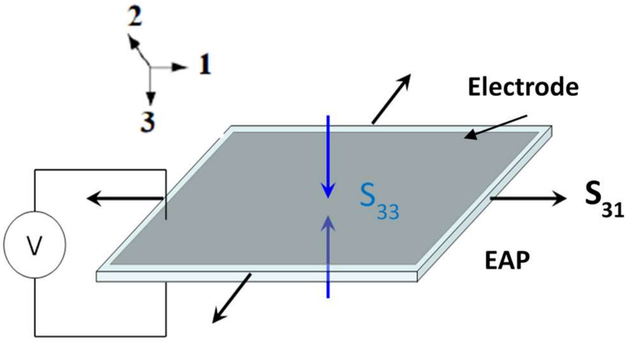

Fig. 1.15. Illustration of the EAP deformation with the application of electric field[32].

The total strain of the dielectric material generated under an electric field could be defined in a tensor form:

$$S_{ij} = s_{ijkl}\sigma_{kl} + d_{kij}E_k + M_{klij}E_kE_l \tag{1.14}$$

The first term is the stain induced by external mechanical stress σ_{kl}, it is related to the elastic compliance. Without external mechanical force, this term could be ignored. The second is the linear strain response to external electric field E_k, it is attributed to the inverse piezoelectric effect of material. This term is equal to 0 for non-piezoelectric polymers such as polyurethanes. The last term is the field induced-strain, which is quadratic on the external electric field.

In EAPs, two mechanisms can contribute to the strain showing a quadratic dependence on the field : the Maxwell effect and the electrostriction phenomenon. In the litterature there is often a mixing of the two mechanisms which causes confusion. A definition of the two terms can be found in the works of Shkel[78] and Krakovsky[79]: the Maxwell stress originates from the change of the electric field distribution inside the EAPs, or in other words, the coulombic attraction between the charges accumulated on the electrodes; the electrostriction is related to the change of dielectric properties caused by the strain. The electrostriction is an intrinsic phenomenon of EAPs that represents the coupling of polarization and the mechanical response.

In the case of polymeric film with compliant electrodes, the relative strain in the direction of the electric field direction (Δh / h) and in the direction perpendicular to it (ΔD / D) can be expressed as follows [79]:

$$\frac{\Delta h}{h} = -\frac{(1+2\nu)}{2Y}\varepsilon_0\varepsilon_r E^2 + \frac{a_1+a_2(1-2\nu)}{2Y}\varepsilon_0 E^2 \tag{1.15}$$

$$\frac{\Delta D}{D} = \frac{1}{2Y}\varepsilon_0\varepsilon_r E^2 - \frac{a_1\nu - a_2(1-2\nu)}{2Y}\varepsilon_0 E^2 \tag{1.16}$$

where ν, Y, ε_0, and ε_r are Poisson's ratio, Young's modulus, the vacuum permittivity, and the stress-free relative permittivity of PU, respectively. a_1 and a_2 are coeffcients describing the change of EAP dielectric properties with the strain. These coefficients are functions of the thermodynamic parameters (the temperature T, the external field magnitude E and the field frequency f)[80].

The first terms of equations (1.15) and (1.16) are related to the Maxwell effect, and the second terms are related to the electrostriction phenomenon.The two effects lead to a quadratic dependence of the total strain on the square of the electric field. As a consequence, the global effective coefficients M_{33} and M_{31} can be defined as:

$$\frac{\Delta h}{h} = M_{33}E^2 \tag{1.17}$$

$$\frac{\Delta D}{D} = M_{31}E^2 \tag{1.18}$$

In the research of polyurethane, there is great discrepancy between the values reported for the electromechanical coefficient (10^{-19} to 10^{-13} $m^2\,V^{-2}$) [31,33,46,81–91]. Thus, the underlying mechanisms attributed to the electric-field-induced strain differ as well. Some claim that the observed strain mainly comes from only the Maxwell effect [31,41,88], whereas others show an electrostriction origin [30,33,46,78,81,89–91]. Table 1.3 summarizes the range of electromechanical coefficients reported for PU films. In this table, the electromechanical properties are evaluated using either M_{33} or M_{31} depending on the experimental bench. This discrepancy in a few magnitudes calls for a reliable and accurate characterization of the electromechanical performance, so as to address the governing mechanism of the electromechanical coupling in PU.

Table. 1.3. Recent measurements and values of electromechanical coefficients of polyurethane films.

PU Thick -ness	Electrode	Measurement set up	M33 / M31 coefficient ($m^2\,V^{-2}$)	Main mechanism	Ref
76 µm	On contact with Cu	Change in capacitance (PU-air-PU)	1.3×10^{-17} (M_{33})	Electrostriction	78
2 mm	N/A	Double beam laser dilatometer	2×10^{-18} (M_{33})	Maxwell	31
100 µm	Sputtered Au (30 nm)	Bimorph cantilever based dilatometer	1.6×10^{-16} (M_{31})	N/A	82

25 µm	2 samples between 3 tin foil layers	Accelerometer	2.6×10^{-17} (M_{33})	Electrostriction	30
25 µm	Evaporated Au	Double beam laser interferometry	1.8×10^{-17} (M_{33})	Electrostriction	30
25 µm	Evaporated Au	Change of air gap capacitors	1.1×10^{-17} (M_{33})	Electrostriction	30
100 µm	Sputtered Au	Bimorph based dilatometer (PU glued on PZT)	8×10^{-18} (M_{31})	N/A	83
56 µm	In sandwich with Al	Strains optically measured in 3 directions by a laser doppler vibrometer	16×10^{-18} (M_{33})	Electrostriction	81
76 µm	In sandwich with Al	Strains optically measured in 3 directions by a laser doppler vibrometer	74×10^{-18} (M_{33})	Electrostriction	81
200 µm	Au electrode	Keyence LB-662 laser displacement meter	Bending (0.2-0.8 mm)	N/A	84
184 µm	N/A	Interferometer in double beam form	3.78×10^{-18} (M_{33})	Maxwell	88
93 µm	N/A	Interferometer in double beam form	2.64×10^{-18} (M_{33})	Maxwell	88
55 µm	Between 2 metallic disks (hydrocarbon fluid)	Modified Michelson interferometer	7×10^{-16} (M_{31})	Electrostriction	46
0.3 mm	Carbon black	Laser sensor, PU disk between 2 acrylic plates	1×10^{-13} (M_{33})	Electrostriction	33
40 µm	Graphic powder	Diaphragm type actuator	2.5×10^{-17} (M_{33})	N/A	86
100 µm	No electrode	Photonic displacement	0.91×10^{-15} (M_{33})	Electrostriction	91

This question will be dealt with in this thesis research.

1.3 Improvement of actuating performance

1.3.1 Enhancement of permittivity

The permittivity is a critical parameter that controls the electromechanical deformation in actuator mode. Hence, the permittivity determines the electromechanical properties of electrostrictive polymers or dielectric elastomers[38,92–94]. Consequently, increasing the dielectric constant is a convenient way to improve the performance of an EAP actuator, so as for a PU actuator.

To improve the permittivity, diverse approaches such as copolymerization, grafting highly polarizable side chains to the backbones, improving chain mobility by adding plasticizers, obtaining blends or composites could be found in literature for other EAPs[93,95–98], however for polyurethane, the studies remains on the incorporation of fillers.

In nanocomposites, the nature of the fillers shows great impact on their macroscopic properties. In the case of insulating fillers, large quantities are required which in turn gives rise to significant increase in Y, to the detriment of M_{31}. For conductive fillers and especially nano-sized ones, a lower content can be sufficient giving rise to a moderate mechanical reinforcement. With the extraordinary conductivity, carbon-based nanofillers are thus ideal choices for PU composites with higher actuating performance. Research on composites of carbon nanotubes, graphene, carbon black have been reported for actuation applications [99–102].

The different series of carbon-based nanomaterials are displayed in Fig. 1.16.

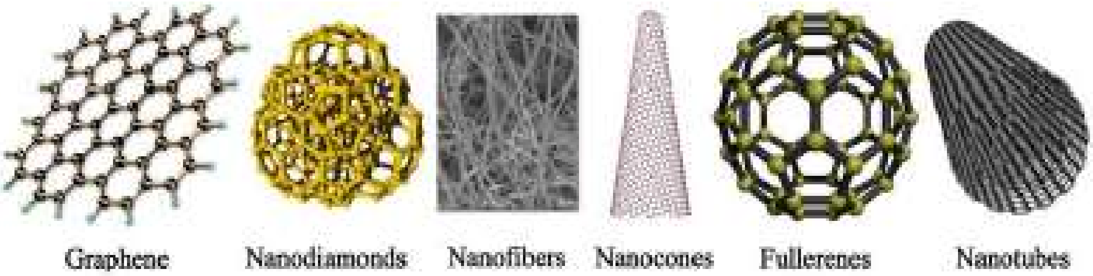

Fig. 1.16. Carbon based nanomaterials[103].

Many authors linked the beneficial effect of the conductive fillers to Maxwell-Wagner-Sillars interfacial polarization [63,104,105]. Consequently, it would be interesting to increase the quantity of interfaces. One aspect is to raise the filler content introduced, where the main issue is to preserve the insulating characteristic of the composite. Another aspect is using fillers with large specific surface area. In this case, graphene is of particular interest, due to the extensive electron mobility and a great specific surface area in favor of interfacial polarization. The incorporation of graphene nanoplatelets into dielectric elastomers for actuator application has attracted enormous research interest in the last years[100]. It is therefore a promising conductive filler for improving the actuating performance of PU.

Except for the nature and shape of fillers, their dispersion state as well as the interaction with the polymer matrix also influence the properties of the nanocomposites. Same as for other nanofillers, due to the agglomeration, graphene nanoplatelets suffer from the difficulty in dispersing into polymer matrix. The surface functionalization of fillers provides a suitable solution. It is reported that the surface functionalization favors the dispersion as well as the cohesion with the polymer matrix[106,107].

1.3.2 Limited effect of nanofillers on the actuating performance

Although incorporating conductive fillers into EAPs remains an effective method to improve the permittivity, during our research, it is remarked that the significant permittivity enhancement does not always lead to the same level of improvement on the electromechanical coupling.

Several examples from literature are presented in Table 1.4.

Table. 1.4. Enhancement of the permittivity versus the enhancement of electromechanical coefficient in several EAP composites.

Polymer	Fillers content	Enhancement of ε_r'	Enhancement of M_{33} or M_{31}	Ref
PU	5 vol% grafted CNTs	40 fold, 0.1 Hz	2 fold, 0.1 Hz, 2.5 MV m^{-1}	108
PI	0.1 vol% SWNTs 0.5 vol% SWNTs	20 fold from0.1% to 0.5%	4 fold from 0.1% to 0.5%, 1 Hz, 0.11 MV m^{-1}	109
PU	1 vol% CB	2 fold, 20 Hz	1 fold, 4 MV m^{-1}	110
PU	1.25 vol% CB	8 fold,0.1 Hz	2 fold, 0.1 Hz, 4 MV m^{-1}	101
PI	0.1 vol% SWNT	41 fold, 0.02 Hz	16 fold, 0.02 Hz, 2 MV m^{-1}	99
PU	3 vol% Gr-CNT	20 fold, 1 kHz	6 fold, DC, 5 MV m^{-1}	111
PDMS	2 wt% thermally expanded GNPs	30 fold,10^3 Hz	3 fold, DC, 15 MV m^{-1}	112

This discrepancy justifies the interest of further research on the role of nanofillers on the EAPs properties: why do they contribute more to the permittivity than to the actuating performance?

Chapter 2. Materials and methods

The aim of this chapter is to present the materials chosen, the elaboration process used to prepare the polyurethane and PU/OFG composite films, as well as the characterizations committed on the films. The characterization techniques from microstructural analysis to macroscopic mechanical, electrical and electromechanical properties were described, with detailed information on the experimental setups and on the measuring conditions given.

2.1 Materials

2.1.1 Polyurethane

The principal polyurethane used in this thesis (Estane 58887 NAT 038, 1.13 g cm^{-3}, 87 shore A) was provided by Lubrizol Company. It is a block copolymer, consisting of 4,4-methylene diphenyl diisocyanate (MDI), 1,4-butanediol (BDO) as hard segments, and poly(teramethylene) oxide (PTMO) as soft segments. The PU was supplied in granules. Some additives were added by the supplier to make properties more stable to the environment, the nature of the incorporated additives is not known. Fig. 2.1 presents the structure of this PU. Table 2.1 shows the main physical properties of PU Estane 58887.

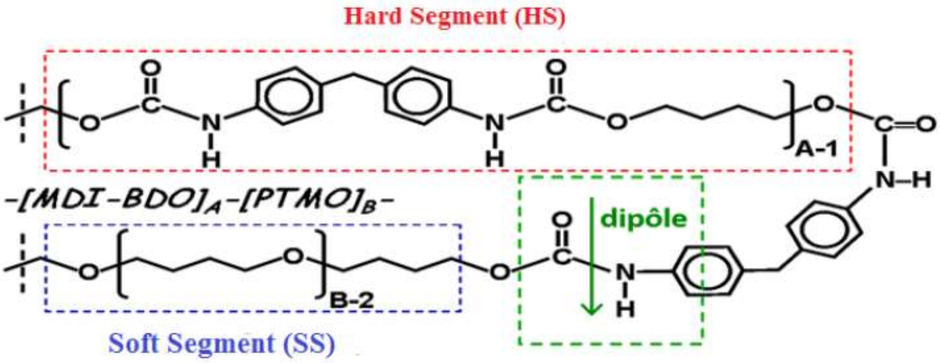

Fig. 2.1. The structure of PU consists of MDI-BO as hard segments and PTMO as soft segments[113].

Table. 2.1. Main physical properties of Estane NAT038 aromatic polyether-based thermoplastic polyurethane from Lubrieol datasheet.

	Measured Values	Method
Hardness	A/1:89 shore A/D	ISO 868
Specific gravity	1.13 g cm^{-3}	ISO 2781
Tensile strength	47 MPa	ISO 527-2/5A/50
Ultimate elongation	570 %	ISO 527-2/5A/50
Tear strength nicked	65 kN m^{-1}	ISO 34-1B
Abrasion resistance	40 mm^{3}	ISO 4649-B
Viscat softening point	79 °C	ISO 306 (A50)

Other two polyurethane (Estane X-4977 NAT 039 and Estane ETE60DT3 NAT 022) with same components but different HS/SS ratio were also used. They were provided by the same supplier as the principal PU, and synthesized by the same process. The two PUs will be abbreviated respectively as PU75 and PU60 in the thesis, while the principal PU abbreviated as PU87.

Because of the different HS/SS content, the three PU show different physical properties. Table 2.2 present some basic properties of these PU concerned by this work [108,114]. The Young's modulus are the values measured in this work, with 26-nm gold electrode on both surfaces. The glass transition temperatures (Tg_{SS}) were determined from DSC measurements.

Table. 2.2. A few properties of the three studied polyurethanes (HS content, density, glass transition temperature and Young's modulus) of the three PU.

	Molecular weight of PTMO (g mol^{-1})	Hard segments (wt%)	Specific gravity (g cm^{-3})	Glass transition temperatureTg_{SS} (°C)	Young's modulus with gold electrodes (MPa)
PU75	**2000**	**26**	**1.07**	**- 66**	**18**
PU87	**1000**	**45**	**1.13**	**-46**	**46**
PU60	**1000**	**65**	**1.17**	**-20**	**185**

2.1.2 Fillers

2.1.2.1 Functionalized graphene nanoplatelets

The graphene nanoplatelets (GNPs, HDPlas^{TM}) used in this study were provided by graphene supermarket. The surface functionalization was achieved by Haydale's plasma process technique, who succeeds to exfoliate mined graphite sheets into even GNPs without damaging the structure. It could also tune the dispersion of GNPs into polar solvent by choosing the plasma[115] [116]. Given the polarity of the solvent, which will be used for composites preparation, GNPs with two different surface functionalization are used in this work: oxygen functionalized graphene (OFG) with carbonyl (C=O), hydroxyl (-OH) and ether (R-O-R) groups and ammonia functionalized graphene (NFG) with primary amine ($-NH_2$), amide ($RCONH_2$) and nitrile (C≡N) groups. Fig. 2.2 presents the SEM images of the functionalized GNPs provided by the supplier.

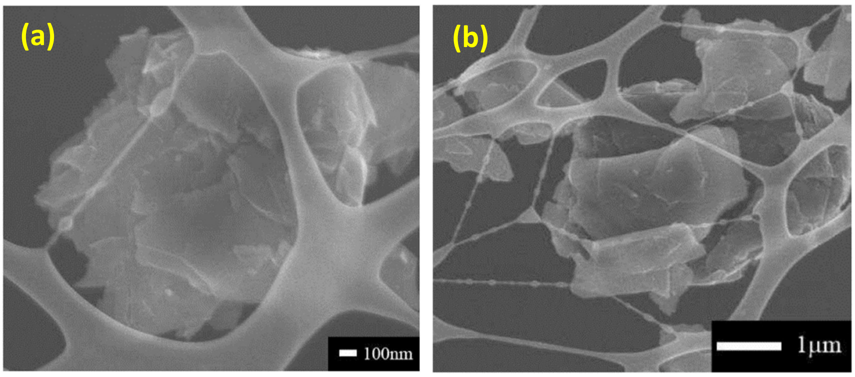

Fig. 2.2. SEM images of (a) oxygen functionlized graphene nanoplateles, (b) ammonia functionalized graphene nanoplatelets[117].

Table 2.3 depicts the typical characteristics of the GNPs.

Table 2.3. Physical characteristics of the graphene nanoplatelets [117].

	Measured Values	Method
Bulk density	215 kg m^{-3}	EN ISO 60
Amorphous carbon	Not detected	SEM/TEM
Specific surface area	20 m^2 g^{-1}	BET Analysis
GNP planar size	0.3-5 µm	SEM
GNP thickness	< 50 nm	SEM

Both OFG and NFG nanoplatelets show good dispersion in the solvent. As shown in Fig. 2.3, after mixing by using a ultrasonic probe for 20 min (will be specified in next section), the mixture of OFG and the solvent, as well the mixture of NFG and the solvent remain stable up to 5 days; no sedimentation was observed. In long terms of one month, OFG is still well dispersed in the solvent, therefore it is chosen as the principal filler in the following study.

Fig. 2.3. Stability of NFG (left) and OFG (right) in the solvent: 0.22 g GNPs in 20 g solvent.

2.1.2.2 Barium titanate nanopowder

The barium titanate powder ($BaTiO_3$, Tetragonal, 99.9%) used in this study were provided by US Research Nanometerials, Inc. Table 2.4 depicts the typical characteristics of the $BaTiO_3$ nanopowder.

Table 2.4. Physical characteristics of the barium titanate nanopowder [118].

	Measured Values	Method
Morphology	Near spherical	SEM
True density	5.85 g cm^{-3}	N/A
Specific surface area	2.06 m^2 g^{-1}	BET Analysis
Aerodynamic particle size	500 nm	SEM
Crystallinity	tetragonal	XRD
Relative permittivity	1000-12000	N/A

2.2 Film elaboration

2.2.1 Pure PU films

The films are prepared by tape casting method. Viscous solutions with the desired composition are previously prepared. For all the solutions, N,N-dimethylformamide (DMF, Honeywell D158550, $\geqslant$ 99%) was used as solvent due to its polar nature and its high capability to dissolve the polyurethane[119]. DMF is a colorless liquid, with a density of 0.94 g cm^{-3} and a boiling temperature of 152-153 °C. However, this solvent is a CMR (Carcinogenic Mutant and Reproductive) product and then all the experiments should always be conducted under a fume cupboard, and with additional individual protection such as a breathing mask if necessary

Firstly, the PU granules were preheated at 80°C for 3 h, following the recommendation of the supplier. A closed system was used for the solution preparation as shown in fig 2.4. 20 g preheated PU granules as well as 80 g DMF were added into a 3-neck spherical flask. One of the necks was used for PU and DMF introduction, another one was used to prevent the DMF from evaporating by a condenser connected to cold-water flow, while the middle neck of the flask was used for mechanical stirring with the help of a half-moon blade. The flask was installed in an oil bath, and heated for 3h at 80 °C accompanied with mechanical stirring until a homogenous, viscous solution was obtained (a photo is shown in Fig. 2.4). The solution was then transferred to a closed jar, and left aside for 24 hours before casting, to get rid of the gas left in the viscous solution.

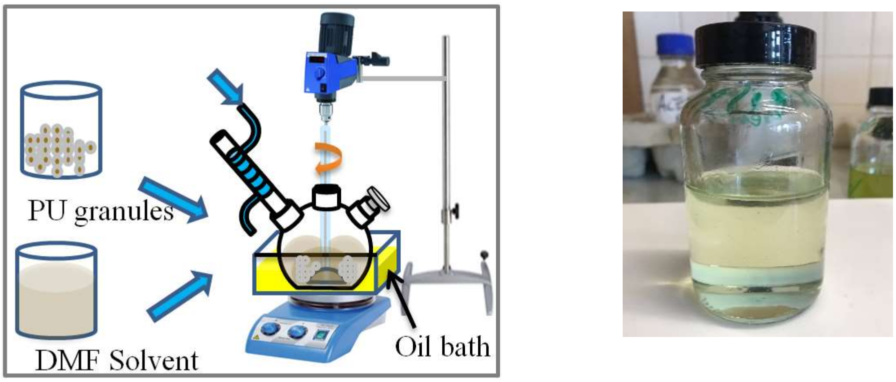

Fig. 2.4. Schematic of the elaboration closed system[108] and example of obtained PU/ DMF solution

With this solution, the PU films were made by a tape casting method. The solution was applied to glass plates by an Elcometer 3700 doctor blade film applicator for a thickness control. Considering the concentration of the solution and the evaporation of DMF, an input thickness of 1000 µm by the Elcometer leads to a final film thickness around 100 µm. The samples were then heated at 60°C for 20 hours in an oven to evaporate the DMF. The dried films were removed from the glass plate and heated again at 125°C, a temperature lower than the melting temperature of PU, for a 3-hour heat treatment. As shown in Fig. 2.5, colorless transparent PU films were obtained.

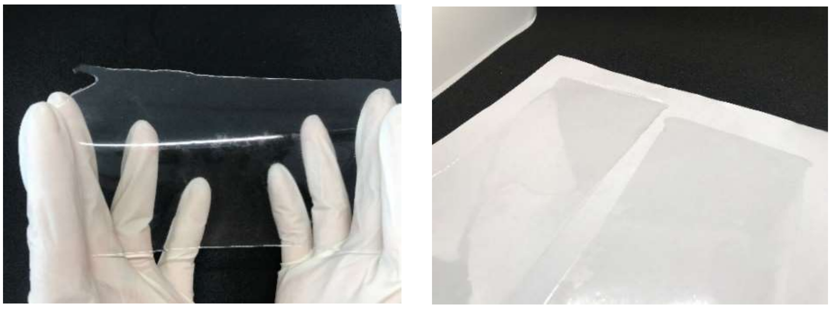

Fig. 2.5. The obtained polyurethane films with a thickness of about 100 µm.

2.2.2 PU composite films

The elaboration of PU composite film is the same as that of pure PU films except for the solution preparation.

According to the desired filler fraction, a certain amount of OFG, NFG or $BaTiO_3$ fillers was weighted and dispersed in 20 g DMF using an ultrasonic processor with a 7-mm sonotrode ultrasonic device (Hielscher UP400S, 400 W, 24 kHz) under a laminar flow hood (ADS Laminaire, PPS 12). The ultrasonic pulse was applied with an amplitude of 70% and 1 cycle . The vial containing the solution was placed during the operation in an iced water bath in order to limit the heating of the solution induced by the ultrasonication. The dispersing time was 20 min in the case of $BaTiO_3$ fillers and 40 min in the case of graphene nanoplatelets.

The fillers/DMF mixture was then added to the flask together with 10 g preheated PU and 20 g more DMF, and the composite solution was prepared as descripted previously for pure PU. Fig. 2.6 resumes the elaboration process of PU/OFG composite film. Fig. 2.7 shows some example of the obtained PU composite films.

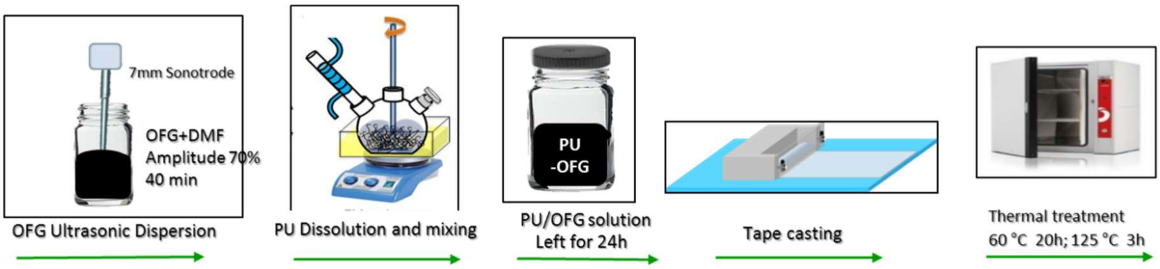

Fig. 2.6. Elaboration process of PU/OFG composite films.

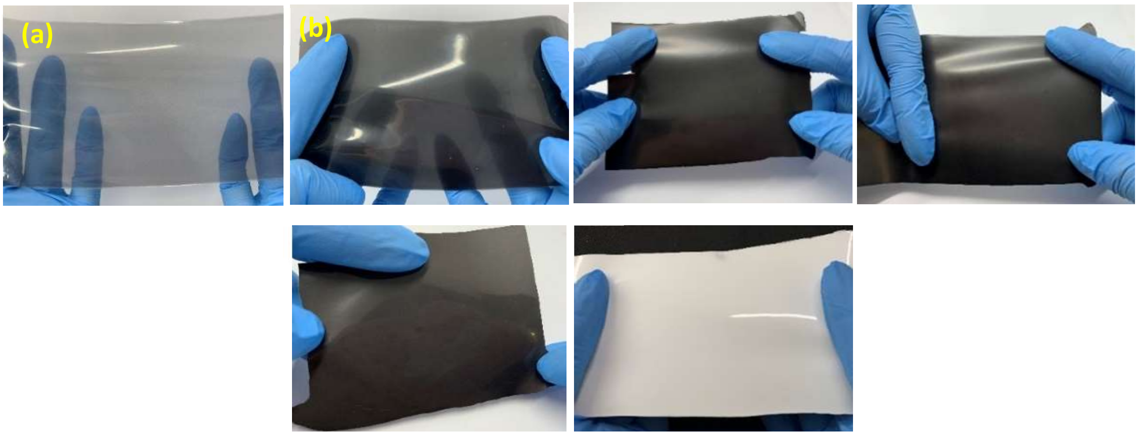

Fig. 2.7. Photographs of obtained PU composite films with a thickness of about 100 µm: (a) 0.17 wt%-OFG, (b) 0.94 wt%-OFG, (c) 5.40 wt%-OFG, (d) 13.13 wt%-OFG; (e) 10.25 wt%-NFG, (f) 20 vol%-$BaTiO_3$.

The thickness of the obtained PU and PU composite films was measured by a mechanical comparator (Florenza), the films were later cut in various shapes and sizes, with and without gold electrode coating, depending on the characterization method.

2.2.3 Deposition of conductive electrodes

For some of the characterizations, particularly mechanical, electrical and electromechanical measurements, conductive electrodes are needed. Thin gold coatings were deposited on both surfaces of the polymer films with a Cressington 208HR sputter coater, equipped with a quartz based thickness controller MTM-20.

The thickness of the gold coating increases with the intensity, the sputtering time and decreases with increased values of the distance between the sample and the target. The current is set to 60 mA, the distance between the sample and the target is fixed to 7 cm and the time varies from 20 to 160 s. The thickness was measured with the help of the quartz crystal monitor.

The thickness of gold deposited on the quartz crystal monitor t_m was determined, and the thickness of gold deposited on the specimen was corrected with the tooling factor (TF), which is calculated from the distance between the target and sample, and the distance between the target and the quartz crystal.

As shown in Fig. 2.8(a), the thickness increases linearly with the sputtering time, with values between 5 and 45 nm. The surface electric resistance was estimated in different parts of the electrode with a multimeter and average values were plot as a function of the coating thickness in Fig. 2.8(b). The resistance exhibit actually the same values all over the surface for all the electrodes. For low thicknesses, namely around 5 nm, large values of resistance were obtained, the deposits were then not sufficiently conductive. Considering thicknesses between 17 and 45 nm, the surface resistance of the electrode decreases with the thickness, with low values (2 to 16 Ω cm) indicating a good conductance of the electrode. With $t_{Au} \geqslant 26$ nm, the benefit of the electrode thickness is minor in terms of the resistance value. Therefore, 26 nm would be the optimal thickness for electromechanical measurement, since it corresponds to good value of conductivity avoiding too much rigidity in the polymer.

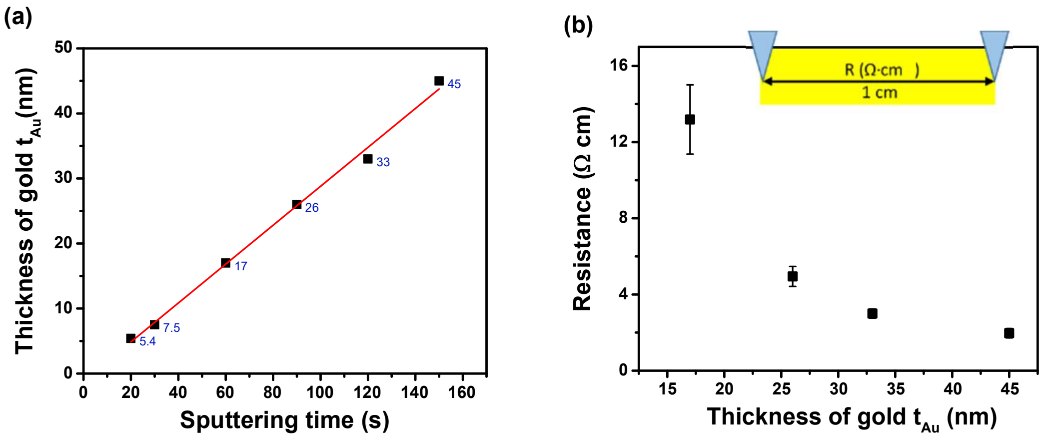

Fig.2.8. (a) The thickness of the gold coating versus the sputtering time; (b) the surface resistance versus the gold thickness

2.3 Characterization methods

2.3.1 Microstructural characterization

2.3.1.1 Scanning electron microscopy

Scanning electron microscopy (SEM) was applied on PU composite films, in order to evaluate the dispersion of nanofillers and the cohesion between the fillers and the PU matrix.

The samples were firstly cryofractured in liquid nitrogen. The observation was carried on the cryofracture surface (cross section).

The PU-OFG composites were observed with a Zeiss Supra 55 VP microscope under high vacuum, at a low accelerating voltage of 1 kV. No conductive coating was applied due to the low voltage values. The PU/$BaTiO_3$ composites were observed with a Hitachi Flex SEM 1000 microscope at 15 kV under a vacuum of 20 Pa and conductive coating.

2.3.1.2 Differential scanning calorimetry

Differential scanning calorimeter (DSC) provides some information on the microstructure of the polymer. The principle is to measure the changes in heat flow as a function of temperature. Exothermic and endothermic processes are visible on the thermograms, depending on the physical transformations of the polymer such as vitreous transition, fusion or crystallization.

The thermal analysis was performed with the Setaram DSC 131 evo calorimeter under nitrogen atmosphere.

The films of PU as well as PU/OFG composites (about 20 mg) were cut into small pieces for a good contact with the bottom part of the crucible, placed in closed 120 µl aluminum crucibles, and precisely weighted. They were cooled from ambient temperature down to -120°C, then heated to 220°c and finally cooled. The heating and cooling rates were performed at 10°C/min. An empty crucible was used as a reference. Calibration was first conducted with mercury, indium, and tin standards for temperature and enthalpy determination. The thermal characteristics were determined with the help of Calisto software.

2.3.2 Fourier transform infrared spectroscopy

Fourier transform infrared spectroscopy (FTIR) was conducted with the help of a Nicolet IS50R Thermo Fisher infrared spectroscopy, equipped with the IS50 ATR multi-range, diamond sampling station. A photo is shown in Fig. 2.9. The scanning range was from 500 to 4000 cm^{-1}. Some test were conducted on both sides of the sample to ensure that the surface condition has no influence on the results.

Fig. 2.9. Nicolet IS50R Thermo Fisher infrared spectroscopy for FTIR measurement.

2.3.3 Mechanical characterization

The Young's modulus of PU and PU composites were determinated with and without gold electrode coating. It should be noted that the modulus is a tensile modulus. Measurement in compression is more delicate on samples of such low thicknesses.

The setup consists of a Newport translation table, a motion microcontroller (XPS), and a 10-N force sensor (Doerler Mesures LC102TC). Films with dimensions of 60 mm in length and 10 mm in width were held on one side with a fixed clamp and on the other side with a mobile clamp. A detailed schematic as well as a photo of the setup as well as are presented in Fig. 2.10. A low strain of 0.5 % was applied to the samples at a speed of 0.1 % s^{-1}. The strain as well as the stress response of the samples were detected by the motion controller and the force sensor. Fig. 2.11 depicts an example of the experimental strain-stress response. Due to the linear response obtained, the Young's modulus of the films (Y) was equal to the slope of the curve.

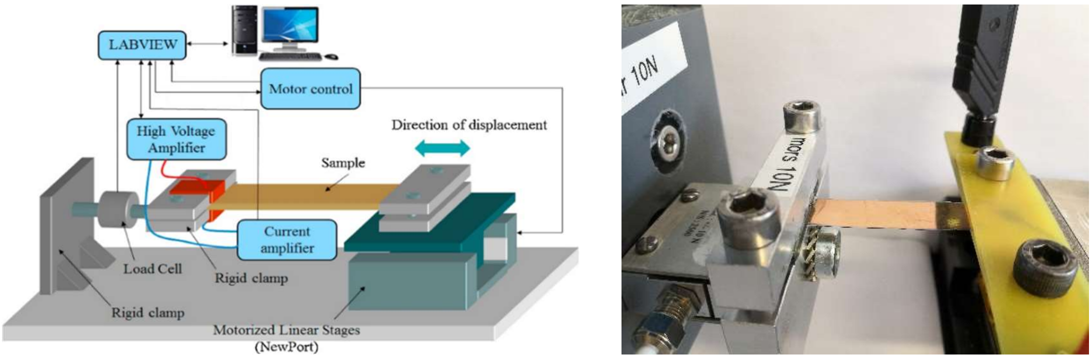

Fig. 2.10. Schematic [36] and photo of the mechanical characterization setup.

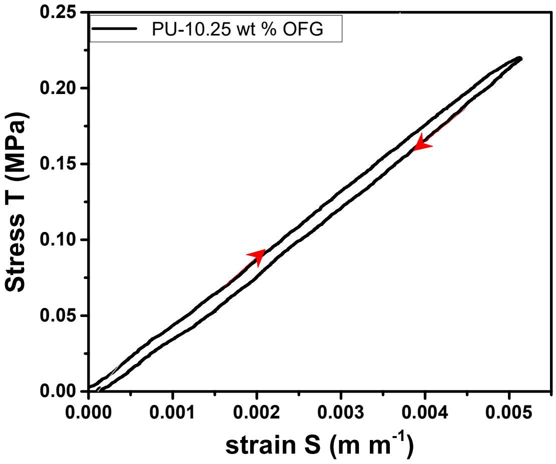

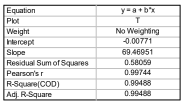

Equation	y = a + b*x
Plot	T
Weight	No Weighting
Intercept	-0.00771
Slope	69.46951
Residual Sum of Squares	0.58059
Pearson's r	0.99744
R-Square(COD)	0.99488
Adj. R-Square	0.99488

Fig. 2.11. Example of the strain-stress curve without the application of electric field.

The mechanical properties of the films were also characterized with and without a DC electric field applied. For the characterization with electric field, films with same dimensions were prepared, and coated with 26-nm gold electrode on both surfaces. A DC voltage was produced by a waveform generator (Agilent 33220A), amplified by a voltage amplifier (Trek 10/10) and sent to the sample, leading to an electric field of 0 MVm^{-1}, 10 MVm^{-1} and 20 MVm^{-1}. A low strain of 0.1 % was applied to the samples at a speed of 0.4 % s^{-1}. The slope of the linear part of the curves were compared to identify the influence of electric field on the Young's modulus of the films.

2.3.4 Electrical characterization

Dielectric spectroscopy is a useful tool to give information on the relaxation modes and on the charge transport.

Dielectric spectroscopy was carried out using a Schlumberger Solarton 1255 impedance/gain phase analyzer and a 1296 dielectric interface (as shown in Fig. 2.12). The real and imaginary part of the permittivity, the conductivity as well as the loss tangent tanδ were determined in the frequency range of 0.1Hz -1MHz under a bipolar AC voltage of 1 V_{RMS}.

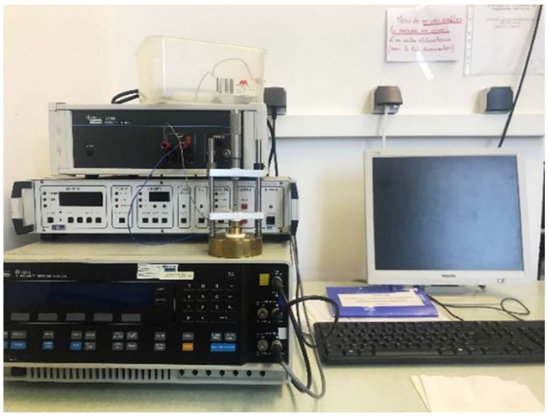

Fig. 2.12. Setup for dielectric spectroscopy measurement.

2.3.4.1 Measuring principles

A sinusoidal voltage $u(t) = Ucos(\omega t$ is applied on the sample placed between two metallic electrodes and the current $i(t) = Icos(\omega t + \varphi$ response is analyzed in terms of amplitude (I) and phase shift (φ).

The complex impedance $\underline{Z}$ is defined in the following equation:

$$\underline{Z} = \frac{\underline{u(t)}}{\underline{i(t)}} = \frac{Ue^{j\omega t}}{Ie^{(j\omega t+\varphi)}} = \frac{U}{I}e^{-j} \qquad (2.3)$$

For a dielectric material, the relative complex permittivity is

$$\varepsilon_r = \varepsilon_r' - j\varepsilon_r'' \qquad (2.4)$$

For a plane capacitor, the complex capacitance C is given by

$$C = \frac{A}{d}\varepsilon_0\varepsilon_r \qquad (2.5)$$

where A is the surface and d the thickness of the sample, ε_0 is the vacuum permittivity (8.85418782 F m^{-1}).

The complex impedance is:

$$\underline{Z} = \frac{1}{jC\omega} \qquad (2.6)$$

leading to

$$C = \frac{1}{j\underline{Z}\omega} \qquad (2.7)$$

and

$$C = \frac{I}{\omega U} e^{j(\varphi - \frac{\pi}{2})} = \frac{A}{d} \varepsilon_0 (\varepsilon_r' - j\varepsilon_r'') \tag{2.8}$$

Finally,

$$\varepsilon_r' = \frac{d}{A\varepsilon_0 \omega} \frac{I}{U} \cos(\frac{\pi}{2} - \varphi) \tag{2.9}$$

and

$$\varepsilon_r'' = \frac{d}{A\varepsilon_0 \omega} \frac{I}{U} \sin(\frac{\pi}{2} - \varphi) \tag{2.10}$$

and

$$\frac{\varepsilon_r''}{\varepsilon_r'} = \tan\left(\frac{\pi}{2} - \varphi\right) = tan\delta \tag{2.11}$$

where $\delta = \frac{\pi}{2} - \varphi$.

The dielectric modulus M” formalism (as shown in equation (2.12)) can be used to highlight relaxation phenomena not observed with ε_r”, especially at low frequencies when high dielectric constant and conductivity values can mask the phenomena[120].

$$M'' = \frac{\varepsilon_r''}{\varepsilon_r'^2 + \varepsilon_r''^2} \tag{2.12}$$

2.3.4.2 Experimental conditions

Three categories of dielectric characterization are carried out: (i) characterization of the frequency-dependent properties at 1 V_{RMS} in a wide frequency range, (ii) investigation of the different relaxations and conduction of PU and composites in a wide temperature range; (iii) characterization of dielectric properties at high electric field and low frequency with well controlled conditions.

To investigate the influence of nanofillers on the relaxation modes of PU, measurements were performed in a wide temperature range using a cryostat (Optistat DN2 Oxford Instruments) and a temperature controller (Oxford ITC503). Measurements were performed in a temperature range of -94 to 80 °C and a frequency range of 0.1 Hz - 1MHz, at 1 V_{RMS} bipolar. Liquid nitrogen was used to reach negative temperatures.

In this thesis, the non-linear curves in frequency domain were fitted with Havriliak-Negami function with the help of WinFIT software. For the analysis of one relaxation process, ε_r’ data were fitted to obtain the ε_∞, and eps”, ε_r” data were firstly removed the DC conduction ($\sigma_{DC}/\varepsilon_0\omega$) and then fitted with the obtained ε_∞, to determine the relaxation time τ and shape parameters α and β.

On purpose of characterizing the dielectric properties of PU and PU composites at the conditions as close as possible to those where actuators are driven, their permittivity were also recorded at high levels of electric field in the range 0.7-10 MV m^{-1} at 0.1 Hz and 1 Hz. A DC signal as well as a unipolar AC signal (examples given in Fig. 2.13) was applied since which are the most common forms for EAPs high voltage applications.

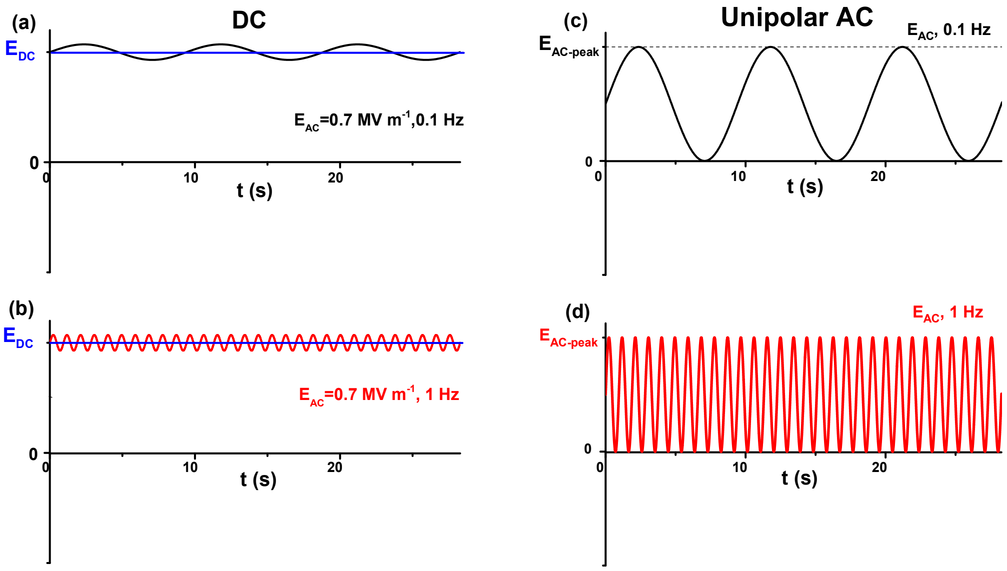

Fig. 2.13. Forms of electric field (10 MV m^{-1} at 0.1 and 1 Hz) used for dielectric characterization: (a), (b) DC with a minimum AC variation, (c), (d) unipolar AC.

The same set up as low field characterization was used, with the help of a high voltage amplifier (Trek 10/10B). A schematic illustration of the high electric field setup is presented in Fig. 2.14.

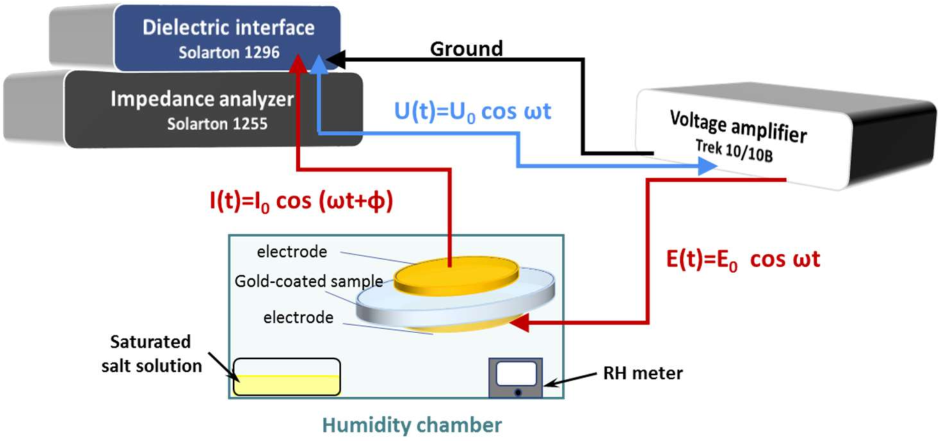

Fig. 2.14. Schematic illustration of the dielectric characterization at high electric field with humidity controlled.

A DC or unipolar AC voltage was generated by a Solarton 1255 impedance analyzer, amplified by a Trek 10/10 amplifier, and applied to the sample. The current I(t) generated by the sample was recorded by Solarton 1296 dielectric interface, and compared with the original voltage sent by the Solarton 1255, to calculate the relative permittivity, conductivity et.al.

During the experiments, it is observed that the permittivity of PU measured at high electric field takes around 200s to reach the stable state (an example is shown in Fig. 2.15). Therefore, for each amplitude, the electric field was applied for 24 cycles, and the impedance was by one cycle integration. In the whole thesis, the values presented are those of the 24th cycle without specification.

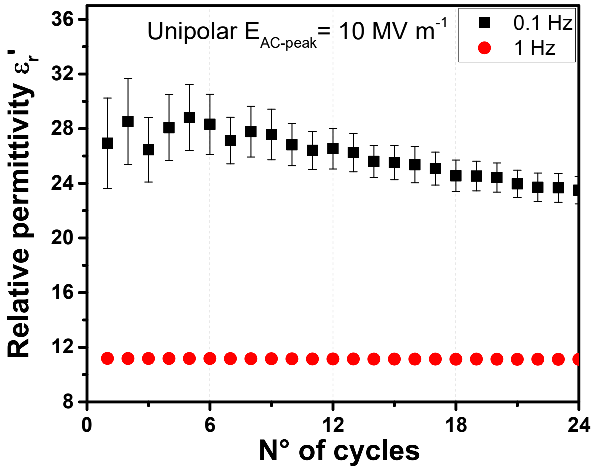

Fig. 2.15. Example of the measured permittivity of PU versus cycles of electric field cycles applied: at 0.1 Hz and 10 MVm^{-1} unipolar AC electric filed.

2.3.5 Electromechanical characterization

Two methods were used to characterize the electromechanical coefficient M_{31} of the PU and PU composite films. The obtained results were compared with each other to validate the measured results.

2.3.5.1 Bender method

A 5-layered structure for Bender characterization of PU and PU composites were prepared as shown in Fig. 2.16(a). The films were coated with gold electrode (17-45 nm) on both surfaces, and then attached to a rigid substrate (Mylar, RS 785-0792, 100 µm) with double-sided tape (3M, ATG 969, 100 µm).

The electromechanical coefficient M_{31} of the obtained cantilever was evaluated with the help of a laboratory-built characterization bench. Fig. 2.16(b) presents the schema of the experimental bench. And Fig. 2.17 shows a photograph of the setup.

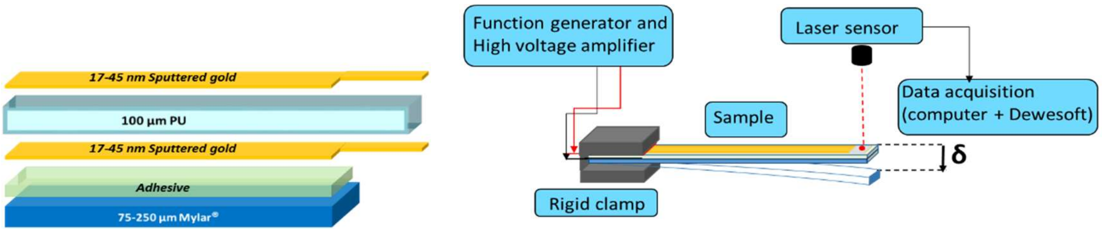

Fig. 2.16. Schematic of the cantilever sample and the setup for Bender measurement.

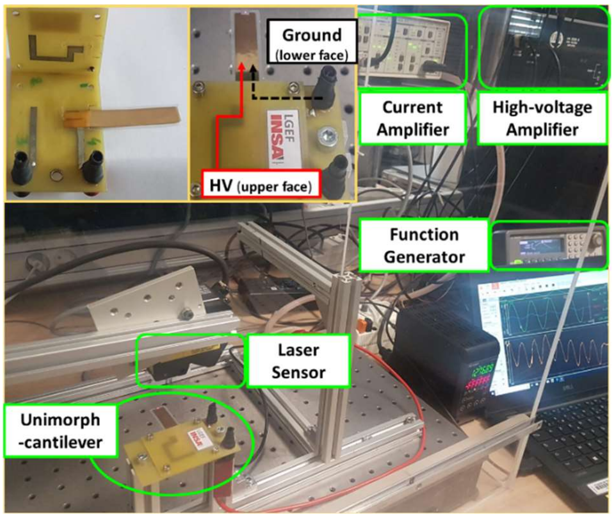

Fig. 2.17. Photograph of Bender setup.

One end of the unimorph cantilever structure was clamped in the device, with the other end free to move. The active area was 40 mm x 10 mm x 0.1 mm.

A unipolar AC electric field at a low frequency (0.1 Hz and 1 Hz, quasi-static) was applied to the sample through a designed system holder with silver tracks (Figure 1b). The voltage was supplied by a function generator (Agilent 33220A) and amplified by a high-voltage amplifier (Trek 609-6). When the electric field was applied, a transverse elongation was generated in the PU film, which forced the cantilever to bend. The sample's tip displacement δ was measured by a laser sensor (3RG7056-3CM00-PF Pepperl+Fuchs). S_{31} was calculated from the measured δ value with equation (2.13) [121], which takes into account the geometry of the device and the material properties:

$$S_{31} = \delta \frac{2t}{3L^2} \frac{A^2B^4+2AB\left(2+3B+2B^2\right)+1}{2AB(1+B)^2} = \delta K_{DS} \tag{2.13}$$

where a two-layer model is considered, where PU and the electrodes compose the first layer, and the substrate is the second one. t is the total thickness of the two layers, L is the active length of the sample, and A, B are, separately, the Young's modulus ratio and thickness ratio of layer 2 to layer 1.

The thickness of the double face adhesive tape is not taken into account in K_{DS}, since it plays only the role of a transfer layer and shows no influence on the deflection. An evidence is that experiments performed with another type of bonding material (a silicone glue Dow Corning 3145) with a similar value of Young's modulus and a double thickness present almost same deflection to that obtained with the adhesive tape ATG969.

M_{31} is calculated from equation (2.14):

$$S_{31} = M_{31}E^2 \tag{2.14}$$

At least four samples of each composition were used for the dielectric, mechanical and electromechanical measurements.

2.3.5.2 Strain-stress method

The strain–stress curves were obtained with and without a DC electric field with the same experimental bench used to determine Young's modulus under electric field in 2.3.2.2 and custom-made conductive clamps. Figure 2.10 shows the setup [36].

The films of 60 x 10 mm^2 were covered with a 26-nm-thick gold electrode on each side. The measurement was taken at strain values near 1% with strain speeds of 0.4 and 4% s^{-1}. The strain-stress curves were recorded with and without a DC field (E_{DC}). The strains that occur with an electric field ($S_{31\text{-on}}$) and without one ($S_{31\text{-off}}$) can be defined as:

$$S_{31-o} \quad = \frac{T}{Y} \tag{2.15}$$

where T is the measured stress, and Y is Young's modulus.

$$S_{31-on} = \frac{T}{Y} + M_{31}E^2 \tag{2.16}$$

S_{31} and M_{31} are then obtained from equation (2.17) in below and equation (2.14):

$$S_{31} = S_{31-on} - S_{31-off} \tag{2.17}$$

2.3.6 Humidity

For some characterizations, the samples were installed in a closed humidity chamber, to investigate the influence of relative humidity (RH) on the dielectric properties of PU and PU composites.

The saturated sodium chloride (NaCl) solution was chosen to create a high relative humidity after reaching the equilibrium [122]. The silica gel was chosen to create a dry atmosphere by absorbing the water in air. The saturated salt solution or silica gel was put in the chamber for at least 5 hours to reach the requested RH levels. High RH level of 60-70%

was achieved with saturated NaCl solution, medium RH level around 45% was achieved with silica gel desiccant (RS PRO, 601-057), and a low RH level around 35% was achieved by heating the silica gel (PROLABO, 285 SC) at 150°C for 30 min (according to the recommendation of the supplier) before usage. The samples were put in the humidity chamber with corresponding RH level 1 hour before characterization. A hydrometer was installed in the humidity chamber to evaluate the real-time humidity level.

Chapter 3. On a better understanding of the electromechanical coupling in polyurethane

Measuring the electromechanical coupling of electroactive polymers (EAPs) is very important for the development of smart materials and adaptive structures. However, the reported electromechanical coefficients show exceptionally large differences. For polyurethane EAP, the values vary from 10^{-19} to 10^{-13} m^2 V^{-2}. In addition, the origin of the mechanism of the strain is controversial. Some argue that the mechanism is due to the electrostatic attraction of free charges on the electrodes, while others claim that electrostriction is predominant.

In this chapter, two methods are proposed for the M_{31} characterization of PU, i.e., Bender method and strain-stress method, with the boundary conditions, the influence of electrodes, and the error sources considered. The validity of the two methods are verified by comparing the M_{31} values obtained. The experimental values are then compared with the values simulated by Comsol, so as to address the mechanism of the electromechanical coupling.

3.1 Permittivity and Young's modulus measurement

3.1.1 Permittivity

The relative permittivity ε_r' of PU was measured on 10 samples with 26-nm gold electrodes on both sides, at 1 V_{RMS} in the range of 0.1 Hz-1 MHz. No stress was applied to the samples, so the measured value is the free-stress permittivity.

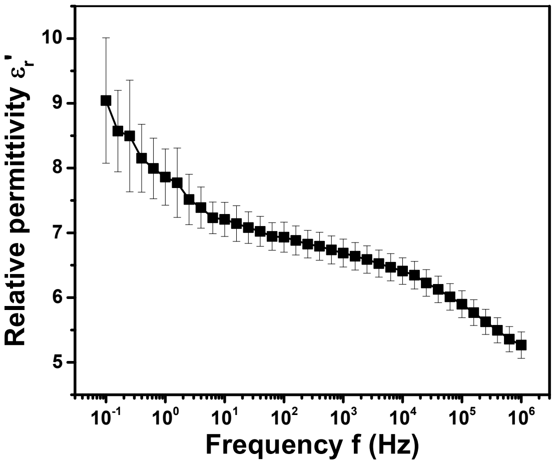

Fig. 3.1. The average permittivity of 10 PU samples.

At 0.1 Hz, the average value of ε_r' was 9.0 ± 1.0. ε_r' decreases when the frequency increases, which is consistent with published papers [123]. This decrease versus frequency is often correlated to phenomena such as DC conduction, Maxwell Wagner Sillars (MWS) polarization, electrode polarization and dipolar relaxations[92,93,102].

Tests were also carried on the rectangular samples for Bender measurements, where similar ε_r' values were obtained. In addition, the values remain the same before and after the rectangular samples were stuck to the rigid substrates by double-faced adhesive, indicating that the electrode was not destroyed by the adhesive.

3.1.2 Young's modulus

Fig. 3.2 presents the Young's modulus of the PU film with and without different gold thickness. Four samples were tested for each thickness. The Young's modulus linearly increases with t_{Au}. Even though the polymer is compressed when the electric field is applied, the Young's modulus was measured in traction because compression measurements are very delicate for thin films.

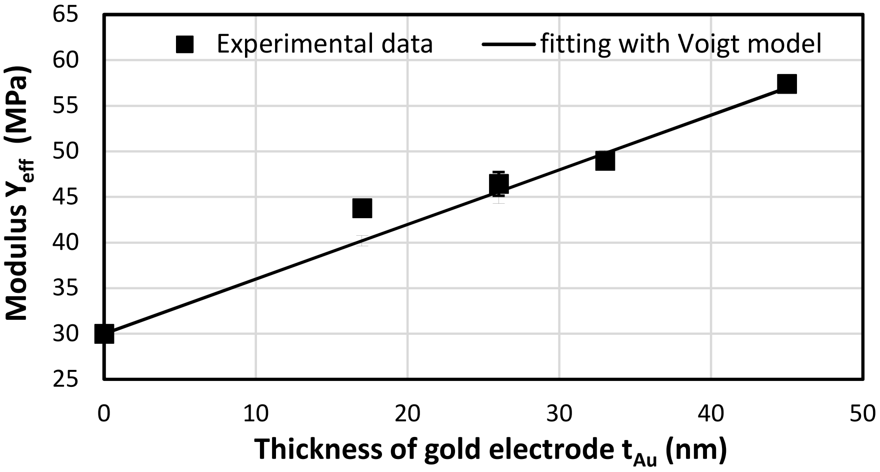

Fig. 3.2. Young's modulus of PU with electrodes versus the thickness of the gold electrodes obtained from the strain-stress curve at a speed of 0.1 % s^{-1} and fitting with the Voigt model.

The effective Young's modulus of the PU with electrodes (Y_{eff}) can be derived from the Voigt model [124]:

$$Y_{eff} = \frac{t_{PU}Y_{PU}+2t_{Au}Y_{Au}}{t_{PU}+2t_{Au}} \tag{3.1}$$

As $t_{Au} << t_{PU}$, equation (3.1) can be written as:

$$Y_{eff} = Y_{PU} + 2\frac{Y_{Au}}{t_{PU}}t_{Au} \tag{3.2}$$

Fitting the experimental result with this model leads to a value of Y_{Au} close to 30 GPa, which is lower than the theoretical Young's modulus of bulk gold (78 GPa). This can be explained by the higher porosity of the sputtered gold film. This obtained value is consistent with previous reports where sputtered or evaporated gold exhibited a lower Young's modulus than the bulk value [125,126].

Despite the porosity, the conductive electrodes are equipotential surfaces.

3.1.3 Young's modulus of substrates

Table. 3.1 presents the measured Young's modulus values of the substrate layers. Four samples were tested for each measurement. The Young's modulus of the substrate decreases with the thickness, which is consistent with the data given by the manufacturer. (Mylar A polyester film datasheet).

Table. 3.1. Young's modulus of the substrate layers versus the thickness and type of substrate

Name	Thickness (μm)	Y (GPa)
Mylar	75	3.37 ± 0.21
	100	3.24 ± 0.70
	125	3.26 ± 0.29
	250	2.57 ± 0.56
Styrene	130	1.2

3.2 Tip displacement of the cantilever

3.2.1 Resonance frequency of the cantilever

Resonance phenomenon is observed during the vibration of a cantilever beam [127,128], and the resonance frequency could be determined with the help of the physical parameters of the cantilever[129]. To guarantee that the measured tip displacements in following sections report the static EAP strain, the resonance frequency was determined by Comsol simulation as well as experimental test.

A 3D geometry was taken for the simulation. Only a two-layer model was used so the resolution of the mechanical equation would not be too complex, since the thickness of the electrode layer is considered as negligible compared to the polymer and substrate layers. Nevertheless, the electrode influence was considered by using the Young's modulus values of the gold coated polymer (see Fig. 3.2). The double face adhesive layer was neither taken into consideration: the tape has only a role of cohesion between the polymer and the substrate and behaves as a transfer layer. According to the Comsol simulations, the deflections are similar with a 2-layer or a 3-layer structure. Solid mechanics physics was used.

The polymer with electrodes and the substrate were modeled as isotropic materials (linear elastic materials for solid mechanics physics). The two materials were connected by a union to ensure the continuity of the boundary conditions.

A physics controlled mesh with tetrahedral elements and fine element size were used. Element size is extensively lower than the characteristic wave length of the fundamental bending mode. The boundary conditions were chosen to be as close as possible to the experimental conditions. The structure was mechanically clamped at one end, while the other part of the cantilever was free to bend. The initial values were u=0 and $\partial u / \partial t = 0$ (structural velocity field).

Eigenfrequency analysis was applied, and it leads to a frequency of 12.75 Hz for the first flexion mode.

Experiment was carried out with a classic cantilever structure for Bender measurement. A unipolar AC electric field ($E_{AC\text{-}peak}$= 12 MV m^{-1}) was applied in a frequency range 0.1 -17 Hz. The experimental resonance frequency for this cantilever is about 12 Hz, in good agreement with the simulated value.

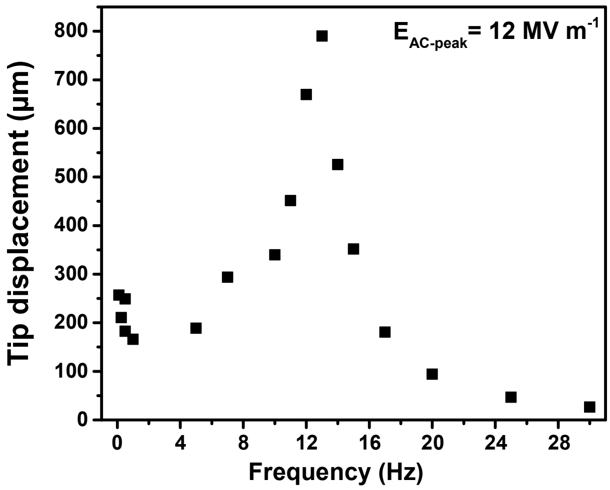

Fig. 3.3. Experimental tip displacements of the cantilever versus frequency.

Therefore, at 0.1 Hz and 1 Hz where the PU films will be characterized in the following sections, the tip displacements are not influenced by the structural resonance since the resonance frequency is far away.

3.2.2 Bender measurement

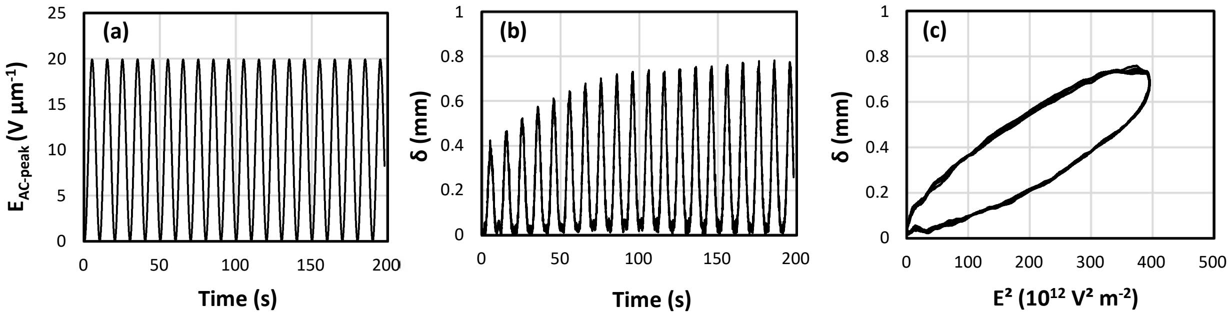

Fig. 3.4. Example of bender measurements at 0.1 Hz: (a) electric field applied to PU with electrodes applied and tip displacement versus (b) time and (c) the square of the electric field.

Fig. 3.4 presents a typical electric field signal applied to the polymeric film in bender measurements, and Fig. 3.4(b) shows the resulting tip displacement versus time at a frequency of 0.1 Hz under 20 MV m^{-1}. The displacement amplitude increases with time and becomes stable after 15 cycles. To ensure that steady state was achieved, 20 cycles were systematically applied to the sample before recording up to four cycles.

Fig. 3.4(c) presents the real-time tip displacement as a function of the square of the electric field. The results shows hysteretic behavior. The maximum displacement was measured. The measurements were performed on 10 cantilevers at different electric fields ranging from 5 to 25 MV m^{-1}. The average value and standard deviation of the maximum tip displacement were then calculated for each field value. The results are plotted versus the square of the electric field in Fig. 3.5.

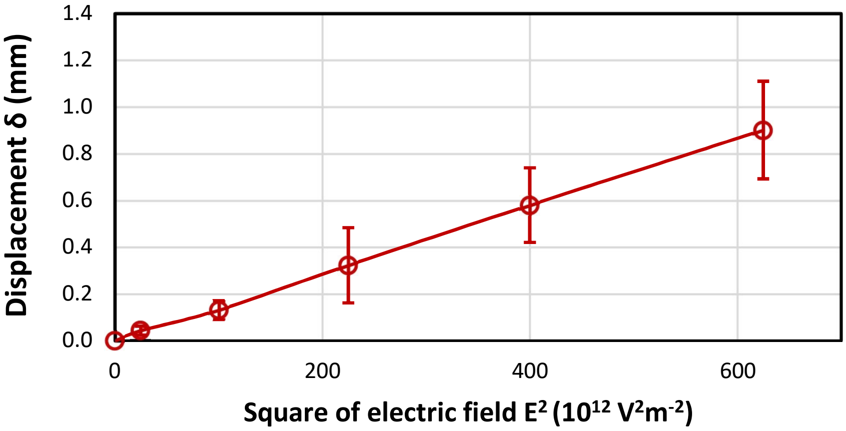

Fig. 3.5. Mean tip displacement versus the square of the electric field from 10 cantilevers tests.

3.2.3 Comsol simulation

Electromechanical forces were used for multiphysics simulations that take into account electrostatic and mechanical physics. The permittivity used in the model was the previously measured free stress value. The same mesh and boundary conditions as described in 3.2.1 were used. Tests with finer element size led to the same results.

For the electrostatics physics, charge conservation for solid material type was applied on the two layers (substrate and polymer) and zero charge (n D = 0) was applied on all boundaries except the upper side of the polymer. The lower side of the polymer, in contact with the substrate, was the ground electrode (electric potential V_0= 0), and a V potential (terminal) was applied to the upper side. The initial values were V=0. Previous experimental measurements were conducted and showed that a DC field and an AC field with a frequency of 0.1 Hz led to the same measured deflection amplitude for the PU. A physics controlled mesh and fine element size were used.

Fig. 3.6 presents the simulated deflection along the cantilever for different values of the electric field, using the measured data for a gold electrode of 26-nm thickness and a Mylar substrate of 100-µm thickness. The deflection increases with the electric field and reaches 0.7 mm at 25 MV m^{-1}.

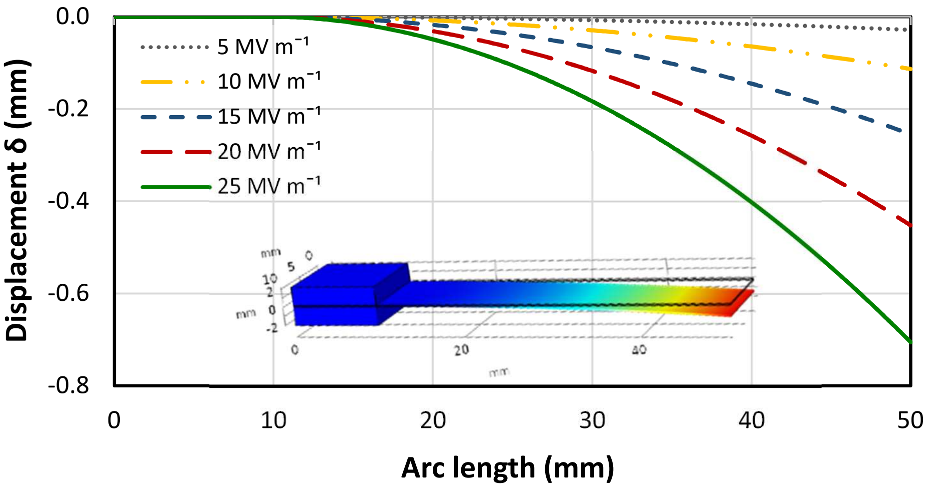

Fig. 3.6. Simulated deflection along the cantilever for electric fields varying from 5 to 25 MV m^{-1}.

Considering the variation of the experimental data, simulations were performed for different values of input parameters. For the input parameters, following factors must also be considered: the permittivity was measured at low electric field, and Young's modulus was measured in traction instead of compression.

This leads to the range of values for t_{sub}, Y_{sub}, Y_{PU}, and ε_{PU} parameters presented in Table. 3.2. The simulations were performed with the 16 possible combinations of the maximum and minimum values of the four parameters. t_{PU} and Y_{sub} are found to have very low effect on the deflection values.

Table. 3.2. Test results of a various ranges of input parameters for Comsol simulations.

	Measured values	Range of values	Values for maximum displacement	Values for minimum displacement
t_{sub} (µm)	100	95-105	95	105
Y_{sub} (GPa)	3.24	3 - 4.5	3	4.5
Y_{PU}(MPa)	45	45-70	45	70
ε_{PU}	9.0	7 - 13	13	7

3.2.4 Comparison of measured and simulated tip displacements

The results of the three simulated tip displacements are plotted in Fig. 3.7 using measured values as input parameters and two other sets corresponding to the maximum and minimum tip displacements. The tip displacement measured by Bender method is compared with the simulated range.

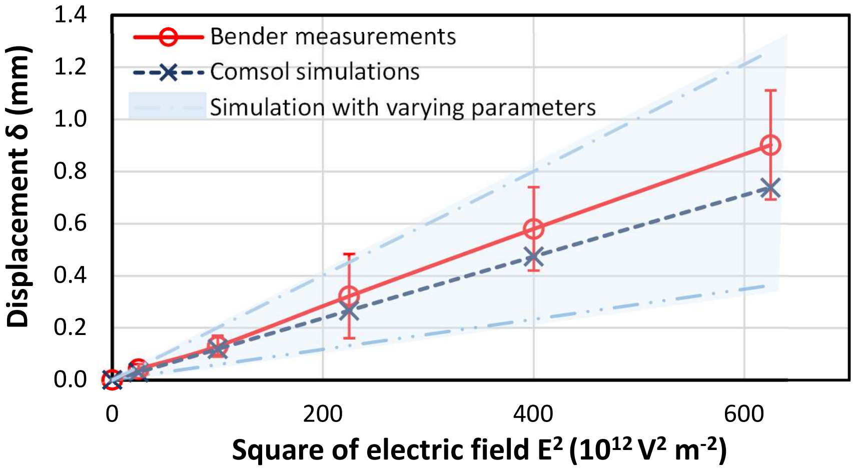

Fig. 3.7. Tip displacement obtained from experimental bender measurements and Comsol simulations with parameters shown in Tab. 3.2.

The tip displacements vary linearly with the square of the field, which is consistent with the Maxwell and electrostriction effects [79,130]. Considering the error bars, it is reasonable to consider that the simulation results are very close to the experimental ones. These results imply that the Maxwell mechanism plays a substantial role in the electromechanical coupling of PU films with electrodes.

3.3 Determination of electromechanical coefficient M_{31}

3.3.1 Bender method

3.3.1.1 Possible error sources in K_{DS}

To extract the measured M_{31} from the previous average tip displacement, S_{31} was calculated using equation (2.18). The factor K_{DS} depends on the thicknesses and mechanical properties of the two layers. Considering the possible deviation of measured thickness and Young’s modulus from the real values, a range of these parameters was tested to determine the K_{DS}. Table. 3.3 presents the results of the possible values of K_{DS}.

Table. 3.3. Influence of material parameters on the value of the factor K_{DS} used in the calculation of S_{31}.

	Measured values (K_{DS}=0.853)	Range of values	Parameters leads to K_{DS} max=1.262	Parameters leads to K_{DS} min=0.509
t_{sub} (µm)	100	95-105	105	95
Y_{sub} (GPa)	3.24	3-4.5	4.5	3
t_{PU} (µm)	100	95-105	100	100
Y_{PU} (MPa)	45	45-70	45	70

S_{31} was then been calculated using the experimental value of K_{DS} and its maximum and minimum values. The results are presented in Fig. 8. The strain shows a linear dependence on the square of the electric field, and the coefficient M_{31} was then determined from the slope of the line. Considering the dispersion of the experimental deflection, the mean experimental value is $1.1 \pm 0.35 \times 10^{-18}$ $m^2 V^{-2}$. When adding uncertainty to the parameters used for the K_{DS} calculation, M_{31} can vary from 0.5 to 2.3×10^{-18} $m^2 V^{-2}$. The obtained M_{31} range is way more precise than the M_{31} or M_{33} reported in literatures [33,82,83,91].

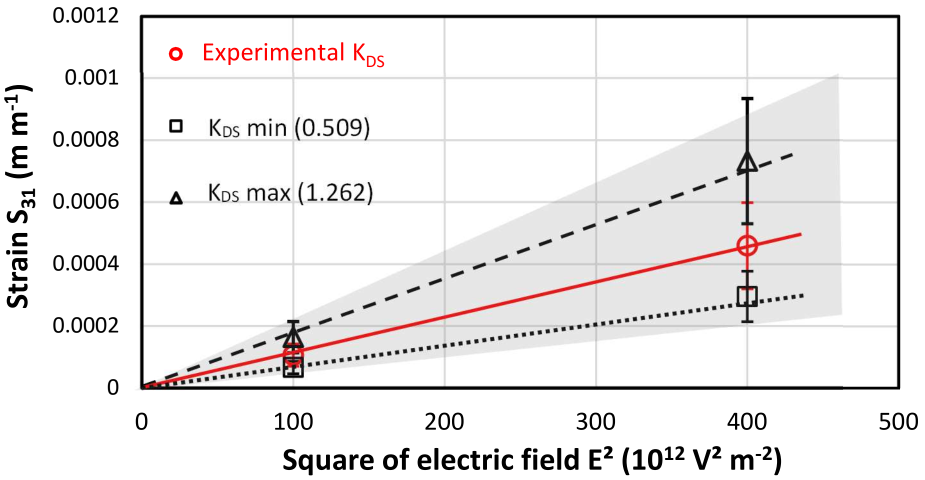

Fig. 3.8. S_{31} strain from bender measurements and different K_{DS} values with the parameters shown in Tab. 3 (0.1 Hz).

3.3.1.2 Impact of substrate

To validate the bender measurement method for the characterization of the PU with electrodes, M_{31} was determined using various Mylar thicknesses of 75 to 250 µm and styrene substrates. Fig. 3.9 presents the tip displacement and the curves of K_{DS}, S_{31}, and M_{31} versus the substrate thickness at 20 MV m^{-1}. The results are the averages of at least three samples.

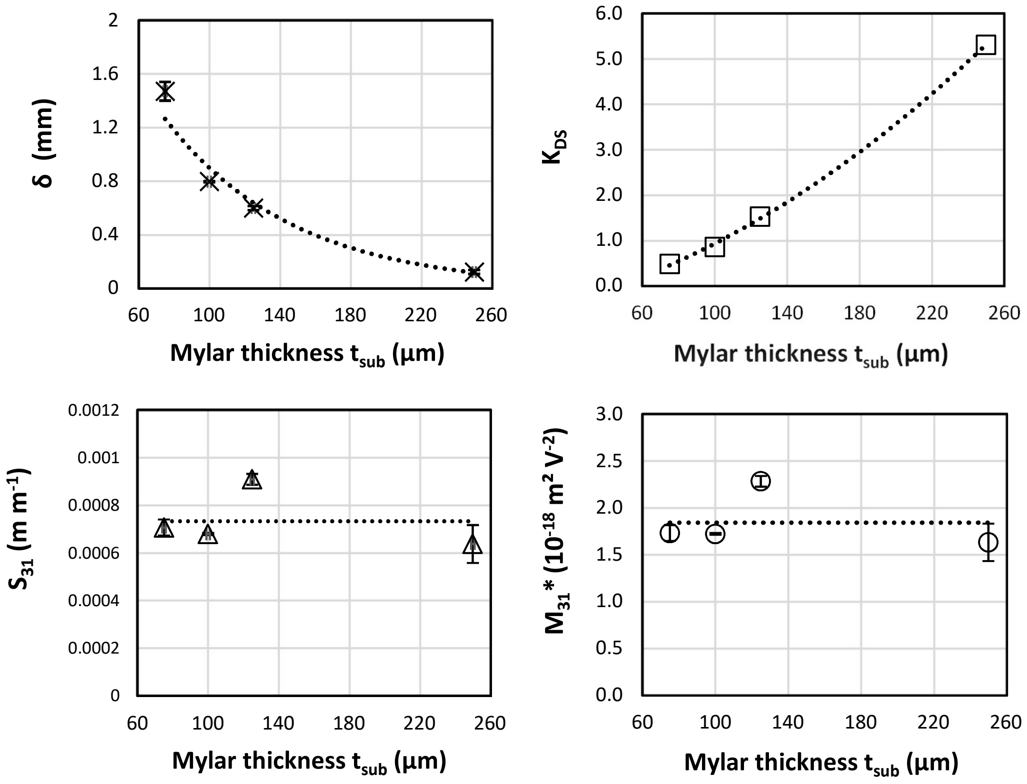

Fig. 3.9. Tip displacement, K_{DS} factor, S_{31} strain, and M_{31} coefficient as a function of the Mylar substrate thickness at 0.1 Hz and 20 MV m^{-1}.

As expected, the tip displacement decreases and K_{DS} increases with the Mylar thickness due to the stiffness enhancement of the cantilever. S_{31} and M_{31} show very similar values regardless of the Mylar thickness. Taking into account that the measurement method is not very accurate, as seen before, the M_{31} coefficient is considered independent of the substrate thickness.

A softer substrate was also tested. For a styrene substrate with a thickness of 130 µm and a Young's modulus of 1.2 GPa, M_{31} was estimated as 1.33×10^{-18} m^2 V^{-2}, which is very close to the value of M_{31} obtained with a Mylar substrate. The M_{31} coefficient is independent of the substrate type in the range examined.

3.3.1.3 Impact of electrode thickness

The influence of the gold electrode thickness was tested using the same calculation method and Young's modulus values from Fig. 3.3 for the gold electrode films. Fig. 3.10 shows the M_{31} coefficient versus the gold thickness. The value remains stable (M_{31}=1.5×10^{-18} m^2 V^{-2}) independently of the electrode thickness.

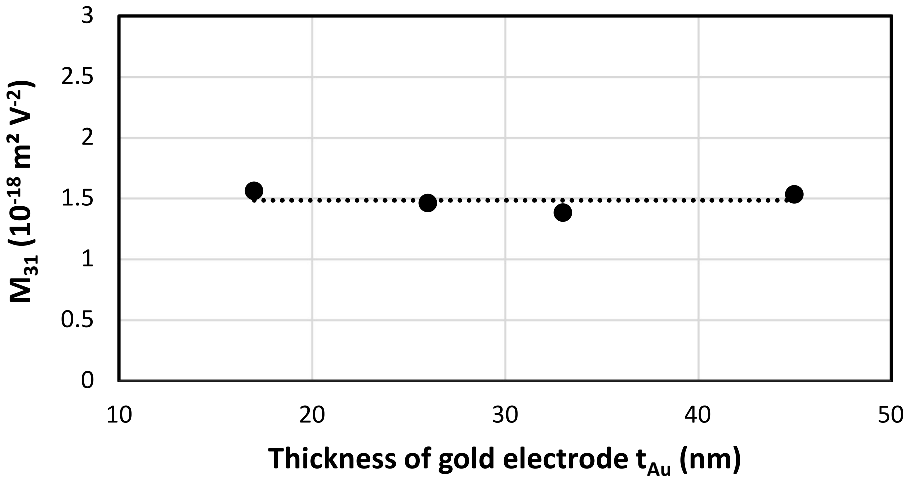

Fig. 3.10. M_{31} coefficient versus gold thickness from bender measurements at 0.1 Hz.

These results highlight that the bender method is a convenient way to estimate the field-induced properties of polymer films with electrodes applied, that the M_{31} obtained is independent on the physical structure of the cantilever sample. The factors who could influence the accuracy of bender measurement are the deviations in thickness and Young's modulus measurements.

3.3.2 Strain-stress method

The same types of gold-electrode PU films were tested using the strain-stress method. The main advantage is that the PU with electrodes is characterized directly without the need to stick the film to a substrate. Fig. 3.11 presents the curve of the input strain with respect to the detected stress at 0, 10, and 20 MV m^{-1}.

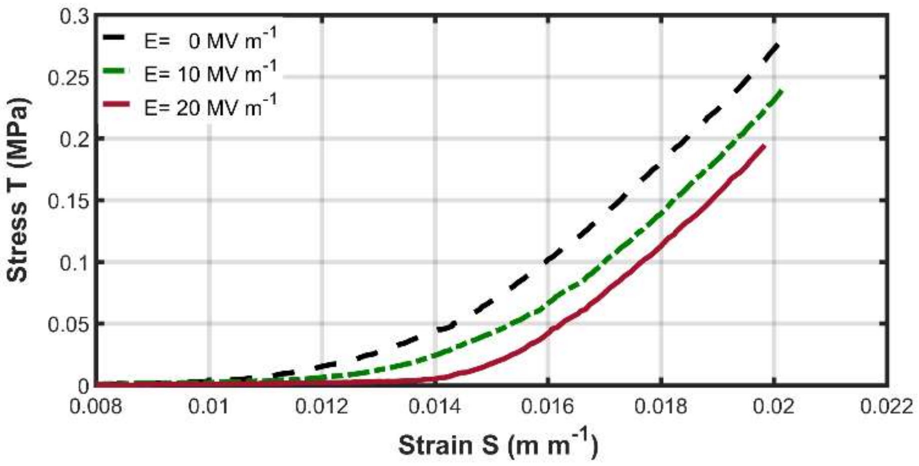

Fig. 3.11. Strain-stress measurements of PU with electrodes at 0, 10, and 20 MV m^{-1}.

For lower values of strain, a plateau is observed until the sample starts to be stressed. Afterwards, the stress varies linearly with the applied strain, regardless of the electric field. The slope of the curves is also independent of the electric field, which means that the Young's modulus does not depend on the electric field value.

A shift of the strain appears between the curve at 0 MV m^{-1} and the one at 10 MV m^{-1}, and a larger one appears at 20 MV m^{-1}. These shifts correspond to the field-induced strain, S_{31}, according to equation (2.17). Fig. 3.12 shows the resulting S_{31} values from four samples.

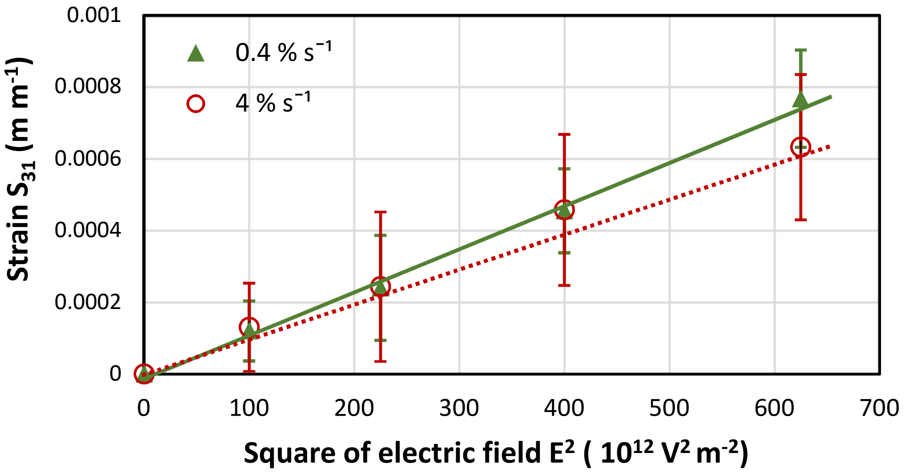

Fig. 3.12. S_{31} strain versus the square of the electric field of PU with electrodes from stress-strain measurements at 0.4 and 4 % s^{-1}.

The value of S_{31} is linear with respect to the square of the electric field and is independent of the strain speed. M_{31} was calculated from the slope of the curve, and the average value is 1.2 × 10^{-18} m^2 V^{-2}.

3.4 Comparison of the measured and simulated M_{31}

Table. 3.4 presents the experimental values of M_{31} obtained from the two experimental methods, and the theoretical Maxwell effect (the first term of equation (1.16)). The Maxwell contribution was calculated with the experimental ε_{PU} and Y_{PU} values considering their varying ranges (i. e., 7-13 for ε_{PU}, and 45-70 MPa for Y_{PU}).

Table. 3.4. Electromechanical coefficients obtained from bender, strain-stress method and Maxwell contribution

	M_{31} (m^2 V^{-2})
Bender method	**0.5–2.3 × 10^{-18}**
Strain-stress method	**0.6–1.5 × 10^{-18}**
Maxwell contribution	**0.4–1.3 × 10^{-18}**

In the case of the bender method, the determination is less accurate for the errors introduced during the calculation. The errors mainly come from the uncertainties in the input parameters used for the K_{DS} determination. On contrary, in the strain-stress remarks, the M_{31} coefficient is directly obtained from measurements without intermediate calculations. However, it is more difficult to capture the field-induced strain when low electric field (e.g., 4 MV m^{-1}) is applied due to the sensor accuracy.

Nevertheless, both two experimental methods lead to similar M_{31} values near 1 × 10^{-18} m^2 V^{-2}, and the experimental values show a range close to that of the Maxwell contribution. It has always been controversial for the electromechanical coupling mechanism, and many authors argued an important contribution of electrostriction[31,46,90,91]. The work in this chapter proved the major contribution of the Maxwell effect in PU.

3.5. Summary

In this chapter, two methods of measuring the EAP electromechanical coefficient: the bender and strain-stress measurements were validated. The methods were used as intrinsic characterizations of the EAP electromechanical coupling behavior. The origins of the uncertainties of the values were discussed.

The experimental deflection value of the unimorph PU samples obtained by bender measurement was compared with the Maxwell deflection simulated by Comsol. It is found that the experimental value is in the range of the simulated Maxwell deflection, so it is concluded that Maxwell mechanism plays a substantial role in the electromechanical coupling in PU films.

Similar M_{31} values were obtained by the two methods. Therefore, the magnitude of the M_{31} electromechanical coefficient of the PU film is confirmed in the range of 0.5 to 2.3 × 10^{-18} m^2 V^{-2}, more precise than that reported in literatures. The experimental results support the major contribution of the Maxwell effect to the total electromechanical coupling.

To further increase the accuracy, the next step is to determine the dielectric and mechanical properties of PU films under conditions that are close to bender measurements. According to the Comsol simulation, the dispersion of the relative permittivity shows a significant effect on the simulated deflection, so testing the permittivity under the bender measurement conditions is predicted to help decreasing the simulation dispersion.

Chapter 4. Origins of the dispersion of polyurethane electromechanical coefficients

In the last chapter, it was proved that Maxwell mechanism dominates the electromechanical coupling in PU. However, the experimental coefficient M_{31} exhibits a large dispersion from 0.5 x 10^{-18} m^2V^{-2} to 2.3 x 10^{-18} m^2V^{-2}. Two questions need to be addressed: the dispersion of the experimental coefficient M_{31}, and the underestimation of the electrostatic model to the M_{31} measured by Bender method.

As the electromechanical performance depends directly on the ratio of the dielectric constant on the Young's modulus, questions were raised about how the electric field can affect the dielectric (ε_r', σ') and the mechanical (Y) properties. It has been already shown that the Young's modulus is independent of the applied electric field. Consequently, this chapter is focused on the electric field dependence of the dielectric properties.

During the thesis, it was also found that the elaboration process and the measurement conditions can have an influence on the properties. A part of this chapter is then devoted to the role of process, humidity and temperature.

4.1 Observed variation of the permittivity

4.1.1 Electric field dependence

Fig. 4.1 shows the relative permittivity values of PU measured under unipolar AC and DC voltage, with a range of electric field (E) 0-10 MVm^{-1}.

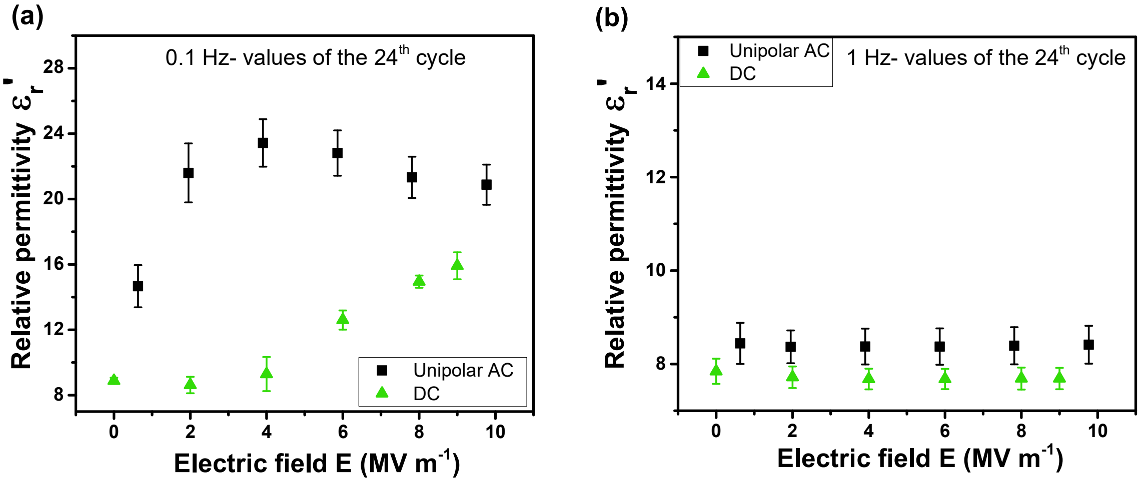

Fig. 4.1. Relative permittivity ε_r' versus electric field under unipolar AC and DC voltage: (1) 0.1 Hz, (b) 1 Hz.

At 0.1 Hz, the dielectric permittivity presents a rather strong variation with the electric field under both unipolar AC and DC voltage, though the tendencies are different. Under unipolar AC voltage, ε_r' increases rapidly from the first electric field applied ($E_{AC\text{-}peak}$=0.7 MVm^{-1}), reaches the maximum value at 4 MVm^{-1}, and then slightly decreases at field higher than 4 MVm^{-1}. Under DC electric field, ε_r' stays unchanged with E_{DC} smaller than 4 MVm^{-1}, followed by a linear increase at higher electric field. At 1 Hz, for both electric field forms, ε_r' values of PU are mostly steady with the increase of E. The electric field has a significant impact only at low frequency. The difference observed at 0.1 Hz between DC field and unipolar AC field could be explained by a different dynamic of the dipole mobility linked to the form of the field. This point has not been investigated in this thesis because the bender measurement was exclusively carried on AC unipolar field. However, it must be seen as a perspective for future works. The difference observed versus frequency could be associated to MWS polarization and/or electrode polarization, which occur mainly in such low frequency region[92,93,102].

Moreover, with the different forms and strengths of applied electric field, a large variation of ε_r' from 8 to 24 was observed, while in the electrostatic model used for M_{31} prediction, only a little range from 7 to 13 was taken (as shown in Tab. 3.2). This could explain the underestimation to the Bender results.

In summary, at 0.1 Hz, for PU, the values of ε_r' measured under high electric field are significantly different from the value at 1 V_{RMS}. In addition, the values depend not only on the strength but also on the form of E. Thus it is important to characterize ε_r' at the same conditions as those where M_{31} are measured. For Bender measurements in this thesis, only unipolar AC voltage was used, therefore the dielectric properties of PU were investigated at the same electric field.

4.1.2 Other sources of the dispersion

At the beginning of the study, the duration of the bending measurement was set up at 240s, because the field-induced strain reached a steady state at this time (as shown in Fig. 3.4). However, during the thesis, unexpected decrease or increase of strains versus time was observed for longer duration of measurements. This observation motivated an investigation of the evolution of permittivity as a function of time for different samples.

Fig. 4.2 presents the evolution of ε_r' versus time from measurements carried out on three different samples (N°1, N°2 and N°3), at 10 MV m^{-1} and 0.1 Hz.

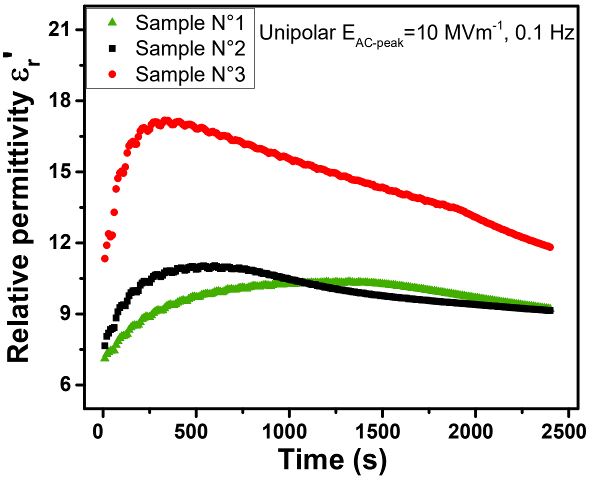

Fig. 4.2. The relative permittivity ε_r' evolution of 3 PU samples versus measuring time

The maximum value of ε_r' depends on the sample, and exhibits a large dispersion (10 to 17), compared to the small one observed at 1 V_{RMS} (between 8 and 10). In addition, the time necessary for ε_r' to reach a relative stable state is different for the three samples. In some cases, more than 2500s are needed to reach the steady state (sample N°3).

The observed dispersion could be probably due to the reproducibility in the film elaboration process, which can lead to a possible modification of the composition and/or the microstructure, or to the measuring conditions (e.g. temperature and humidity). The first assumption is based on the observation that the same elaboration process can lead to samples of different colors, from colorless translucent to pale yellow translucent. The second one came from the fact that the measurements were performed without humidity or temperature controlled.

Therefore, in the following part, factors that could be responsible to the different dielectric behaviors of PU were investigated by varying one parameter while maintaining the other parameters unchanged.

4.2 Identification of the key factors influencing the dielectric and mechanical properties

4.2.1 Elaboration process

4.2.1.1 Dielectric and mechanical properties of PU of different colors

The dielectric behavior of PU-1 (colorless) and PU-2 (pale yellow) were characterized at a humidity level of 67%-69% and at ambient temperature (around 22 °C). The evolution of ε_r' versus electric field ($E_{Ac\text{-}peak}$) of PU-1 and PU-2 is depicted in Fig. 4.3.

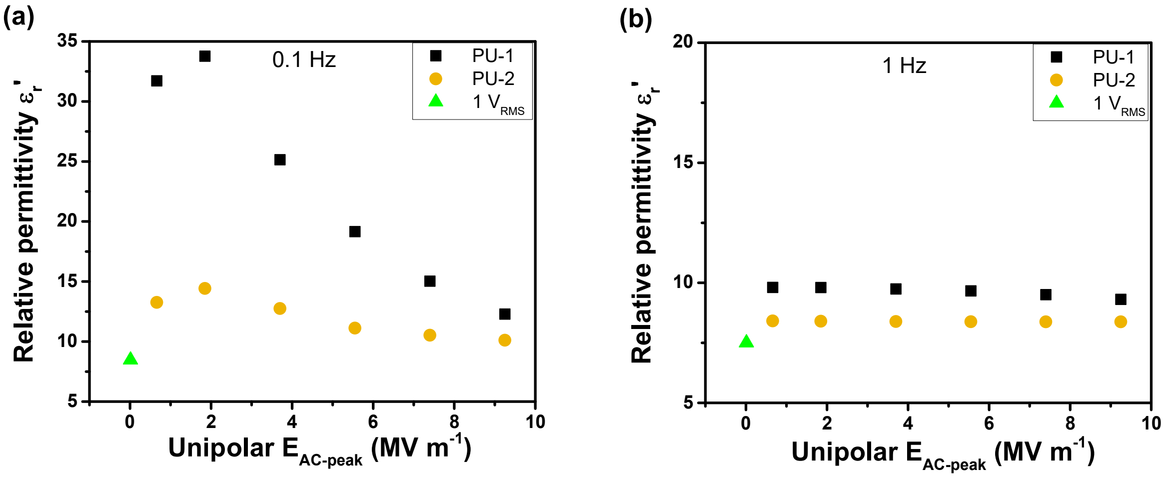

Fig. 4.3 Two types of relative permittivity εr' behavior versus electric field of PU: (a) 0.1 Hz, (b) 1 Hz

At 0.1 Hz, the permittivity of the two PU first shows an increase followed by a decrease from intermediate values of fields, but the values are different. For PU-1, ε_r' reaches its maximum value of 34 at 2 MV m^{-1}, which represents a 4-fold increase compared to the 1 V_{RMS} value. The ε_r' value of PU-2 is lower than that of PU-1 on the full $E_{AC\text{-}peak}$ range, especially at $E_{AC\text{-}peak}$ higher than 2 MV m^{-1}. At 1 Hz, ε_r' of both PU samples at high voltage are only slightly higher than that of 1 V_{RMS}. The values are almost independent of the electrical field level as previously mentioned in paragraph 4.1.

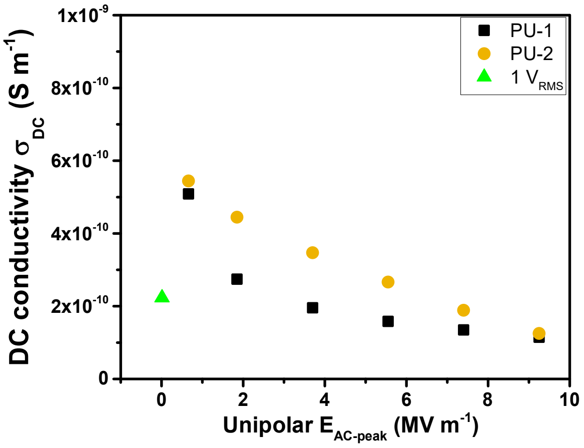

Fig. 4.4. DC conductivity of versus electric field.

The DC conductivity σ_{DC} of PU-1 and PU-2 versus $E_{AC\text{-}peak}$ are presented in Fig. 4.4. It is shown that, contrary to the permittivity, the σ_{DC} of PU-2 is higher than that of PU-1. The DC conductivity measurement has been performed in parallel with the permittivity measurement on expecting a correlation between these two data. In this experiment, the higher permittivity of the colorless PU is associated with a lower σ_{DC}.

Mechanical tests were also performed on colorless and yellow samples. It is observed a slight mechanical reinforcement in the case of pale yellow samples. From the measurements of four sample of same color, the Young's modulus is found to 29±3.7 MPa for colorless PU and 33.5±3.5 MPa for pale yellow PU. In the literature, there is no consensus how the change in the microstructure affect the mechanical properties. Oxidation process can lead either to lower or higher Young's modulus[49].

Based on the different color as well as the different dielectric and mechanical properties versus $E_{AC\text{-}peak}$, it is questionable whether the composition and/or the microstructure of PU have been modified during the elaboration process.

4.2.1.2 Possible modifications of the polyurethane during the elaboration process

The yellowing of PU is often attributed to the thermal and photo oxidation, which is more pronounced at high temperature, and can be initiated by mechanical stress and impurities. As mentioned in 2.1, the PU granules were dissolved in DMF with heating and agitation during 3 h, which makes possible such oxidation process. The PU used in this work is a block copolymer, consisting of 4,4-methylene diphenyl diisocyanate (MDI), 1,4-butanediol (BDO) as hard segments (HS), and poly(teramethylene) oxide (PTMO) as soft segments (SS). In this PU, two groups can be concerned with the photo and thermal oxidation: the aromatic diisocyanate (MDI) and the ether group in the polyol part.

In the ether group, the alpha carbon can lose a hydrogen and form an oxygen radical, the reaction of this oxygen radical with adjacent oxygen or carbon can lead to product a formate or an aldhehyde [131,132].

The oxidation of the central methylene group in MDI can lead to product quinone-imides (as shown in Fig.4.5(a)) [131,133]. Quinones are molecules containing chromophoric groups at the origin of the yellow color.

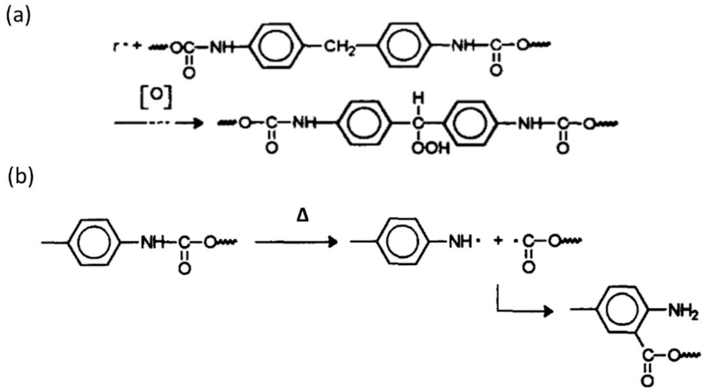

Fig. 4.5. (a) Oxidation of central methylene group and (b) scission of N-C bond[131].

This oxidation can be accompanied with a scission of N-C bond in urethane group, following a photo-Fries reaction (Fig. 4.5(b)) [131,133]. The scission may change the hard and soft segments organization and consequently the microphase separation of HS and SS [134,135].

Fourier-transform infrared spectral studies (FTIR) were performed on several colorless and pale yellow PU samples to have some information about the possible modifications during the elaboration process[136]. Fig. 4.6 presents global spectra obtained from the colorless and yellow PU.

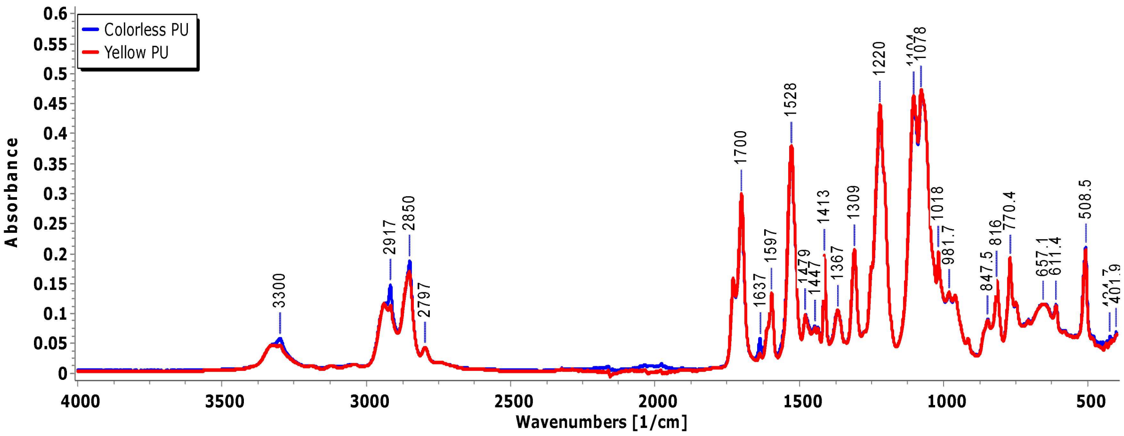

Fig. 4.6. FTIR spectra of colorless and yellow PU.

Globally, same principal stretching bands with same intensities are found in the spectra whatever the color of the PU, indicating no great composition change among the samples. For instance, the stretching bands are near 3300 cm^{-1} for N-H groups, near 2900 cm^{-1} for C-H groups, near 1700 cm^{-1} for C=0 groups and near 1200 cm^{-1} for C-N groups.

For both colorless and yellow PU, peaks at 1597 cm^{-1} and 1637 cm^{-1} were observed, which could be attributed to the presence of quinone group[137]. This interpretation can support that some oxidation mechanisms might have happened during the elaboration process. However, there is not a great intensity change in these peaks depending on the color. It represents that even if the film remains colorless, some oxidation could have happen. It was certainly at an early stage of the color change.

Some slight changes of intensity ratio are visible on the peaks at 1700 and 1740 cm^{-1} (hydrogen-bonded carbonyl (C=O)$_{\text{H-bonded}}$ and free carbonyl (C=O)$_{\text{free}}$), on the peaks at 3300 and 3340 cm^{-1} (hydrogen-bonded amine (NH)$_{\text{H-bonded}}$ and free amine (NH)$_{\text{free}}$), and on the peaks at 1078 cm^{-1} (hydrogen-bonded ester (C=O)OC$_{\text{H-bonded}}$)[138]. For example, Fig. 4.6 presents the absorbance in the range 3450-3150 cm^{-1} and 1180-980 cm^{-1}. These changes indicates possible variation in the state of hydrogen bonding interaction[139], which can modify the microphase separation in PU.

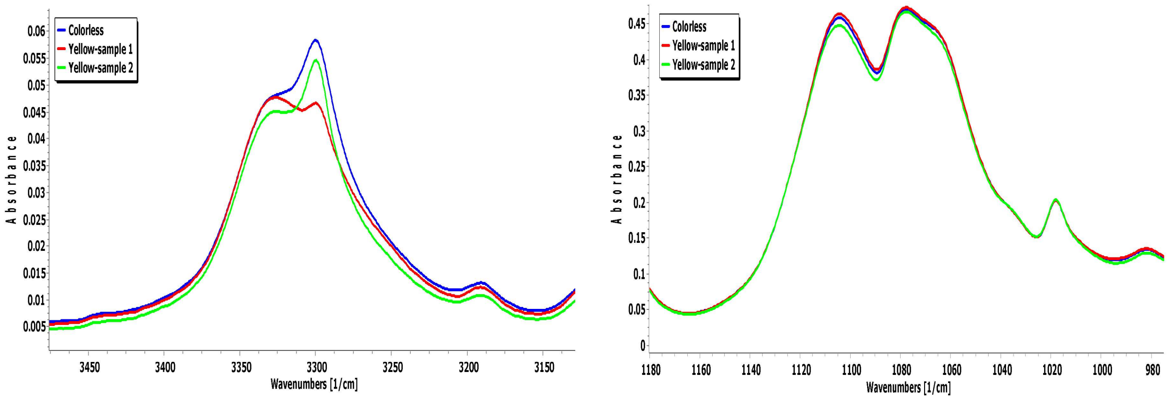

Fig. 4.7. FTIR spectra of colorless PU and yellow PU in (a) amine N-H and (b) ester (C=O)OC.

4.2.1.3 Microstructure of PU of different colors

A DSC analysis was conducted to observe how the elaboration process can impact the microstructure of the PU. Fig. 4.8 presents an example of a complete thermogram of colorless PU and the bimodal endotherms of different colorless and pale yellow samples.

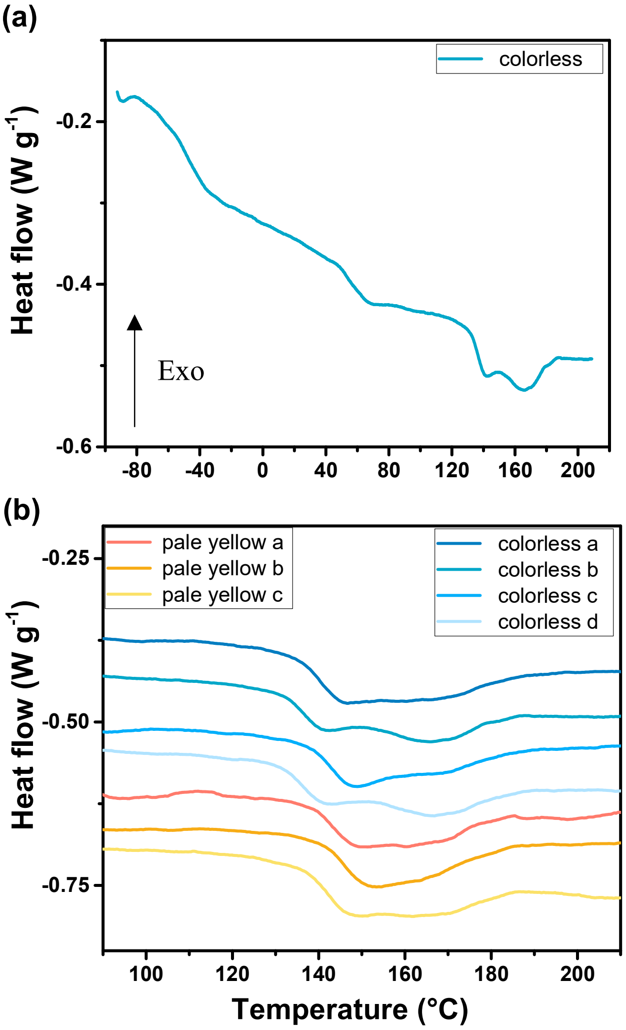

Fig. 4.8. DSC analysis of PU with different color: (a) a complete thermogram of colorless PU, (b) bimodal endotherms of different colorless and pale yellow samples (curve shifted for a better observation).

Three main thermal events could be observed during the temperature evolution. The first thermal event at -40/-50°C was related to the glass transition of the soft segments (SS) in PU. As reported by Martin[140], T_g can be used qualitatively to indicate the amount of hard segment dissolved in the soft domains. Although for PU any quantitative analysis involving T_g has been difficult due to the complex morphology where the microdomain structure can impose restrictions on the motion of soft segments and where the soft domains can be partly crystalline. It is however possible to relate the T_g value directly to the degree of HS-SS mixing, due to the link between HS and SS, which restricts the rotation of SS[141]. When more HS are dissolved in the soft domain, the mobility of SS decreases, and the Tg values become higher.

The endotherm in the range 40-80°C could be related to the glass transition of hard segment microdomains, to local restructuring of hard segment units within the hard microdomains including disruption of short-range order or disruption of SS/HS bonds[143] [144].

The HS T_g interpretation is questionable, as this event was not visible on the second heating run (not shown in the manuscript).

There were two possible interpretations for the bimodal endotherm (T_{m1} and $T_{m2)}$ in the range 130-180°C. The first one was the micro-mixing of non-crystalline or semi-crystalline soft and hard phases followed by the fusion of crystalline HS [143] [145]. The second was the fusion of crystalline HS with the two peaks related to two lengths of HS [140] [146]. In both cases, the increase of the sample crystallinity is linked to an increase of Tm_1 and Tm_2 and/or an increase of the enthalpy of the bimodal endotherm.

The thermal properties of the different samples are listed in Table 4.1.

Table. 4.1. Thermal properties of PU with different colors

	Sample	T_{gSS} (°C)	ΔC_p (mW)	T_{m1} (°C)	T_{m2} (°C)	ΔH_f (J/g)
Colorless PU	**a**	**-42.4**	**1.2**	**148**	**171**	**12.1**
	b	**-43.8**	**1.5**	**143**	**167**	**13.5**
	c	**-47.7**	**1.4**	**149**	**168**	**12.6**
	d	**-50.6**	**1.4**	**140**	**170**	**13.8**
Pale yellow PU	**a**	**-50.2**	**1.4**	**149**	**168**	**11.2**
	b	**-50.4**	**1.3**	**152**	**165**	**12.1**
	c	**-49.8**	**1.3**	**148**	**170**	**13.8**

The T_g was not greatly affected by the elaboration process; only a slight decrease of about 3 or 4 °C is obtained for the pale yellow samples, which can indicate a very small change in the HS-SS mixing [147].

The possible difference in the polymer microstructure is a little more visible on the bimodal endotherm, in terms of shape in the range 130-180°C and of T_{m1} values, as shown in Fig. 5.6(b). The total enthalpy remains the same for the two types of samples, but the micro-mixing of hard and soft phases, and the HS fusion are different. The T_{m1} values are a little higher for the pale yellow group, confirming the small change in the degree of phase separation.

Among the four colorless samples, the parameters show also a dispersion, making it not easy to compare with the pale yellow series. In addition to the elaboration process, we can also ask about the sensibility of such polyurethanes to the humidity. This point will be discussed in a next section.

In view of the results obtained with the various characterization techniques described above, it is hard to conclude without any doubt on the effect of the composition variation on the dielectric properties. In addition, as it has been recalled, there is an uncertainty on the PU composition. Indeed, some additives were used by the industrial manufacturer, and it was not possible to obtain the list or some information about them. Additives can behave in complex ways and some reactions could have happened during the elaboration process, and influenced the properties of PU film.

Specific investigations out of the scope of the thesis are clearly needed to clarify the link between composition and dielectric properties. Therefore, in following sections, investigations are conducted on only colorless PU samples.

4.2.2 Humidity

4.2.2.1 Dielectric properties at different humidities

Fig. 4.9 presents ε_r' of PU versus $E_{AC\text{-peak}}$ at different humidity levels.

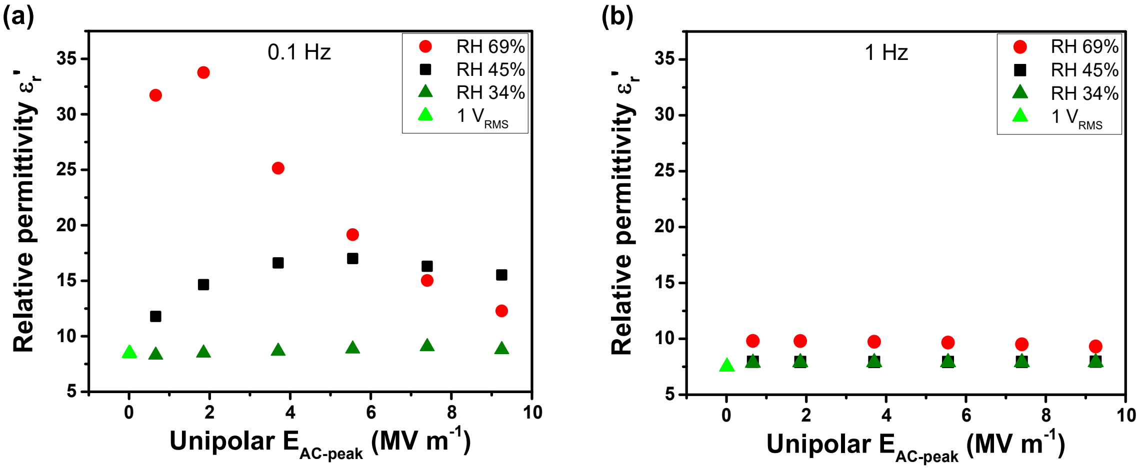

Fig. 4.9. Relative permittivity of PU versus electric field at different humidity: (a) at 0.1 Hz, (b) at 1 Hz.

At 0.1 Hz, the evolutions of ε_r' versus $E_{AC\text{-peak}}$ distinct among humidity levels, while at 1 Hz, only RH 69% leads to a slightly higher ε_r' than at other RH levels It is worthwhile to note again that at 1Hz, the permittivity values are electrical field independent. Therefore, existence of water molecule clearly contributes to the permittivity mainly to low-frequency procedures, i.e., MWS polarization, DC conduction and/or electrode polarization, but also to faster polarizations such as dipole polarizations.

The remarkable impact of humidity on the dielectric properties of PU versus $E_{AC\text{-peak}}$ is quite surprising. Indeed, an ether polyol is more resistant to hydrolysis than an ester polyol, and a MDI group has a weak tendency to hydrolyse compared to a TDI group [132]. This is one of the reasons why this polyurethane was chosen.

Fig. 4.10 presents the dielectric properties of PU at different levels of humidity and electric field versus time.

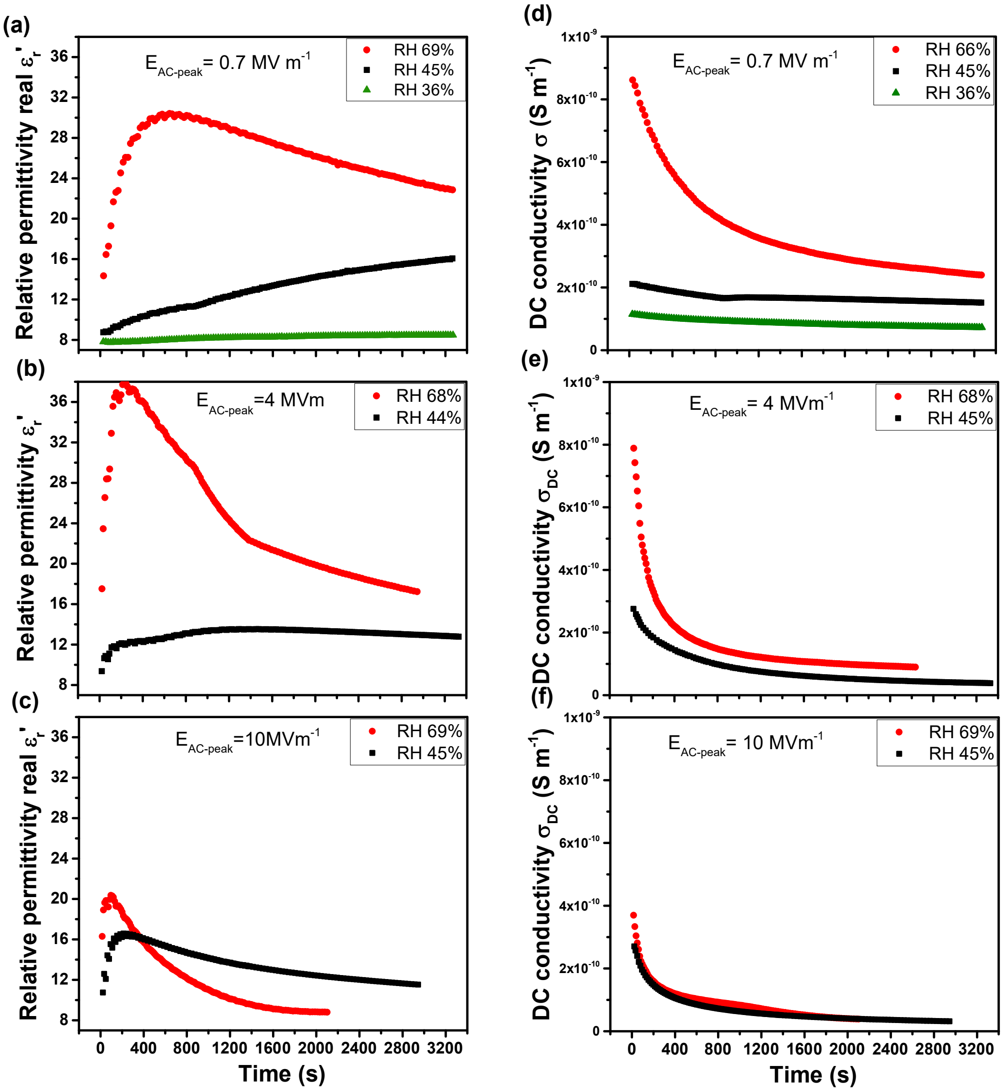

Fig. 4.10. Dielectric properties of PU versus measuring time at different levels of humidity and electric field at 0.1 Hz: (a), (b), (c) dielectric permittivity; (d), (e), (f) DC conductivity

At high humidity (RH> 66%), the maximum of ε_r' show higher values of 30 and 38 at 0.7 and 4 MV m^{-1}, and a relative lower value of 21 at 10 MV m$^{-1,}$ indicating that the maximum value of the permittivity also depends on the amplitude of the electrical field. At medium humidity (around RH 45%), the maximum of ε_r' are in a range of 14-18 for the three $E_{AC\text{-}peak}$. At low humidity (RH 34%), the single measurement performed at 0.7 MVm-1 shows that εr’ values keep unchanged around 8 (0.7 MV m^{-1}).

At RH> 66%, the evolutions of ε_r' versus time are similar under all $E_{AC\text{-}peak}$. ε_r' reach their maximum in a short time (less than 400 s), followed by a slow decrease. At RH around 45%, the evolutions of ε_r' vary with $E_{AC\text{-}peak}$. At 0.7 MV m^{-1}, ε_r' increases monotonically, at 4 MV m^{-1}, ε_r' increases and stays stable, while at 10 MV m^{-1}, ε_r' increases firstly, and then decreases.

Fig. 4.10 (d), (e) and (f) show that the values of DC conductivity increase with the humidity level. This increase is however large when the electrical field amplitude is small. Contrary to the experimental results in section 4.3.1.1, higher permittivity are in this section associated to higher level of conductivity.

For a given humidity and electric field, the DC conductivity σ_{DC} decreases versus time and probably reaches a steady state with very low values of conductivity (< 2.8 x 10^{-10} Sm^{-1}) . The higher the amplitude of electrical field is, the shorter the time needed to reach to the steady state is.

These experimental results clearly indicate that the maximum value of the permittivity, the DC conductivity as well as their evolution versus time vary under the conjugate effect of the humidity (RH) and the amplitude of the electric field ($E_{AC\text{-}peak}$). The effect of RH (especially high RH level) and $E_{AC\text{-}peak}$ is mainly observed at the transient behavior of PU, among which the most perceivable is the variation of the permittivity and the conductivity values.

In literature, the physical change caused by water is mostly due to the water absorption of the polymer matrix [49]. In the case of PU, the soft segments are more responsible for the sensitivity to humidity, considering their higher hydrophilicity than the hard segment ones [148,149]. The absorbed water could act as a plasticizer in PU because of the small size of water molecule. In the system containing water, the change of dielectric properties could be attributed to reorientation of water molecules, dipole relaxation as well as the DC conduction due to ions transportation[150]. Only a little quantity of absorbed water can contribute to the molecular mobility of the polymer, consequently enhance the MWS polarization and the α dipolar relaxation [149].

However, the impact of the electric field on dielectric properties of non-ferroelectric EAPs is rarely documented, not to mention the joint effect of the humidity and the electric field.

Yet no matter what the mechanism is, the humidity plays an important role. The polar nature of water contributes to the global polarization when bonded to the polymer chain. The high conductivity of water (5×10^{-5} sm^{-1} for deionized water at 25°C) increases the global DC conductivity of the polymer. It is worth noting that one cannot simply take the permittivity increased by water absorption as an improvement to the PU properties, since the field-induced polarization decreases continuously versus time.

4.2.2.2 Young's modulus at different humidities

Mechanical measurements were conducted on PU samples at different humidity levels. The PU samples were put in atmosphere with humidity of 41% and 70% separately for at least 1 hour. At least 3 samples were tested at each humidity. The average Young's modulus of PU was determined to be 28 MPa at RH 41% and 21 MPa at RH 70%, which correspond to a decrease of 25 %. This decrease is in agreement with the plasticizing effect of the water molecules [151–154].

4.2.3 Temperature dependence of dielectric properties

Fig. 4.11 describes the temperature dependence of PU dielectric properties at 1 V_{RMS}, 0.1 Hz, in a temperature range from -100 to 80 °C.

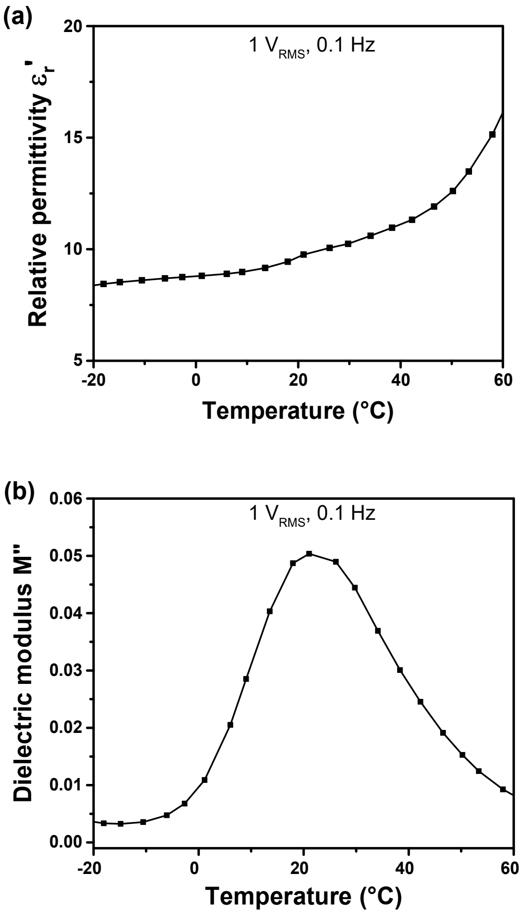

Fig. 4.11. Temperature dependency of dielectric properties of PU: (a) relative permittivity ε_r', (b) dielectric modulus M''

Fig. 4.11 depicted the variation of the permittivity and the M'' dielectric modulus versus temperature.

Since the electromechanical characterization of the polymer is performed at room temperature and at low frequency, one part of the observed dispersion on the measurements can also be explained by temperature fluctuations, which can induce a strong changes in the dielectric properties.

Dielectric measurements versus temperature, around the room temperature at high electrical field level will be probably necessary to better quantify the impact of the temperature variation on the actuation capability of the polymer.

4.3 A better prediction of the M_{31} coefficient with controlled factors

4.3.1 Case of the studied PU

The M_{31} value can be predicted by the law $\varepsilon_0\, \varepsilon_r'/2Y$, as shown in equation 1.16.

The aim of this section is to evidence that the accuracy of the prediction depends on the control of the experimental conditions in which the measurements are performed.

Fig. 4.12 presents the measured and calculated M_{31}coefficient obtained at high and medium humidities.

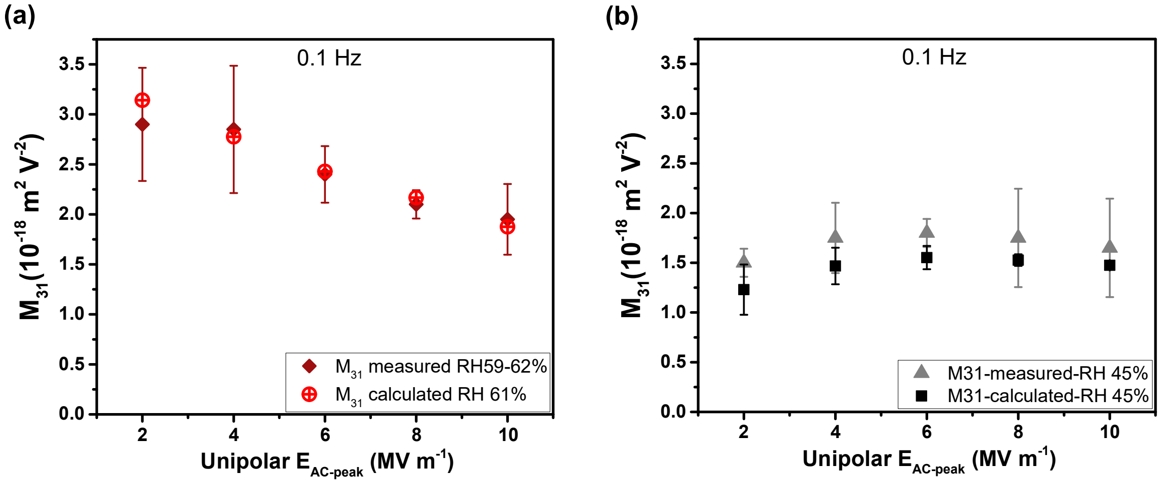

Fig. 4.12. M_{31} measured and calculated versus $E_{AC\text{-}peak}$ at 0.1 Hz, with time and humidity controlled: (a) high humidity around 60%, (b) medium humidity around 45%.

In the electric field range of 0.7 -10 MV m^{-1}, at both high humidity around RH60% and medium humidity around RH45%, the calculated M_{31} succeeds to predict closely the average value of the measured M_{31}. In addition, it achieved to predict the decreasing M_{31} versus $E_{AC\text{-}peak}$ at high humidity, and a relative stable M_{31} versus $E_{AC\text{-}peak}$ at medium humidity.

Moreover, with controlled experimental condition, the measured M_{31} are also less dispersed comparing with section 3.4. For example, at 10 MV m^{-1}, 1.6 x 10^{-18} m^2V^{-2} to 2.2 x 10^{-18} m^2V^{-2} was observed at RH around 60%, and 1.2 x 10^{-18} m^2V^{-2} to 2.2 x 10^{-18} m^2V^{-2} at RH 45%.

4.3.2 Case of two other PUs with different HS content

The M_{31} of three different PU namely PU60, PU75, PU87 respectively have been measured using the bender method and calculated with the experimental values of their permittivity and Young's modulus.

As mentioned in section 2.1, these three compositions differ by their HS/SS ratio. The HS content for PU60, PU75 and PU87 are 65%, 26% and 45% individually.

The dielectric permittivity as well as the M_{31} were measured in a RH range of 38%-42%. The permittivity was taken at the 24th cycle of each electric field application. For Bender measurement, an electric field was applied for 240s to reach the stationary state, then the measurement of M_{31} at each $E_{AC\text{-}peak}$ was carried out.

Fig. 4.13 presents the ε_r' evolution of the three PUs, as a function of $E_{AC\text{-}peak}$.

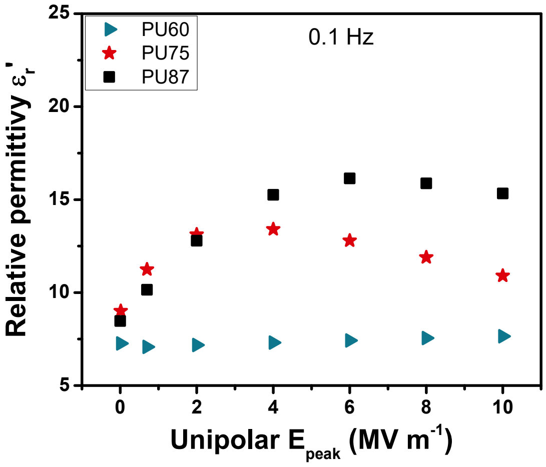

Fig. 4.13. Relative permittivity versus electric field: three PUs with different HS content, at humidity 38-42 %.

The behavior of ε_r' versus electric field is quite similar for PU75 and PU87, with a first increase followed by a slight or moderate decrease at $E_{AC\text{-}peak}$ ≥ 6 MV m^{-1}, though the values at higher $E_{AC\text{-}peak}$ are slightly different. These different values at higher $E_{AC\text{-}peak}$ could possibly be related to the dissimilar molecular weight of the polyol (2000 g mol^{-1} for PU75 and 1000 g mol^{-1} for PU87).

ε_r' of PU60 is stable with the electric field and exhibits a lower value than those of PU87 and PU75. Compared to the high hydrophilic SS content of PU75 and PU87 (74% and 55%), the low SS content of PU60 (35%) makes it less sensitive to humidity. It is reasonable to conclude that higher the HS content in PU, better the stability to the amplitude of electric field.

Fig. 4.14 depicts the measured and calculated M_{31} of PU75 and PU60 obtained at 0.1 Hz.

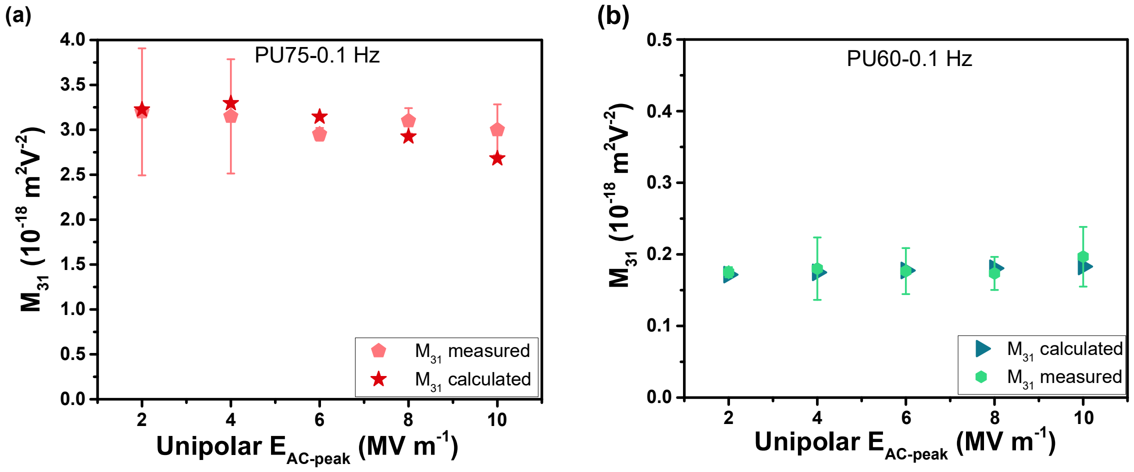

Fig. 4.14. M_{31} measured and calculated for different compositions of PU (a) PU 75, (b) PU 60.

The calculated M_{31} succeed to predict closely the measured M_{31}. The measured M_{31} of PU75 show a higher dispersion at 2 and 4 MV m^{-1}, which was already observed on PU87.

The M_{31} calculated at 1 V_{RMS} and the M_{31} calculated at same condition of M_{31} measured (10 MV m^{-1}, RH 45%) of the three Pus are compared in Fig. 4.15.

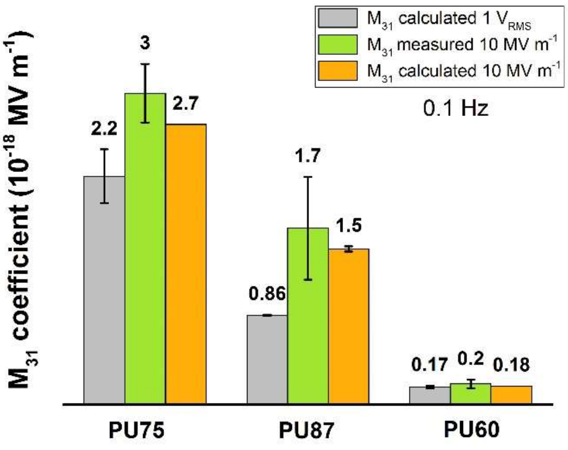

Fig. 4.15. The M_{31} measured, calculated at 10 MV m^{-1}, and M_{31} calculated at 1 V_{RMS} for three Pus (0.1 Hz)

It is revealed that for the three PU with different HS/SS contents, especially for PU87 and PU75 who have more SS contents, the M_{31} calculated at 1 V_{RMS} underestimates the measured

M_{31}. However, with similar electric field and humidity applied, the M_{31} calculated could predict closely the measured M_{31}.

4.4 Summary

PU exhibits higher relative permittivity at high electric field than at 1 V_{RMS}, which could explain the underestimation of M_{31} by the electrostatic model in chapter 3. At high electric field, the permittivity value is sensitive to several factors, including forms and strength of electric field, measuring period, elaboration process, humidity and temperature. This sensitivity explains the origin of the dispersion of measured M_{31} in chapter 3, and indicates the importance of measuring dielectric properties of EAPs at the same conditions to drive actuators.

The following points are important:

The elaboration process lead to films of different colors from colorless to pale yellow. The microstructure was found to be a little modified and this can explain the different behavior observed for dielectric and electromechanical performance. The elaboration process must be even more controlled in terms of temperature, mixing conditions and exposition to light, to limit the yellowing and the change in HS/SS organization that follows. The problem of unknown additives used by the industrial supplier can also play a role.

The permittivity value of PU is influenced by a joint effect of humidity and electric field. They can both accelerate the evolution of permittivity behavior in time scale. The water absorbed by PU can contributes to the global polarization. The plasticizing effect of water is confirmed by the decreased values of Young’s modulus.

For PU87, the permittivity measured at the same conditions with Bender measurement succeed to predict closely the measured electromechanical coefficient in both high and medium humidity. For the three PUs with different HS/SS content, though the humidity was roughly controlled, the permittivity measured at high electric field succeed to predict the measured M_{31}. Compared to ε_r’ measured at 1 V_{RMS}, the ε_r’ measured at high electric field predict M_{31} values nearer to the measured M_{31} for all the three PUs.

Further investigation on the dielectric properties under high electric field with varying temperatures should helpful to optimize the prediction of measured M_{31}.

Chapter 5. Effect of fillers on the properties of polyurethane composites and the possible origins of the limited improvement on M_{31} coefficient

Introducing conductive fillers into EAPs is considered as an effective method to improve the actuating performance, due to the enhancement of the permittivity that largely counterbalances the slight increase of the Young's modulus.

In many papers, the increase in permittivity is attributed to the interfacial polarization. The first objective of this chapter is then to conduct detailed studies in order to investigate this aspect.

In addition, in the literature, even if the permittivity is significantly increased, the electromechanical coefficient M_{31} or M_{33} are often less improved than expected. For example, in the previous studies of our laboratory on polyurethane/grafted carbon nanotubes composites, the permittivity was increased to 40 fold, while he M_{33} was increased only 3 times compared to neat PU[108].

Chapter 4 showed that in pure PU, with well controlled measuring conditions, the measured M_{31} coefficient could be successfully predicted by the ratio of the permittivity on the Young's modulus. This arises the question on the observed discrepancy for composites: is it due to poor control of the measurement conditions or are there any other reasons? It constitutes the second objective of the chapter.

To meet the two objectives, a deep investigation on the impacts of the OFG nanoplatelets on the mechanical and dielectric properties of PU/OFG composites is carried out in this chapter, with the help of multiscale characterizations.

5.1 Impact of humidity and electrical field amplitude on the properties of PU/OFG composites

5.1.1 Relative permittivity

Chapter 4 revealed the impact of humidity and of electrical field amplitude on the macroscopic properties of polyurethane film. The objective of this paragraph is to check whether humidity affects the properties of composites at the same level. Fig.5.1 presents the electric field dependence of PU and PU-10.25 wt%-OFG permittivity, at different humidity levels, at 0.1 Hz and 1Hz.

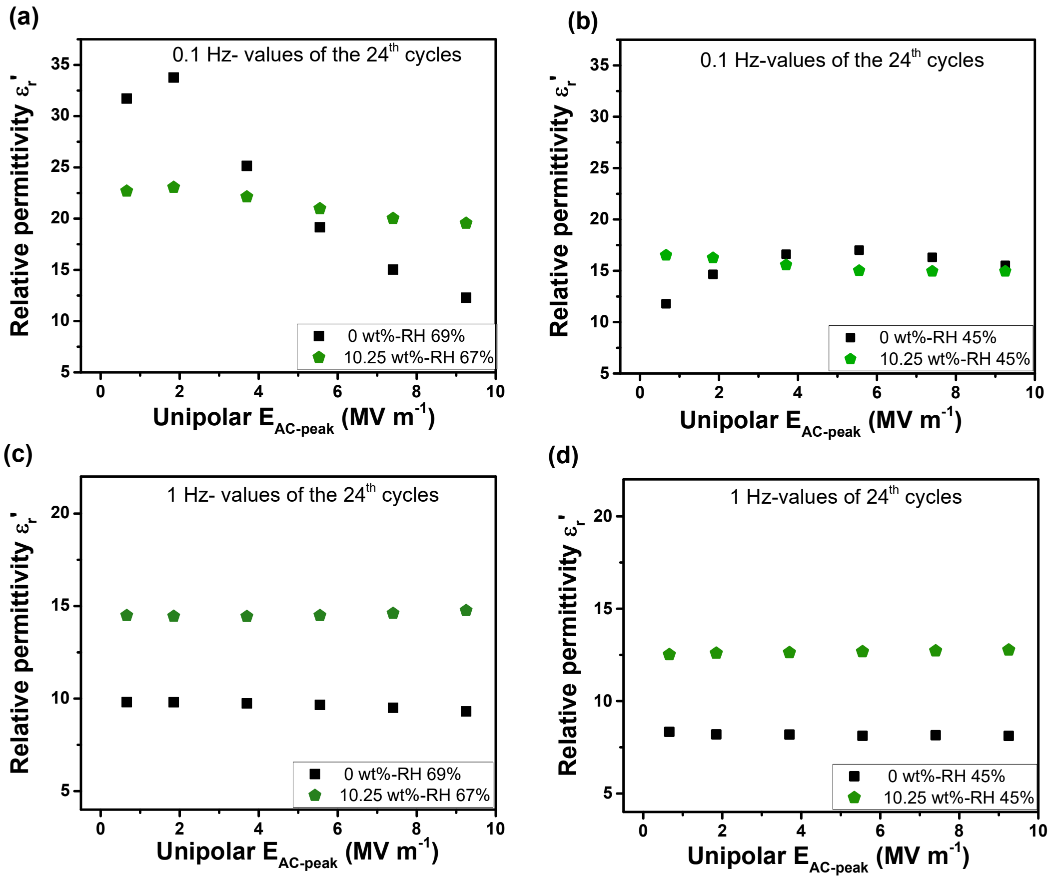

Fig. 5.1. The relative permittivity of PU and PU-10.25wt%-OFG at different humidity levels, 0.1 Hz: (a) high humidity, (b) medium humidity; 1 Hz: (c) high humidity, (d) medium humidity. Values of the 24thcycle presented for each $E_{Ac\text{-}peak}$.

At 0.1 Hz, for medium and high humidity level, contrary to what is observed on PU films, the permittivity of PU-10.25wt%-OFG is less affected by the electrical field amplitude and can be nearly considered as electrical field independent.

At 1 Hz, ε_r' values remain stable with the amplitude of $E_{AC\text{-}peak}$ for both PU and composite.

The humidity level slightly affects the permittivity values of the PU-10.25 wt%-OFG composite (around 22 for 67% and 16 for 45%) at 0,1 Hz as well as 1 Hz (around 15 for 67% of humidity and 12 and 45% of humidity). Similar to that mentioned in chapter 4 for pure PU, the presence of water molecule helps achieving a higher ε_r'. However, the effect of humidity is less pronounced in PU/OFG composites comparing with pure PU. This could be explained by the large aspect ratio and surface area of graphene nanoplatelets, which help reduce the water permeability of PU. It is reported that two-dimensional fillers with great aspect ratio, such as clay and graphene, are able to decrease the polymer permeability against gases and electrolytes by creating a natural barrier to the diffusion[155,156].

Fig.5.2 shows the electric field dependence of the permittivity for PU and PU/OFG composites, at medium humidity level (43%-47%), at 0.1 Hz and 1Hz.

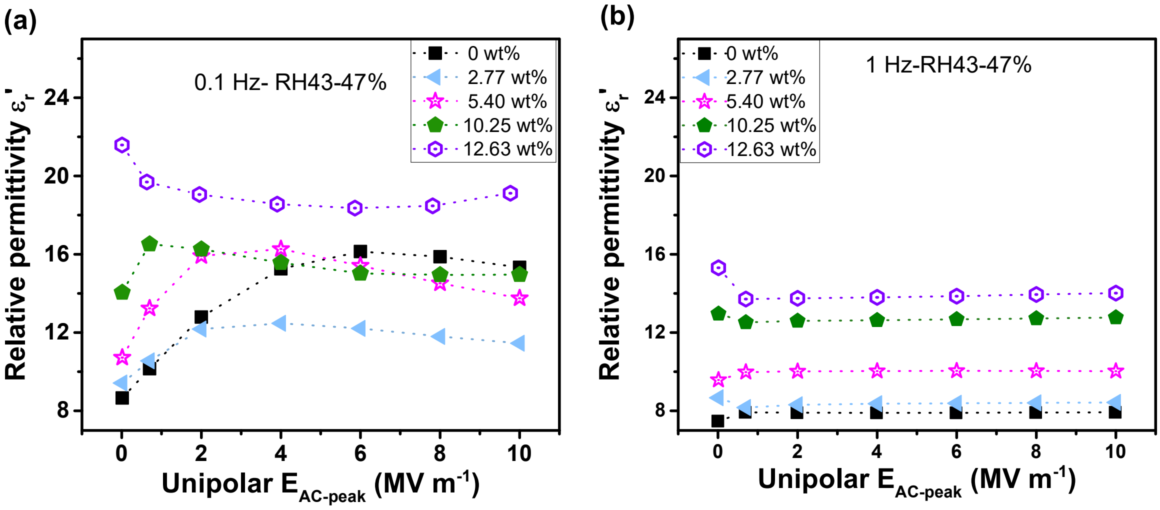

Fig. 5.2. Evolution of the permittivity of PU and PU/OFG composites versus electric field at RH 43%-47%: (a) 0.1 Hz, (b) 1 Hz (lines for guiding eyes).

At 0.1 Hz, with medium OFG content in PU matrix (2.77 wt% and 5.40 wt%), the evolution of ε_r' as a function of $E_{AC\text{-}peak}$ shows firstly an increase followed by a decrease. This evolution is in the same manner as for pure PU, though the variation is smaller (e.g., for PU-2.77 wt%-OFG, ε_r' varies between 10 and 12, while for pure PU, ε_r' varies between 10 and 16). With high OFG content, (10.25 wt% and 12.63 wt%), ε_r' shows a negligible decrease versus $E_{AC\text{-}peak}$. At 1 Hz, ε_r' values remain stable with the amplitude of $E_{AC\text{-}peak}$ for PU/OFG composites whatever the composition.

With the increase of OFG content, the permittivity of PU/OFG composites increases at both 0.1 Hz and 1 Hz, and the increased value is greater at 0.1 Hz. This gives a first evidence of the contribution of OFG nanoplatelets on low-frequency phenomena (MWS polarization and/or DC conduction). Detailed study would be presented in next sections.

It is worth noting that over the electric field range 0.7 -10 MVm^{-1}, contrary to usually believed, there is no systematic increase in ε_r' value of the composites comparing to pure PU. The improvement, less important than one expected, might explain some of the discrepancy between the calculated and the experimental M_{33} values in the previous work[108], since ε_r' were measured at 1 V_{RMS}.

5.1.2 Young's modulus

Mechanical measurements were conducted on PU-10.25 wt%-OFG samples with and without electric field application. Same as the case of PU, the Young's modulus of PU-10.25 wt%-OFG is independent to electric field.

Mechanical measurements were also conducted on PU-10.25 wt%-OFG samples at different humidity levels. The samples were put in atmosphere with humidity of 44% and 70% separately for at least 1 hour. At least 3 samples were tested at each humidity. The average Young's modulus of PU-10.25 wt%-OFG was determined to be 48 MPa at RH 44% and 45 MPa at RH 70%, which correspond to a decrease of 5 %. This decrease is much less than the 25% of PU (mentioned in 4.2.2.2), which is consistent with a reduced permeability of the polymer caused by OFG.From the application perspective, the most important conclusion of this paragraph is that the nano fillers show a beneficial effect on stabilizing the permittivity and Young's modulus values versus the field amplitude and the humidity level. This will also facilitate the characterization of the composite films for the next section, which is devoted to a better understanding of the role of the nanoplatelets.

5.2 Effect of OFG nanoplatelets on the properties of polyurethane composites

5.2.1 Microstructure of PU and PU/OFG composites

This paragraph deals with the nanofillers dispersion within the polymeric matrix and its interaction with the polymer chains with the help of SEM imaging and the influence of the nanofillers on the microstructure by using DSC techniques.

5.2.1.1 Cross-section morphology

Fig. 5.3 presents a few examples of SEM analysis on pure PU and composites containing respectively 5.40 wt%, 10.25 wt% and 13.13 wt% of OFG.

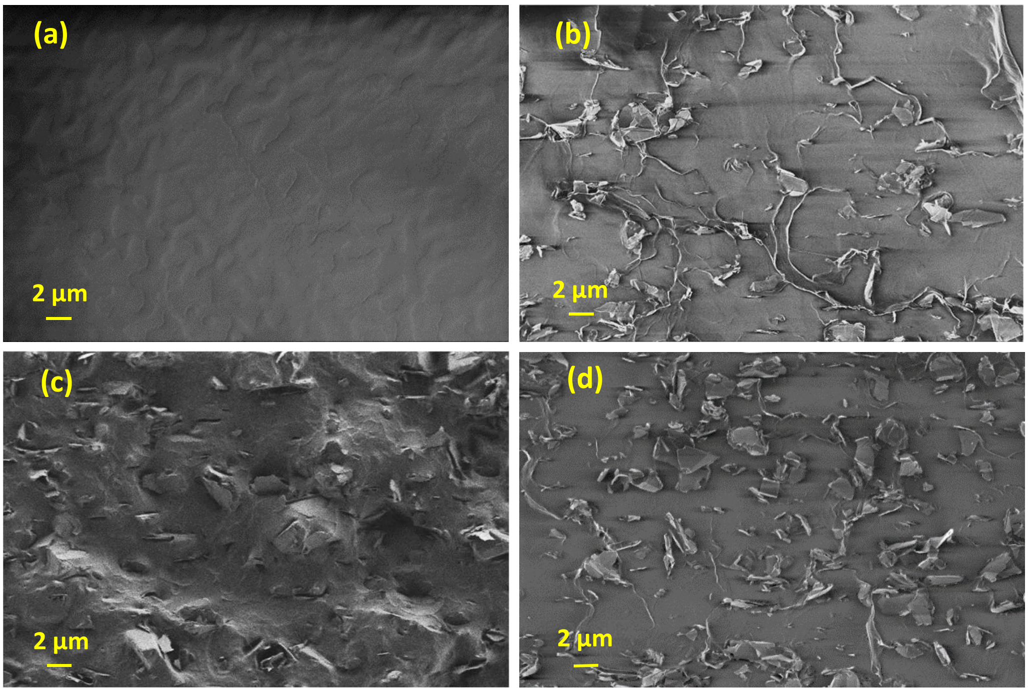

Fig. 5.3. SEM micrographs of a cryofractured cross section surface of the (a) pure PU, (b) 5.40 wt%-OFG, (c) 10.25 wt%-OFG and (d) 13.13 wt%-OFG.

According to Fig. 5.3, the OFG nanoplatelets are overall uniformly distributed in the PU matrix for all composite contents. For PU-13.13 wt%-OFG composite, the distance among the nanoplatelets is short in some region because of the high concentration. This might lead to electrical breakdowns under high electrical fields. For all composites, there is no sign of a preferential orientation of the nanoplatelets: they exhibit various orientations and positions (platelets in and perpendicular to the plane), indicating a three-dimensional (3D) distribution in the PU matrix.

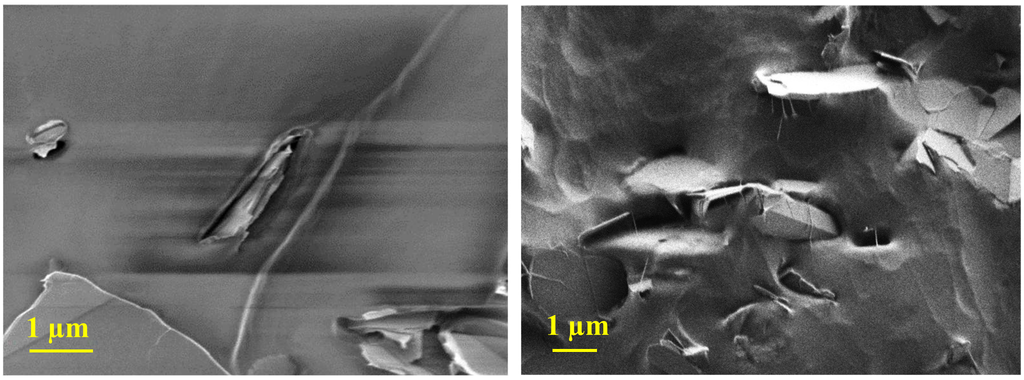

Fig. 5.4. SEM micrographs of a cryofractured (cross section) surface of the PU-10.25 wt%-OFG.

Fig. 5.4(a) displays a stack of a few OFG nanoplatelets (about 200 nm in thickness). The cohesion between the stacked platelets and the polymer appears to be imperfect since the cryofracture created a gap between them. In addition, Fig. 5.4(b) confirms this observation by highlighting only a few links between the OFG nanoplatelets and the PU matrix. The interfacial cohesion is therefore incomplete.

The distribution of planar size (l) and thickness (d) of the OFG nanoplatelets were observed from the SEM analysis, and presented in Fig. 5.5.

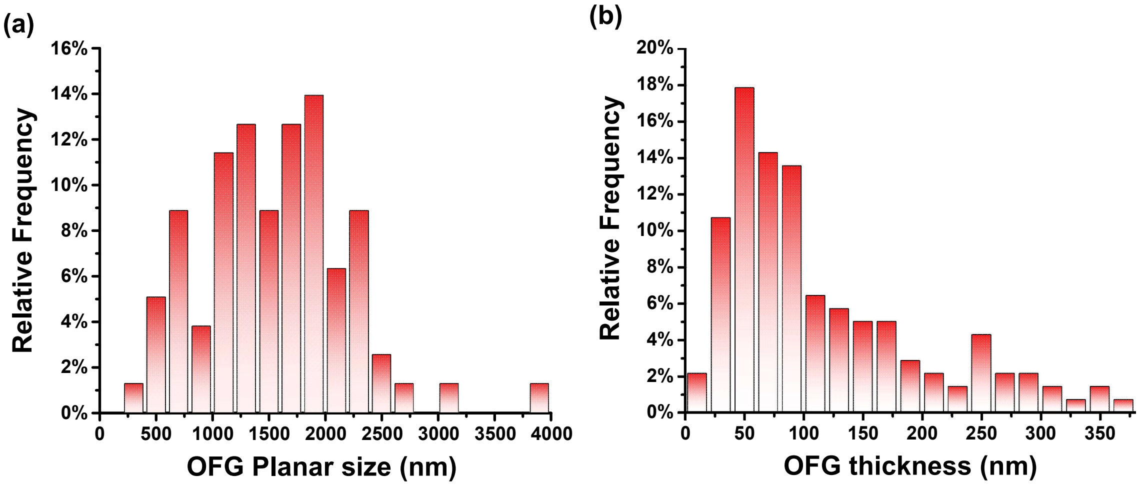

Fig. 5.5. Size determination of OFG nanoplatelets

The average values were determined as follow.

$$I = \frac{\sum N_i I_i}{\sum N_i} \tag{5.1}$$

$$d = \frac{\sum N_j d_j}{\sum N_j} \tag{5.2}$$

An average planar size of 1560 ± 640 nm and an average thickness of 115± 83 nm are obtained from respectively 80 and 150 measurements. The planar size is in the range given by the supplier, while the thickness is greater than 50 nm, in agreement with the observed stacked platelets. The mean aspect ratio (A_f= l/d) is calculated to be 14.

5.2.1.2 Thermal properties

Fig. 5.6 depicts the DSC thermograms of PU and a PU/OFG composites. The thermal properties are given in Table 5.1.

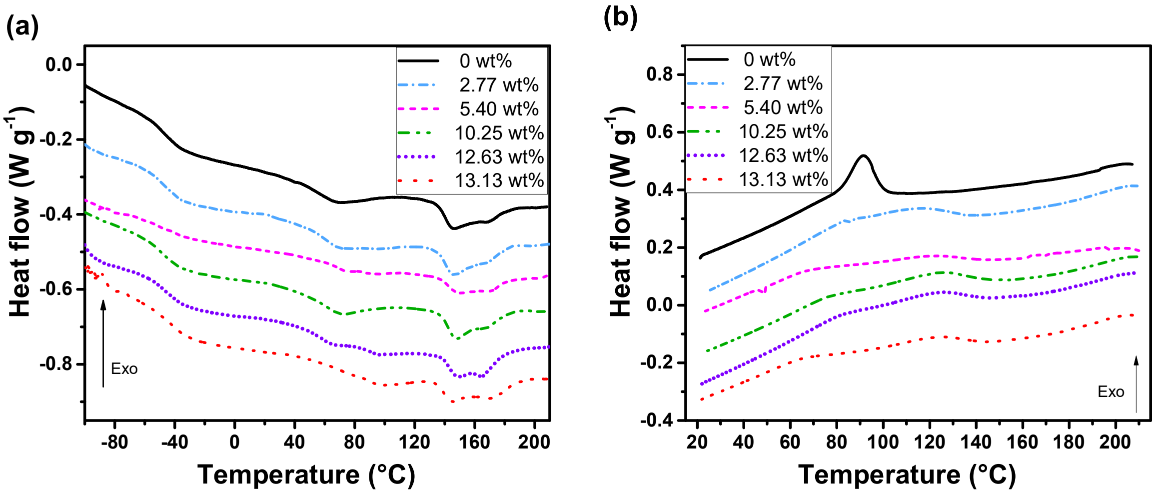

Fig. 5.6. DSC thermograms of PU and PU-OFG composites (a): heating process; (b) cooling process (position shifted for a better observation).

Table. 5.1. Thermal properties of PU-OFG films from DSC experiments.

wt% OFG	Tg_{SS} (°C)	ΔCp (mW)	T_{m1-2} (°C)	ΔH_f (J/g)	T_c (°C)
0	-46.1	1.2	147-169	12.8	90
2.77	-45.2	1.3	147-169	13.1	85-115
5.40	-48.9	1.3	150-168	11.6	85-130
10.25	-47.5	1.1	147-170	12.6	80-125
12.63	-45.8	1.2	150-169	11.2	75-125
13.13	-41.1	1.1	147-173	11.2	70-130

Four main thermal events could provide information on the microstructure of the composites. Globally, the Tg values do not vary considerably with the OFG content: only a moderate increase was noted at high contents. This increase could be an indication of a higher quantity of HS dissolved in the soft domains, therefore a higher degree of HS-SS mixing.

The endotherm in the range 40-80°C can be associated to local restructuring of hard segment units within the hard microdomains including disruption of short-range order or disruption of SS/HS bonds[144]. It is neither affected by the presence of OFG even if a slight modification is observed with OFG contents of 12.63 wt% and 13.13 wt%.

According to the bimodal endotherm (T_{m1} and T_{m2}) in the range 130-180°C, the crystallinity could be considered unchanged regardless of the OFG content. The both interpretations in 4.2.1.3 relate the increasing crystallinity to increased T_{m1}, T_{m2} and the global melting enthalpy ΔH_f, whereas no significant change was observed in T_{m1}, T_{m2} nor ΔH_f with the incorporation of OFG.

A more important influence of the OFG can be seen upon cooling. The crystallization phenomenon is more widespread and the Tc temperature is higher. The nanoplatelets seem to play the role of nucleating agents facilitating the crystallization.

In conclusion, only a slight modification by OFG on the microstructure of PU/OFG composites is observed from the DSC analysis. Nevertheless, the experimental results can neither definitely rule out the effect of the microstructure on the properties. Indeed very small differences at the micro level could have an impact in macroscopic dielectric and electromechanical properties.

5.2.2 Mechanical properties

As the M_{31} depends on the Young's modulus of the polymeric films, this paragraph is devoted to the study of the mechanical reinforcement induced by the nanofillers.

5.2.2.1 Experimental values

A quasi anhysteretic behavior is observed in the strain-stress curve, evidencing that the mechanical losses are negligible. From this curve, the Young modulus are determined in accordance with the method presented in chapter 2.

Fig. 5.7 presents the experimental Young's modulus versus OFG content. The experimental values increased linearly with the introduction of OFG in a moderate extent. For example, an increase of 30 % was obtained with 10.25 wt% OFG loading.

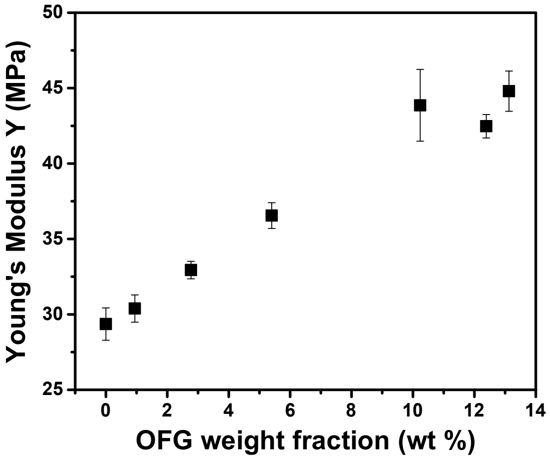

Fig. 5.7. Measured Young's modulus of PU/OFG composites versus OFG content at a speed of 0.1 % s^{-1}

5.2.2.2 Experimental and modeled Young's modulus

Mechanisms of reinforcement are strongly influenced by the dispersion morphology and then the aspect ratio of the nanofillers. Several composite models can be used to predict the mechanical properties. They generally differ by the nature of the dispersion and the morphology of the fillers.

The rule of mixtures is a classic law to predict the properties of mixtures [157], according to which the Young's modulus of composites could be written as (5.3):

$$Y = Y_f \emptyset_f + Y_m(1 - \emptyset_f) \tag{5.3}$$

Y, Y_f and Y_m are the Young's modulus of the composites, the fillers and the matrix and Φ_f the volume fraction of fillers. This law was not chosen since the geometry factor of the fillers is not considered. In addition, this law is adapted to composites with aligned fibers[158] .

Another category of models is Guth and Guth-Gold models [159] based on the viscoelastic theory and often used to predict mechanical behavior of composites [6,7]. They consider the volume fraction but not the Young's modulus of fillers. Only when the amount of fillers is higher than 10 % in volume, the geometry factor of fillers is considered.

The Halpin-Tsai model [160] can also be considered. It is based on the self-consist micromechanics model by Hill[161], for sphere filled composites. In Hill's model the composite is assumed to be homogeneous everywhere, and the interface adhesion is perfect for stress transform. Halpin-Tsai developed this model for aligned fibers, taps and planers, taking into account the geometry factor of fillers. It is later modified to Halpin-Kardos model[160] for randomly distributed fillers. Halpin-Tsai and Halpin-Kardos models have succeeded in predicting composites filled with nanoflakes [162–164].

Due to the nature of the OFG fillers (nanoplatelets) and its random dispersion, the Halpin-Kardos model was chosen to predict the Young's modulus according to (5.4):

$$\frac{Y}{Y_m} = \frac{3}{8}\frac{(1+2A_f\mu_L\phi_f)}{(1-\mu_L\phi_f)} + \frac{5}{8}\frac{(1+2\mu_T\phi_f)}{(1-\mu_T\phi_f)} \tag{5.4}$$

where Y and Y_m are the Young's modulus of respectively the composites and the matrix, Φ_f is the volume fraction of fillers, which was calculated assuming a density of 2.2 g cm^{-3} for OFG and 1.13 g cm^{-3} for PU. A_f is the aspect ratio, whose average value was determined to be 14 earlier in this work, and μ_L and μ_T are geometry factors, according to (5.5) and (5.6).

$$\mu_L = \frac{Y_f/Y_m - 1}{Y_f/Y_m + 2A_f} \tag{5.5}$$

$$\mu_T = \frac{Y_f/Y_m - 1}{Y_f/Y_m + 2} \tag{5.6}$$

Here, Y_f is the Young's modulus of the fillers. This model assumes that a perfect adhesion between polymer and filler.

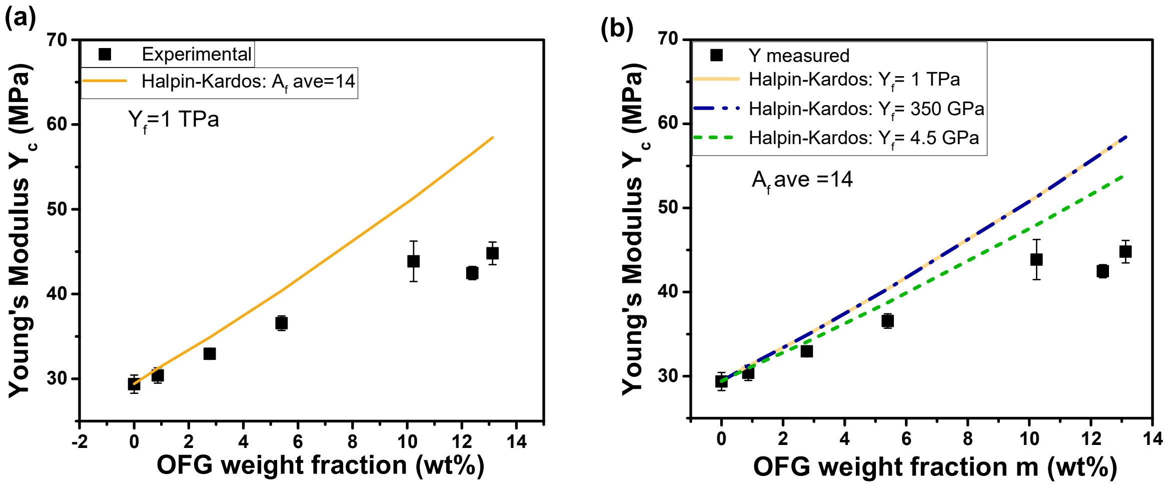

Fig. 5.8. Young's modulus of PU/OFG composites (without Au electrode) measured and predicted by Halpin-Kardos model (a) with Y_f=1 TPa, (b) with different Y_f.

Fig. 5.8(a) presents the fitting of the experiment values by Halpin-Kardos model, using the aspect ratio determined in 3.1.3 (A_f =14), the measured modulus of PU matrix (Y_m= 29 MPa) and the published value of 1 TPa for a monolayer of graphene [165–167].The predicted values were closed to the experimental ones. However, the experimental values were slightly smaller than the predicted ones at high OFG concentration. This might be due to the fact that the Y_f of monolayer graphene was used above, while according to Fig. 3(a), the OFG nanoplatelets agglomerate in the PU matrix.

There is an uncertainty regarding the Y_f due to the fact that the Young's modulus usually decreases with the number of graphene layers due to the slippage between the layers [168]. Two additional values were then tested for the model: 350 GPa as published for a 10-layer graphene sample [169] and 4.5 GPa corresponding to the Young's modulus of graphite [170]. The new fittings are presented in Fig. 5.8(b).

Among the possible physical values for Y_f, the best fit is obtained for the lowest value of 4.5 GPa. This result as well as the remaining difference between experimental and theoretical values can be explained by the moderate interfacial adhesion between the polymer and the nanoplatelets, in good agreement with the SEM micrographs. This effect is actually not considered by the model.

For the composites, the use of fillers has led to moderate variations of the Young's modulus versus content confirming the moderate adhesion between the fillers and the polymeric matrix observed by SEM imaging. The moderate mechanical reinforcement is a benefit for electromechanical performance, since the M_{31} coefficient follows a law proportional to 1/Y.

5.2.3 Dielectric properties at room temperature

This paragraph focuses on the permittivity, loss tangent and conductivity measurements versus fillers contents.

5.2.3.1 Relative permittivity

Fig. 5.9(a) presents the evolution of the real part of the dielectric constant (ε_r') for different OFG weight fractions (m) as a function of the frequency for PU films and PU-OFG nanocomposites.

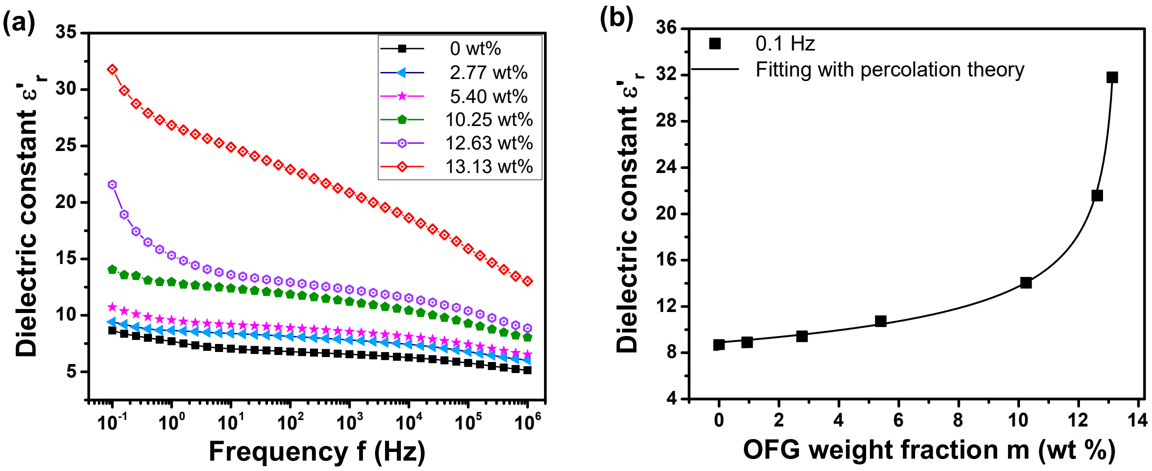

Fig. 5.9. Variation of the real part of the dielectric constant ε_r' versus (a) frequency and (b) OFG weight fraction.

The dielectric constant decreases when the frequency increases for both the PU film and the PU/OFG composites. Two slope changes are observed: the first one occurs at the lowest frequencies and is usually attributed in the literature to different phenomena such as DC conduction, Maxwell Wagner Sillars (MWS) polarization and/or electrode polarization[92,93,102]; and the second one, less pronounced, around 10^4 Hz, generally attributed to dipolar relaxation.

Fig. 5.9(b) presents the variation of the dielectric constant versus OFG content, at 0.1 Hz. The dielectric constant increases with the OFG content and this occurs to a greater extent after 10.25%. The attained value of the dielectric constant is about four times higher than that of the PU film.

Below the percolation threshold, the experimental data can be modeled by[171]:

$$\varepsilon_r' = \varepsilon_{rm}'\left(1 - \frac{m}{m_c}\right)^{-q} \tag{5.7}$$

Here, ε'_{rm} is the dielectric constant of the polymer matrix, m_c is the percolation threshold, and q is the critical exponent.

At 0.1 Hz, a percolation threshold of 13.34 wt% and a q exponent of 0.32 are obtained. This calculated percolation threshold is supported by the SEM images which shows a large proximity between fillers for contents around 13 wt%.

According to the literature, typical values for the q exponent are 1, 1.3 and 0.7 for 1D, 2D and 3D space dimensions[171–174], respectively. q values below 0.5 have also been reported and attributed to a 3D network of fillers [175]. The q value of 0.32 obtained in this work can be related to a 3D distribution of OFG nanoplatelets, also in good agreement with the SEM images.

5.2.3.2 Loss tangent

Figure 5.10 depicts the variation of the loss tangent (ratio of the imaginary part ε_r'' to the real part ε_r' of the dielectric constant) versus frequency for various OFG contents.

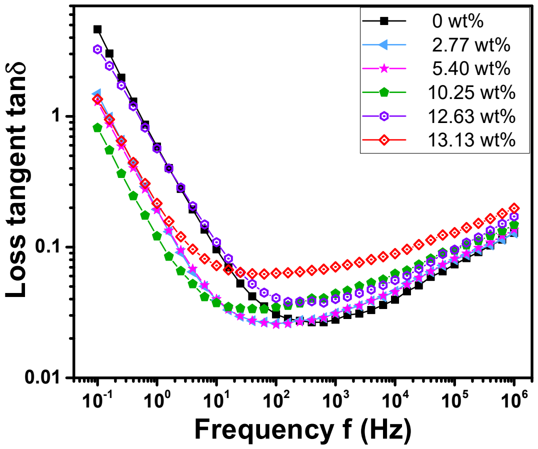

Fig. 5.10. Loss tangent of various PU/OFG composites versus frequency

As for the pure PU films, as the frequency increases, the nanocomposites exhibit a large decrease in loss tangent followed by a moderate increase. The decrease observed for low frequencies is linked to the end of the contribution of electrode polarization, MSW polarization and/or conduction to the dielectric properties whereas the increase at medium frequencies is due to other dipolar relaxations. For frequencies below 10 Hz, lower loss tangent values are obtained for composites with 2.77, 5.40 and 10.25 wt% OFG as compared to pure PU.

Generally, conductive fillers increase the loss tangent of the composites [99,101,102]. Only very few papers have reported on lower dielectric losses with conductive fillers [176]. This decrease could certainly be associated to the functionalization of graphene. The insulating layer formed by the plasma functionalization may have played an effective role since the oxygen functionalization created carbonyl, hydroxyl and other functionalities on the surface of the conductive platelets.

5.2.3.3 Conductivity

Fig. 5.11(a) presents the real part of the conductivity (σ’) of PU and PU/OFG composites as a function of the angular frequency (ω). The curve of conductivity of both PU and PU/OFG composites consist of two parts, namely, a low-frequency plateau, followed by a monotonously increasing part at higher frequency. In this higher frequency range, the conductivity increases when raising the OFG content, which is consistent with higher conduction values of the graphene fillers. For concentrations beyond 14.60%, the global conductivity exhibits a sharp increase in accordance with a percolating system.

The percolating threshold, corresponding to a sudden jump in the plateau values is probably reached for a value between 13.13 wt% wt and 14.60 wt%, in good agreement with the calculated percolation threshold of 13.34 wt% from the permittivity measurement.

According to Jonscher’s law[71], the conductivity σ’ can be described as:

$$\sigma' = \sigma_{DC} + A\omega^{n} \tag{5.8}$$

where A is a constant and n is the power exponent.

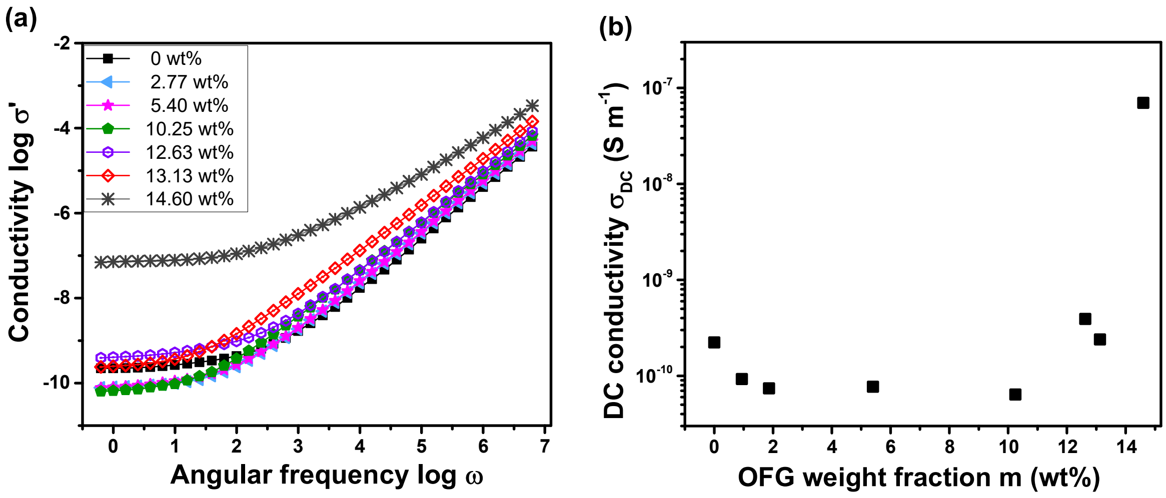

Fig. 5.11. (a) Conductivity of PU/OFG composites versus frequency, (b) DC conductivity versus OFG weight fraction.

The DC conductivity σ_{DC} corresponds to the value measured for the plateau. The n exponent was obtained using the slope of the curve representing log ($\sigma' - \sigma_{DC}$) as a function of log ω (data not shown). The n exponent is in the range 1 to 1.1, except for 14.60 wt% with n near 0.8. Despite that the exponent is limited to $n \leq 1$ in the original Jonscher's law, reports on n values higher than unity exist in polymers with ionic-like conduction mechanisms [72,73]. For a higher OFG content near the percolation threshold, the n exponent value diminishes which can indicate the contribution of electronic hopping conduction.

Fig. 5.11(b) depicts the evolution of σ_{DC} versus the OFG content. The observed trend is similar to that obtained for the loss tangent: an initial decrease for low and moderate OFG contents followed by an increase for higher contents in the vicinity of the percolation threshold. The evolution is therefore quite different from what has been described in several papers on EAP composites with carbon fillers [102,177], which reported a monotonic increase of DC conductivity when increasing the content of conductive fillers. Since σ_{DC} is related to the transport of free charges from one electrode to another, it can be assumed that the OFG would behave as traps for the charged mobile species with an efficiency correlated to the distance between them. For a moderate OFG content, the distance between two neighboring traps is high enough to disturb the charge transport but this capability decreases as the distance is reduced, thus leading to new paths for the charge displacement. Near the percolation threshold, an electronic conduction can have an important role.

While the variation in permittivity of composites as a function of the OFG content follows a classical behavior, the loss tangent and the DC conductivity exhibit a less documented behavior, which can be related to the capability of functionalized nanoplatelets to behave as charge traps.

5.2.3.4 Dielectric modulus M''

As it has been reported in Chapter 1 dedicated to the state of art, at a given temperature and in a given frequency range, dipoles created by various mechanisms within the material can contribute or not to the global polarization, depending on their relaxation state. In addition, the charge carriers present in the material can also affect the polarization values, its direction and its stability.

Fig. 5.12 presents the imaginary part of relative permittivity ε_r'' and the dielectric modulus M'' of PU and PU/OFG composites in the frequency range 0.1 Hz-1 MHz.

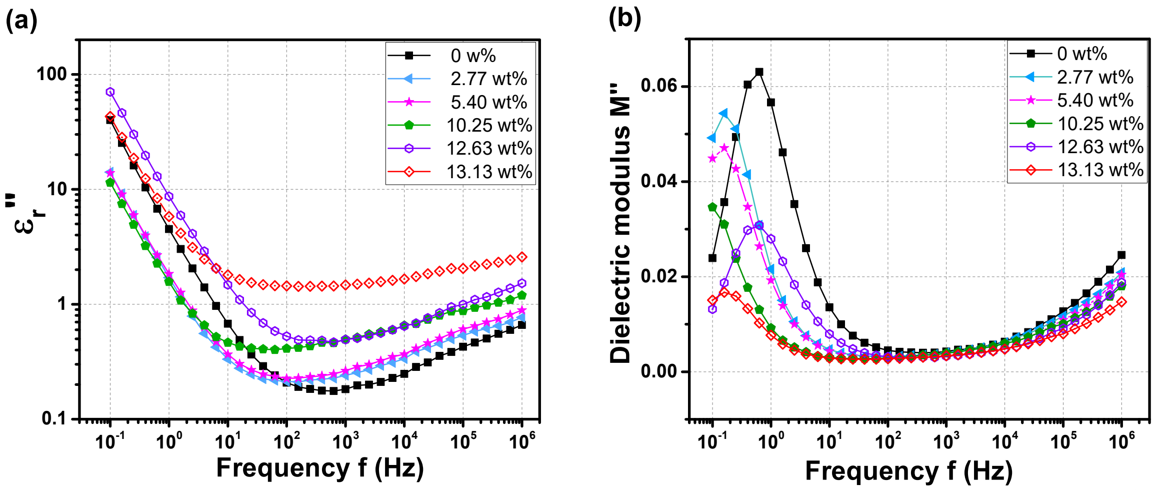

Fig. 5.12. (a) Imaginary part of permittivity εr", (b) Dielectric modulus M" of PU and PU/OFG composites versus frequency.

Comparing to ε_r", M" succeeds to highlight the dielectric phenomena at low frequency. The first peak of M" at low frequency can indicate the contribution of MWS interfacial relaxation, the incomplete peak at high frequency may be attributed to dipolar relaxations.

Temperature-dependent experiments were conducted for a more thorough understanding of their effect on the permittivity.

5.2.4 Dielectric and conduction properties versus temperature and frequency

5.2.4.1 Dielectric relaxations in wide temperature range at 0.1 Hz

Fig. 5.13 presents the evolution of the imaginary part of the dielectric constant ε_r" and the dielectric modulus M" in the temperature range from -100 to 80 °C at 0.1 Hz.

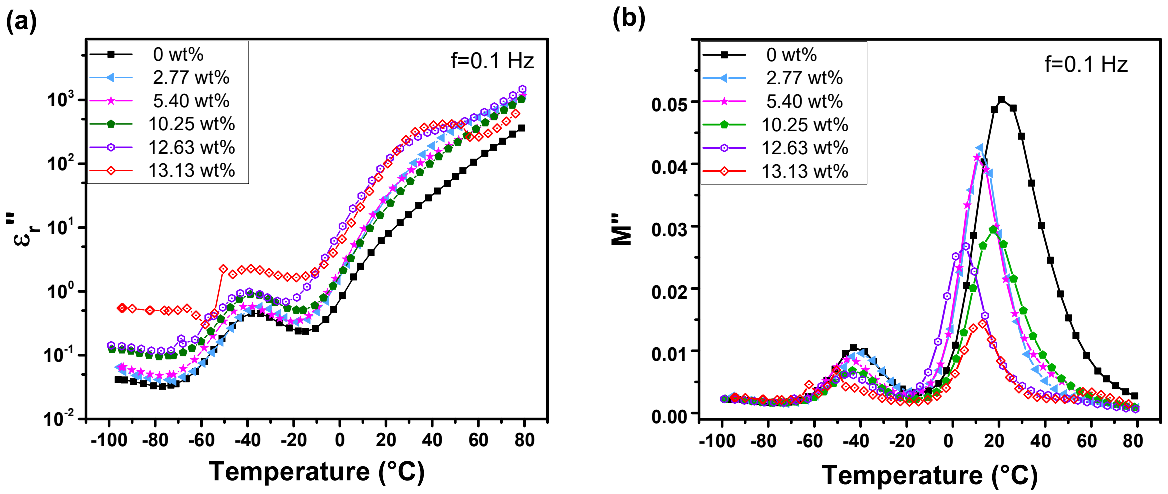

Fig. 5.13. Dielectric relaxations of PU/OFG composites at 0.1 Hz (a) imaginary part of the permittivity εr", (b) imaginary part of the dielectric modulus M".

Two maxima of M” are clearly observed for the PU and the PU/OFG composites. Another peak of lower intensity is also present near -90 °C, assigned to the β-relaxation caused by the local motion of polar groups on the polymer chain. This relaxation is not really affected by the OFG nanoplatelets. The second peak around -50/-40 °C is related to the α-relaxation with the segmental motion of the soft phase. The polymer goes from a rubbery to a glassy state.

5.2.4.2 Dipolar relaxations

No detailed analysis on the β relaxation was conducted, since no great change was observed between PU and PU-OFG composites over the corresponding temperature range, and the intensity of the relaxation was too low for a precise analysis.

α relaxation provides information on the reorientation of the polar soft segments of the chain during the glass transition of the soft rich microphase.

Fig.5.14 depicts the parameters obtained from Haviliak-Negami fitting on α relaxation.

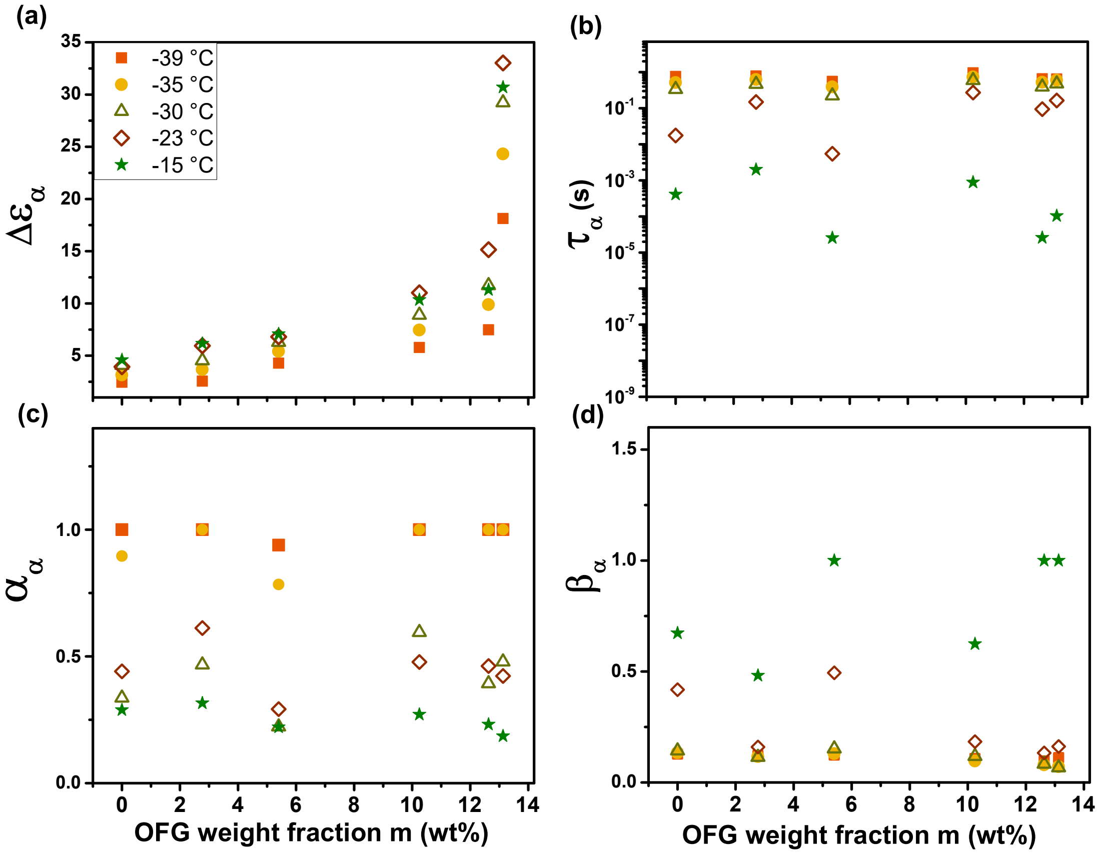

Fig. 5.14. Havriliak-Negami fitting parameters versus OFG content for α relaxation: (a) dielectric dispersion $\Delta\varepsilon_\alpha$, (b) relaxation time τ_α, (c) (d) asymmetric parameter α_α and broadness parameter β_α.

The dielectric strength of α relaxation $\Delta\varepsilon_\alpha$ increases continuously with OFG content, and highlights a large increase near the percolation threshold. The relaxation strength is a measure of the number and the orientation correlations of dipole moments along the polymer chain[178]. Considering that the microphase separation is not greatly changed by OFG, it can be suspected that the OFG nanoplatelets affect the orientation correlation, following a mechanism that could be close to a graft effect of the OFG on the backbone. Lower scale characterizations could be useful for a better understanding. The variation of $\Delta\varepsilon_\alpha$ versus temperature is more important for composites with high OFG contents.

For the lowest temperatures (-39°C, -35°C and -30°C), the relaxation time τ_α could almost be considered constant versus OFG content; for the highest temperature (-23°C and -15°C), fluctuation of τ_α is observed among the composites.

At given temperatures, the shape parameter α is almost constant versus OFG content. With temperature decreasing to near T_g, the α value gets close to 1, indicating a more symmetric shape of the relaxation peak. The parameter β decreases as the temperature diminishes. As the temperature gets close to T_g, the value becomes independent on OFG content (about 0.3).

Fig. 5.15 presents the relaxation time τ_α of the composites as a function of 1/T.

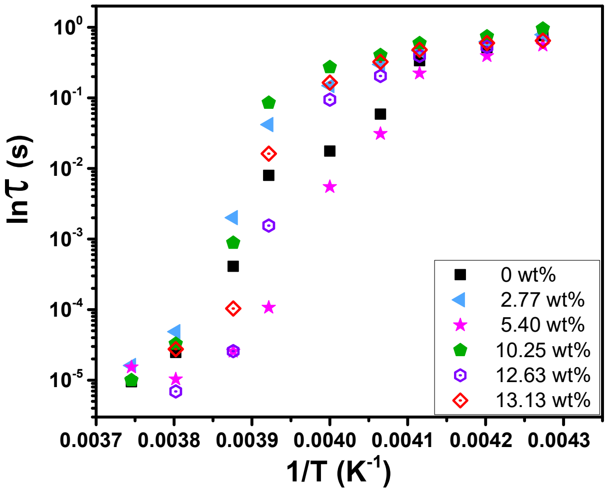

Fig.5.15. Temperature dependence of the α relaxation times, following the VTF law

τ_α changes by many orders of magnitude over the temperature range. The temperature dependence of the relaxation times is described by Vogel-Tammann-Fulcher (VTF) equation (equation 1.11). There is no significant change in the activation parameter B, the pseudo activation energy vary between 0.2 and 0.4 eV for PU and PU/OFG composites.

The third peak observed in M" formalism (Fig. 5.12(b)) is highly dependent on OFG content, with the position of the maximum varying from 0 to 25 °C. A mix of interfacial polarization (MWS), conduction and/or electrode polarization is associated to this range. To go deeper in the interpretation and obtain information on the type of charges involved in this process, two studies were conducted: the variation of DC conductivity with temperature, and the treatment of the relaxation phenomena in the range from -10°C to 35°C after subtracting the σ_{DC} part.

5.2.4.3 DC conduction

Fig. 5.14(a) presents the evolution of the log of σ_{DC} versus 1/T. In the temperature range -10 °C to 35 °C, log σ_{DC} exhibits a near linear relation with 1/T. The temperature range was chosen so as not to consider other phenomena such as α relaxation. The linear evolution agrees with the Arrhenius law [179]:

$$log\sigma_{DC}(T) = log\sigma_0 - \frac{E_a}{K_BT} \tag{5.9}$$

where σ_0 is the pre-exponential factor, E_a is the activation energy of DC conduction, and K_B is the Boltzmann constant.

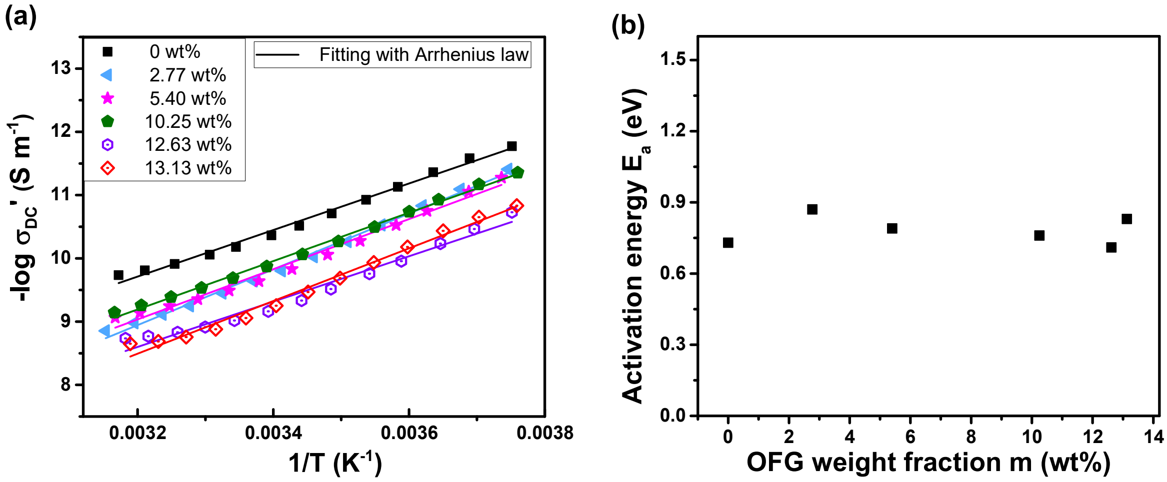

Fig. 5.14. Evolution of the DC conductivity of PU and the PU/OFG composites: (a) log σ_{DC} versus 1/T, (b) activation energy versus OFG content.

Fig. 5.14(b) presents the evolution of the activation energy as a function of the OFG content. It is in the range 0.7- 0.9 eV, regardless of the OFG content.

5.2.4.4 MWS relaxation

The contribution of the conductivity ($\sigma_{DC}/\varepsilon_0\omega$) on ε_r” was then subtracted from the measured values to remove the ohmic conduction part in the loss spectra ε_r”. Fig. 5.15 presents the obtained values.

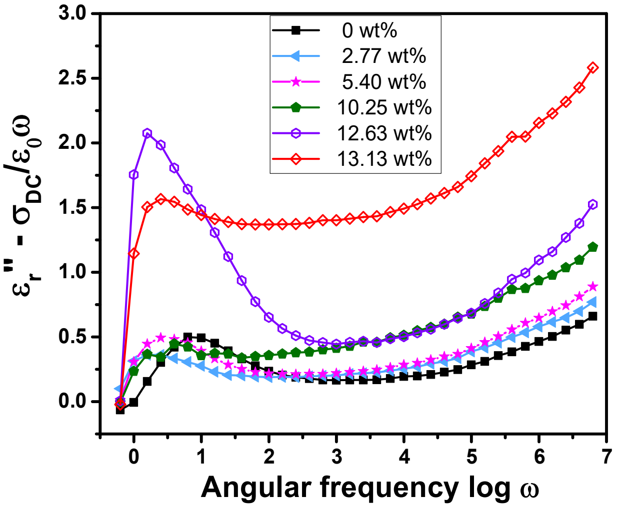

Fig. 5.15. Evolution of ε_r" without the DC conduction part versus angular frequency.

Relaxation peaks are visible in the corrected spectra, revealing the MWS relaxation. The Havriliak-Negami fitting results on conduction-free loss relaxation are presented in Fig.5.16 at ambient temperature (298 K).

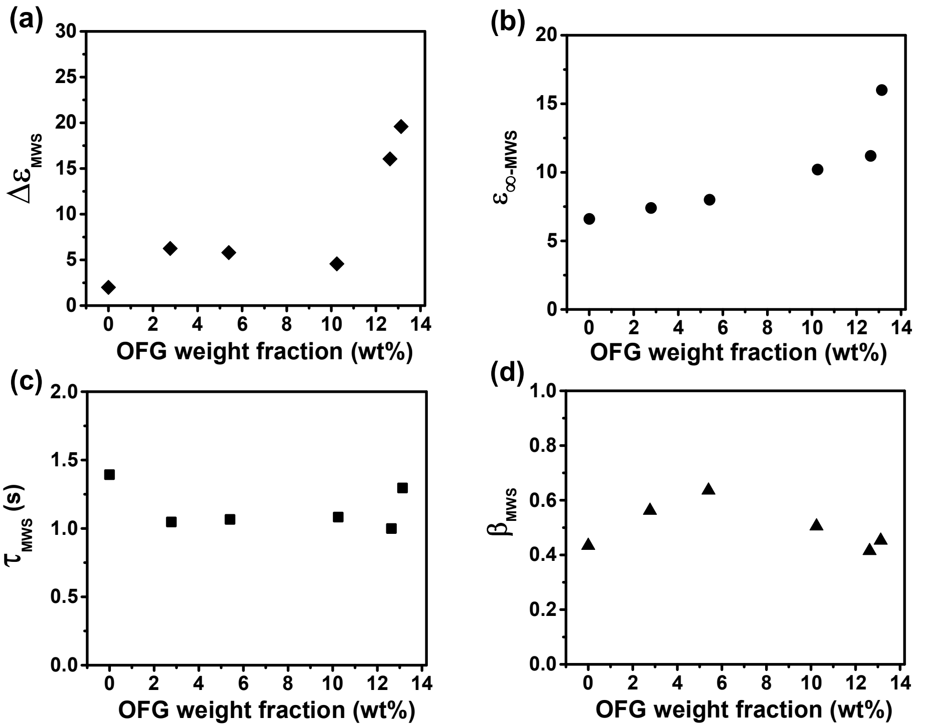

Fig. 5.16. Havriliak-Nagami fitting parameters versus OFG content for the MWS relaxation at ambient temperature (from DC conduction-free dielectric data): (a) dielectric dispersion $\Delta\varepsilon_{MWS}$, (b) high frequency permittivity $\varepsilon_{\infty MWS}$, (c) relaxation time τ_{MWS}, (d) spectra broadness parameter β_{MWS}.

The contribution of the MWS polarization to the permittivity is not so obvious. $\Delta\varepsilon_{MWS}$ is almost OFG content independent for the lower contents and an abruptly growth is only observed for contents in the vicinity of the percolation threshold. $\varepsilon_{\infty\text{-MWS}}$ presents an increase versus OFG content, in accordance with the contribution of α relaxation.

The relaxation time τ_{MWS} remains in the range 1.0-1.5 s, and is not significantly influenced by the OFG content. The parameter α is equal to 1 for all the compositions, evidencing that the distribution of the relaxation time is symmetric, whereas the β parameter lie in the range 0.4-0.65, displaying a significant broadness of the distribution. Both for PU and the PU/OFG composites, the MWS polarization do not relax at a single frequency. From the temperature dependence of the relaxation time (data not shown), the activation energy was determined to be in the range 0.1-0.35 eV. The E_a is not greatly affected by the OFG content and the low values obtained indicated a high dipole mobility.

In summary, both for MWS and α relaxation, it is observed an increase of the dielectric strength, which confirms the contribution of the fillers to the global polarization. For low and moderate OFG contents, the OFG contribution is more significant for the dipolar polarization (α) than for the interfacial polarization. The fillers do not affect significantly the activation energy for the 3 processes, namely α relaxation, MWS and DC conduction. The conduction analysis lead to a probable ionic origin of the charge carriers.

5.3 Possible origins of the limited improvement on M_{31}

5.3.1 Measured and calculated M_{31} of PU/OFG composites

According to the four-fold enhancement in permittivity and the moderate increase in Young's modulus with the incorporation of OFG, an improvement in M_{31} could be predicted by Maxwell effect. This paragraph is thus focused on M_{31} coefficient of PU/OFG composites measured by Bender method, as well as the one predicted by Maxwell effect.

5.3.1.1 Measured M_{31}

Fig. 5. 17 depicts the variation of S_{31} versus the square of electric filed amplitude for PU and composites.

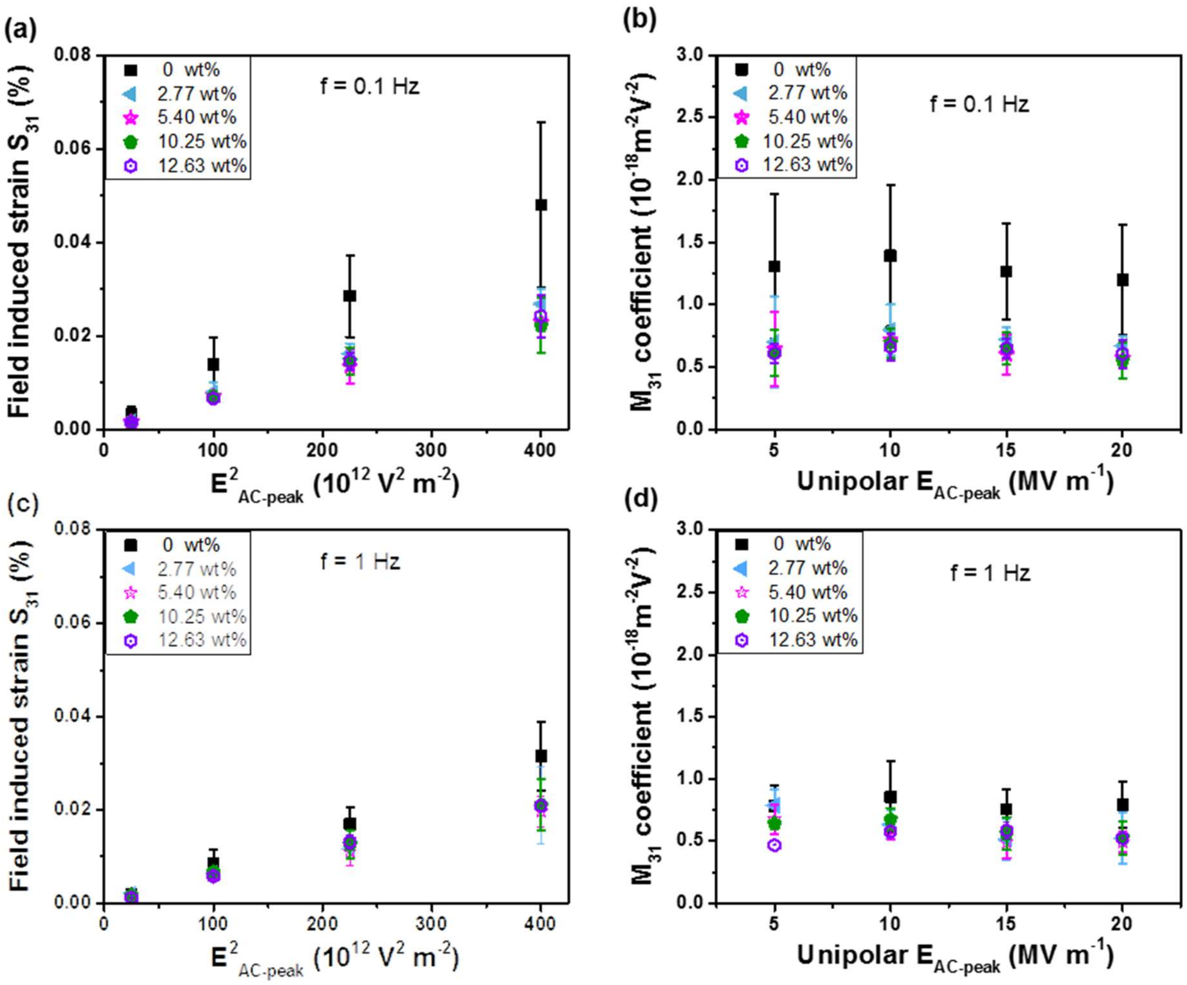

Fig. 5.17. Electromechanical performance of PU/OFG composites at 0.1 Hz and 1 Hz: (a), (c): field induced strain S_{31} versus the square of electric field; (b), (d): M_{31} coefficient versus electric field.

It can be observed for pure PU that the increase is not perfectly linear and shows a saturation at $E_{AC\text{-}peak}$> 15 MV m^{-1}. For all the PU/OFG composites, S_{31} are linear versus the square of $E_{AC\text{-}peak}$. However, S_{31} of all compositions show similar values in the $E_{AC\text{-}peak}$ range, and are surprisingly smaller than that of pure PU. Compared with pure PU, the dispersion of S_{31} is smaller in composites.

M_{31} coefficient of PU and composites were calculated from S_{31} and presented in Fig. 5. 17(b). The values of pure PU are dispersed in the given field range, and decrease at $E_{AC\text{-}peak}$ > 15 MV m^{-1}. Similar to S_{31}, the M_{31} values are similar and less dispersed for all the composition, and they are constant with the amplitude of electric field. However, despite an expecting enhancement of M_{31} by OFG incorporation, the M_{31} of PU/OFG composites remain smaller than the one of pure PU.

5.3.1.2 Comparison of measured M_{31} and calculated M_{31}

Fig. 5. 18 depicts the evolution of the measured and calculated M_{31} as a function of OFG content under 10 MV m^{-1} at 0.1 Hz.

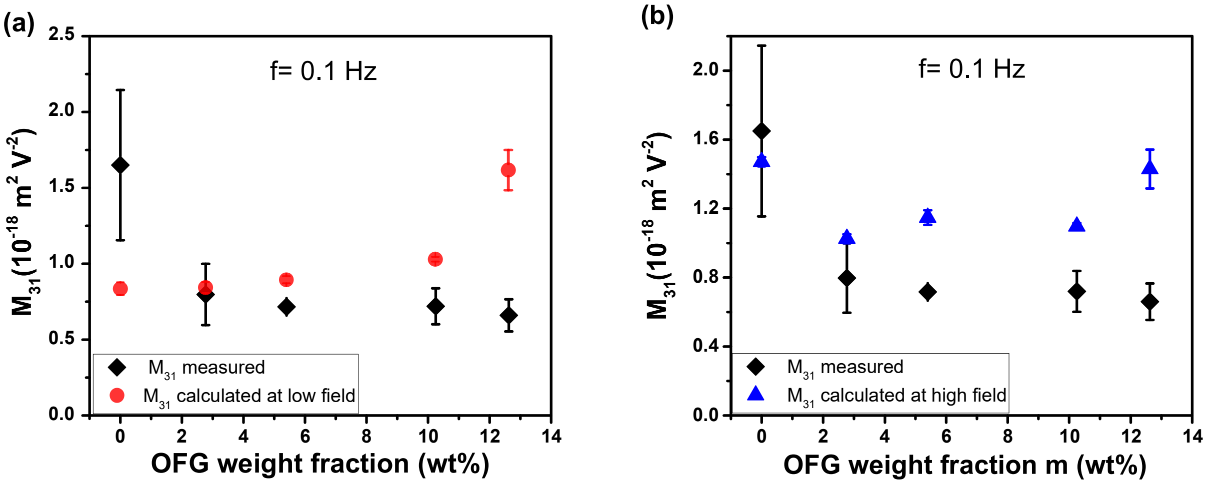

Fig. 5.18. Electromechanical coefficient M_{31} of PU/OFG composites as a function of OFG content at 0.1Hz: (a) M_{31} measured at 10 MV m^{-1} and $M_{31\text{-}1V}$ calculated with ε_r' obtained at 1 Vrms; (b) M_{31} measured at 10 MV m^{-1} and $M_{31\text{-}E}$ calculated with ε_r' and Y obtained at 10 MV m^{-1}.

As shown in Fig. 5 18(a), at 0.1 Hz, the M_{31} predicted with ε_r' obtained at 1 V_{RMS} and Y at neutral field increases with OFG content, firstly at a moderate level and then more dramatically near the percolation threshold. This increase is in good agreement with the large increase of ε_r', which is more important than the increase of Y (presented in 5.2). However, despite the predicted M_{31} improvement, the experimental M_{31} of composites remain lower than that of PU, and consist with 5.3.1.1, the M_{31} is similar among all the composition, with less dispersion than pure PU. The discordance between the measured and calculated M_{31} could be attributed to the different characterizing electric field used, since chapter 4 showed the great dependence of ε_r' on electric field (whereas Y is independent).

Fig. 5. 18(b) presents the M_{31} calculated with ε_r' measured at 10 MV m^{-1} with humidity rate in the range 43%- 47% (values in Fig. 5.2). The calculated M_{31} values of composites are smaller than that of pure PU (similar at 12.63 wt%), which agrees with the measured values. However, different from a better prediction obtained for pure PU, the calculated M_{31} of composites maintains a discrepancy to the measured values: the experimental M_{31} is always smaller than the calculated one, and the discrepancy increases with the OFG content.

Similar results were observed at 1 Hz, although the both measured and calculated M_{31} values are smaller, thus also the discrepancy between them.

The PU-10.25 wt%-OFG was taken as an example for further study. Following the conclusions of chapter 4, the experimental conditions (humidity level and electrical field amplitude) were carefully controlled, in order to ensure that they were the same during the bender measurement, and the measurements of permittivity and Young's modulus.

Figure 5.19 presents for PU-10.25 wt%-OFG composites, with different levels of humidity, a comparison between the measured and the calculated M_{31}.

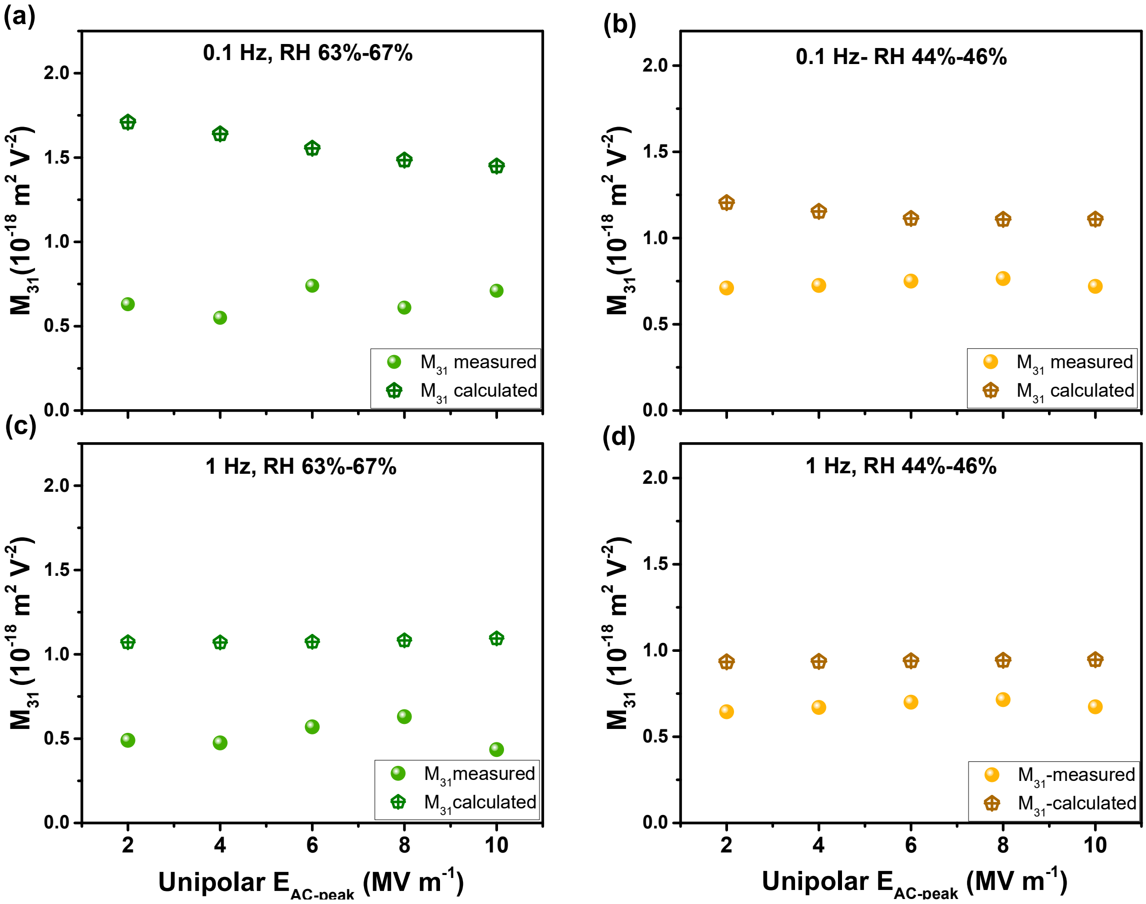

Fig. 5.19. The measured and calculated M_{31} of PU-10.25wt%-OFG at different humidity levels, 0.1 Hz: (a) high humidity, (b) medium humidity; 1 Hz: (c) high humidity, (d) medium humidity. Values of the 24th cycle presented for each $E_{AC\text{-}peak}$.

Contrary to that was observed on the PU films, the control of the experimental conditions does not explain discrepancies between measured and calculated electromechanical coefficients. This indicates that other factors need to be taken into account.

One possible hypothesis to explain the lower measured values can be the overestimation of the permittivity of PU/OFG composites, due to the conductive nature of the fillers, or the functionalization type.

The permittivity calculation from capacitance measurement ($\varepsilon_r'=C_pd/A$) is based on the model of plate capacitor, which assumes that the electrical field lines are perpendicular to the electrodes and the amplitude of the field is constant. In fact, the dispersion of conductive nanofillers within the polymer could have affected the field lines and the field amplitude, possibly leading permittivity values of discord.

In order to verify this hypothesis, comparisons were committed on PU composites with similar permittivity and Young's modulus, but different types of fillers: an isolating filler $BaTiO_3$, and graphene nanoplatelets with ammonia surface functionalization (NFG). Filler contents were carefully chosen to have the same permittivity as PU/OFG composites. In respect to these aims, PU-20 vol%-$BaTiO_3$ and PU-10.25 wt%-NFG were chosen. The permittivity, Young's modulus and M_{31} coefficient were characterized and compared.

5.3.2 PU composites with different type and functionalization of fillers

Fig. 5.20 presents the permittivity of PU-12.63 wt%-OFG, PU-20 vol%-$BaTiO_3$ and PU-10.25 wt%-NFG.

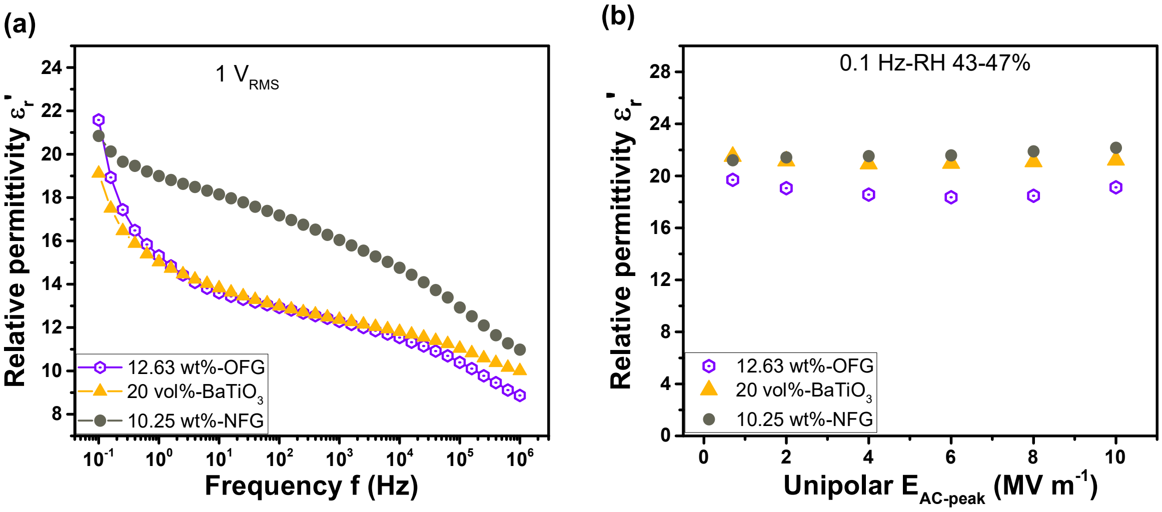

Fig. 5.20. The relative permittivity of PU-12.63wt%-OFG, PU-20 vol%-BaTiO3 and PU-10.25 wt%-NFG: (a) permittivity versus frequency at 1 VRMS, (b) versus electric field at 0.1 Hz.

The three composites with different type of fillers show similar permittivity values at 1 V_{RMS} in low frequency range. At 0.1 Hz, as PU-12.63 wt%-OFG, the permittivity of the two other composites are also independent on the amplitude of electric field, and the permittivity values of all three composites are close in $E_{AC\text{-}peak}$ range 0.7 -10 MV m^{-1} (between 19 and 22).

Fig. 5.21 presents SEM micrographs of PU-20 vol%-$BaTiO_3$, the fillers are quite homogeneously distributed and dispersed in the PU, and similary to OFG nanoplatelets, no preferring direction of the fillers arrangement is observed.

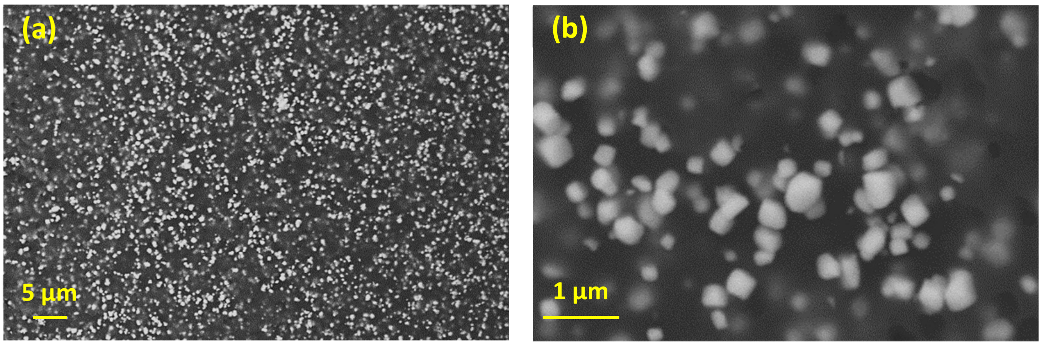

Fig. 5.21. SEM micrographs of a cryofractured (cross section, Au sputtered) surface of PU-20 vol%-$BaTiO_3$.

Table 5.2 presents the calculated and measured M_{31} obtained at the same conditions, for the three different composites with similar ε_r' and Y.

Table. 5.2. M_{31} calculated and M_{31} measured for PU composites with different types of fillers

Filler content	$\varepsilon_{r'}$ 10 MV m^{-1}, 0.1 Hz	Y (MPa) 0.1 %s^{-1}	M_{31} calculated (10^{-18} m^{2}V^{-2}) 10 MV m^{-1}, 0.1 Hz	M_{31} measured (10^{-18} m^{2}V^{-2}) 10 MV m^{-1}, 0.1 Hz
12.63wt%-OFG	19.1	59.1	1.4	0.66
20 vol%-$BaTiO_3$	21.2	59.1	1.6	0.86
10.25 wt%-NFG	22.2	59.8	1.6	0.67

With different nature of fillers (conductive OFG and isolating $BaTiO_3$), as well as different surface functionalization (OFG and NFG), the measured M_{31} exhibit always smaller values than the calculated ones. The calculated M_{31} are around two times the value of measured ones.

Therefore, in opposition to the previous hypothesis, the discrepancy between the predicted and the measured M_{31} could not be explained by the conductive nature nor the surface functionalization of fillers. Other factors must be considered.

5.3.3 Other possible origins

Another possible explanation could be that the interfacial polarization decreased the electric field seen by the composites and counterbalanced the increase in permittivity. As reported by Allayarov[180], mixing an electroactive polymer with conductive or high dielectric permittivity fillers can bring some disadvantages, by changing local fields values in the polymer and near the fillers.

Assuming that the reduced field is responsible for the obtained strain, then with the equation of Maxwell contribution and the measured S_{31}, a value of this depolarizing field can be estimated. The real field seen by the composites would be approximatively 7 MV/m instead of 10 MV/m. The consequence is that the extracted M_{31} using the applied field is different from the actual M_{31}, because the sample is driven by a lower electrical field than the applied one.

Other factors, such as a moderate mechanical interfacial adhesion as well as temperature fluctuations around the maximum of the relaxation peak, could also explain the values of the M_{31} coefficients.

5.4. Summary

The 3D distribution of nanoplatelets in the composites was confirmed by SEM analysis as well as the percolation law. The mechanical reinforcement remained modest probably due to a moderate adhesion between polymer and graphene nanoplatelets, highlighted by SEM and in agreement with over-estimated values predicted from the Halpin-Kardos model.

DSC experiments revealed that the microstructure of polyurethane was only sligthy affected by the presence of functionalized graphene, which cannot allow to undoubtedly conclude on the intrinsic role of the fillers.

As excepted, a large increase of the permittivity was obtained near the percolation threshold, as well as a decrease versus frequency. The variation in DC conductivity versus OFG content supported the fact that the OFG behaved as traps for the charged mobile species with the efficiency correlated to the distance between traps. The obtained activation energy lay in a range 0.7- 0.9 eV, regardless of the OFG content, pointing at an ionic origin of the conduction.

A detailed study was carried out on the dielectric relaxation peaks from -94°C to 80°C at low frequency, after removing the contribution of the DC conduction. Havriliak-Negami fitting indicates that the OFG contributes not only to Maxwell Wagner Sillars (MWS) polarization but also to dipolar polarization (α). At low and medium OFG contents, the contribution is more significant for dipolar relaxation than interfacial polarization.

One beneficial effect of introducing OFG to PU matrix is the stabilized dielectric properties in relation to the humidity and the electric field amplitude. However, the introduction of OFG does not always increase the permittivity under high electric field. It explains partially the less improved M_{31} than expected.

Different with the case of pure PU, for PU/OFG and PU/NFG composites, even with the well-controlled humidity and electric field, the calculated M_{31} is higher than the measured ones. Onepossible origin could be that the interfacial polarization decreased the electric field seen by the composites and counterbalanced the increase in permittivity. Other factors, such as a moderate mechanical interfacial adhesion as well as temperature fluctuations around the maximum of the relaxation peak, could also explain the values of the M_{31} coefficients.

Conclusion

The conclusion of the thesis summarizes the key points that allow us to answer the two question: What is the mechanism responsible for the field-induced strain in polyurethane? How the conductive nanofillers influence the electromechanical properties? It also points out the importance of carefully controlling the experimental conditions used for the elaboration process and the measurement of the properties.

The Bender and strain-stress methods proposed succeed to characterize the electromechanical coupling of EAPs. Comparing the Comsol-simulated and the experimentally measured values of M_{31} coefficient concludes to the major contribution of the Maxwell effect rather than the electrostriction phenomenon. Both methods lead to M_{31} values of PU in the same magnitude (10^{-18} m^2 V^{-2}), which is more precise than those reported in the literature are (10^{-19} to 10^{-13} m^2 V^{-2}), however, dispersion is still observed among the samples.

Whereas the M_{31} coefficient is measured at high levels of electric fields, the predicted value found in the literature is most often obtained from the permittivity and the Young's modulus measured at low levels. For the studied polyurethane, the discrepancy observed between the measured and calculated M_{31} is not due to the Young's modulus, which is electric field independent; but partially due to the dielectric properties, which vary with the characteristics of the electric field (signal form, amplitude, frequency and application duration).

Moreover, at high electric fields, the permittivity value is sensitive to other factors, including humidity, elaboration process, and temperature conditions. The permittivity value is influenced by a joint effect of humidity and electric field, which control the time needed to reach the steady state. The absorbed water in PU acts as plasticizer, and can contribute to the global polarization. The elaboration process could affect the number and type of hydrogen bonds that link the hard and the soft segments, and therefore can change the permittivity. A dielectric relaxation occurs close to the room temperature, a small temperature fluctuation can therefore significantly affect the PU properties.

With controlled conditions of humidity rate and electric field application, a good agreement was achieved between the measured and the calculated M_{31} values, for the studied PU and two others PU containing different HS/SS ratio.

PU/OFG nanocomposites with OFG content ranging from 2.77 wt% to 13.13 wt% were prepared using a solvent tape casting method. Experimental characterizations and data processing using dedicated physical laws reveal that the functionalized nanoplatelets are homogenously dispersed with a three-dimension distribution, but with a moderate interfacial cohesion with the PU matrix.

Comparing with neat PU, a 4-fold increase in permittivity is obtained with 12.63 wt% OFG, just before the percolation threshold (13.34 wt%).

Dielectric spectroscopy highlights that the OFG contributes to the interfacial polarization and the dipolar (α) polarization by increasing their dielectric strength. At low and medium OFG content, the contribution is more significant to the dipolar polarization than to the MWS polarization, whereas a higher increase of the MWS dielectric strength is generally expected with the incorporation of conductive fillers. A possible explanation could be that the random volumic distribution of nanofillers cannot allow a preferred orientation for the interfacial dipoles, especially at low contents.

The DC conductivity is also changed by the incorporation of nanofillers. It decreases with the incorporation of OFG for content less than 10.25 wt% certainly due to the functionalization layer, and then increases at higher OFG contents. The obtained value of activation energy for the conduction mechanism is favored for an ionic origin.

However, the significant permittivity increase and the modest mechanical reinforcement lead to an increase of the calculated M_{31}, but not to the experimental one, even with controlled experimental conditions. Same results were obtained with ammonia-functionalized graphene nanoplatelets, and with isolating barium titanate fillers, evidencing that the observed behavior is not linked to the type of fillers or the functionalization.

One beneficial effect of introducing OFG to PU matrix is to stabilize dielectric properties in respect of humidity rate and electric field amplitude. Yet it is also one of the reasons that explain the low electromechanical coupling obtained for the composites, since their permittivity under high electric are not increased likes PU.

Another possible explanation for observed discrepancy between the measured and calculated M_{31} is that the interfacial polarization reduces the local field, and counterbalanced the increase in permittivity. The moderate cohesion between OFG and PU matrix could also play a role.

This thesis shows the limitation of nanofillers incorporation method towards an enhancement of polyurethane electromechanical performance. Due to the heterogeneity of the polyurethane, this material already exhibits a good value of M_{31} coefficient.

The objectives of the thesis were certainly over-ambitious due the very complex nanostructure of the polyurethane and the fact that this industrial polymer contains some additives of unknown nature.

The polyurethane itself is complex and present a good electromechanical coupling. More research is needed for a deeper understanding of the induced field deformation, particularly in terms of electric charges such as ions diffusion. It will require a perfect control of the composition and the measurement conditions. It would be necessary to get closer to a laboratory which masters the polyurethane fabrication technology in order to avoid the additives use. Some changes on the microstructure should also be considered, for example play on the microphase separation rate from the starting monomers or plasticize the polyurethane.

Concerning the real role of the fillers, it appears of prime importance to consider less complex polymers, just to avoid the possible coupled effect between the intrinsic micro structural heterogeneity and the extrinsic one. Incorporating fillers into simple or model materials, with controlled composition and architecture, can help address some of the challenges, such as the actual role of fillers on the interfacial polarization and how their organization within the polymer influences the dipole distribution.

The electrode polarization can also be taken into consideration. It could be studied by changing the nature and geometry of the electrodes, and by varying the thickness of the EAP film.

The electromechanical performance of a flexible actuator is not only depending on the intrinsic properties of the polymer, but also on the geometry structure. The boundary conditions play an important role on the characteristics. A preliminary study was carried out and successfully lead to spaced line electrodes printed on polyurethane surface. With the help of 2D and 3D printing, it would be an interesting subject to improve the actuator performance by optimizing the electrode compliance.

For all these perspectives, more advanced characterizations should be conducted to deeply analyze the materials at the interface level. And the development of numerical tools such as finite elements calculations should also be a resource in this field.

References

1. Hunter, I. W. & Lafontaine, S. A comparison of muscle with artificial actuators. in *Technical Digest IEEE Solid-State Sensor and Actuator Workshop* 178–185 (IEEE, 1992).
2. Bar-Cohen, Y. *Electroactive polymer (EAP) actuators as artificial muscles: reality, potential and challenges*. (2003).
3. Goh, Y. F., Akbari, S., Khanh Vo, T. V. & Koh, S. J. A. Electrically-induced actuation of acrylic-based dielectric elastomers in excess of 500% strain. *Soft Robot.* **5**, 675–684 (2018).
4. Brochu, P. & Pei, Q. Advances in Dielectric Elastomers for Actuators and Artificial Muscles. 10–36 (2010). doi:10.1002/marc.200900425
5. Prahlad, H., Pelrine, R., Stanford, S., Marlow, J. & Kornbluh, R. Electroadhesive robots - Wall climbing robots enabled by a novel, robust, and electrically controllable adhesion technology. *Proc. - IEEE Int. Conf. Robot. Autom.* 3028–3033 (2008). doi:10.1109/ROBOT.2008.4543670
6. Pei, Q. *et al.* Recent progress on electroelastomer artificial muscles and their application for biomimetic robots. in *Smart Structures and Materials 2004: Electroactive Polymer Actuators and Devices (EAPAD)* **5385**, 41–50 (2004).
7. Bar-Cohen, Y. Electroactive Polymers as artifitial muscles- capabilities, potentials and challenges. in *Fourth International Conference and Exposition on Robotics for Challenging Situations and Environments* 188–196 (2000).
8. Carpi, F. & Rossi, D. De. Electroactive Polymer-Based Devices for e-Textiles in Biomedicine. in *IEEE Transactions on information technology in biomedicine* **9**, 295–318 (2005).
9. Gu, G., Zou, J., Zhao, R., Zhao, X. & Zhu, X. Soft wall-climbing robots. *Sci. Robot.* **3**, 1–13 (2018).
10. Tang, C., Li, B., Fang, H., Li, Z. & Chen, H. A speedy, amphibian, robotic cube: Resonance actuation by a dielectric elastomer. *Sensors Actuators, A Phys.* **270**, 1–7 (2018).
11. Must, I. *et al.* Ionic and capacitive artificial muscle for biomimetic soft robotics. *Adv. Eng. Mater.* **17**, 84–94 (2015).
12. Carpi, F., Kornbluh, R., Sommer-Larsen, P. & Alici, G. Electroactive polymer actuators as artificial muscles: Are they ready for bioinspired applications? *Bioinspiration and Biomimetics* **6**, (2011).
13. Bar-Cohen, Y. & Zhang, Q. M. Electroactive polymer actuators and sensors. *MRS Bull.* **33**, 173–177 (2008).
14. Das, R. *Electroactive polymers and devices 2013-2018: Forecasts, Technologies, Players*. (2018).
15. Osada, Y., Okuzaki, H. & Hori, H. A polymer gel woth electrical driven mobility. *Nature* **359**, 710–713 (1992).
16. Bar-Cohen, Y., Xue, T., Shahinpoor, M., Simpson, J. & Smith, J. Flexible, low-mass robotic arm actuated by electroactive polymers and operated equivalently to human arm and hand. *Robot. 1998* 15–21 (1998). doi:10.1061/40337(205)3
17. Wallmersperger, T., Kröplin, B. & Gülch, R. W. Coupled chemo-electro-mechanical formulation for ionic polymer gels - Numerical and experimental investigations. *Mech. Mater.* **36**, 411–420 (2004).
18. Hirai, T., Ueki, T. & Takasaki, M. Electrical Actuation of Textile Polymer Materials. *J. Fiber Bioeng. Informatics* **1**, 1–6 (2008).
19. Jungho, J., Kim, J., Woo, S. & Hee, J. Fabrication of ionic-polymer-metal-composite (IPMC) micropump using a commercial Nafion. **5385**, 272–280 (2004).
20. Aureli, M., Kopman, V. & Porfiri, M. Free-locomotion of underwater vehicles actuated by ionic polymer metal composites. *IEEE/ASME Trans. Mechatronics* **15**, 603–614 (2010).
21. Feng, G. H. & Tsai, J. W. Micromachined optical fiber enclosed 4-electrode IPMC actuator with

multidirectional control ability for biomedical application. *Biomed. Microdevices* **13**, 169–177 (2011).

22. Nguyen, T. T., Goo, N. S., Nguyen, V. K., Yoo, Y. & Park, S. Design, fabrication, and experimental characterization of a flap valve IPMC micropump with a flexibly supported diaphragm. *Sensors Actuators, A Phys.* **141**, 640–648 (2008).
23. Smela, E., Kallenbach, M. & Holdenried, J. Electrochemically driven polypyrrole bilayers for moving and positioning bulk micromachined silicon plates. *J. Microelectromechanical Syst.* **8**, 373–383 (1999).
24. Smela, E. C onjugated Polymer Actuators. **33**, 197–204 (2008).
25. Alici, G., Punning, A. & Shea, H. R. Enhancement of actuation ability of ionic-type conducting polymer actuators using metal ion implantation. *Sensors Actuators, B Chem.* **157**, 72–84 (2011).
26. Alici, G. & Higgins, M. J. Normal stiffness calibration of microfabricated tri-layer conducting polymer actuators. *Smart Mater. Struct.* **18**, (2009).
27. Baughman, R. H. *et al.* Carbon nanotube actuators. *Science (80-.).* **284**, 1340–1344 (1999).
28. Vinogradov, A. M., Schmidt, V. H., Tuthill, G. F. & Bohannan, G. W. Damping and electromechanical energy losses in the piezoelectric polymer PVDF. *Mech. Mater.* **36**, 1007–1016 (2004).
29. Min, S., Zhang, X., Zwiers, F. W. & Hegerl, G. C. Supplementary Information for Corrigendum. *Nature* **381**, 9–11 (2011).
30. Ma, Z., Scheinbeim, J. I., Lee, W. L. & Newman, B. A. High Field Electrostridive Response of Polymers. *J. Polym. Sci. Part B Polym. physcis* **32**, 2721–2731 (1994).
31. Zhang, Q. M., Su, J., Kim, C. H., Ting, R. & Capps, R. An experimental investigation of electromechanical responses in a polyurethane elastomer. *J. Appl. Phys.* **81**, 2770–2776 (1997).
32. Pelrine, R., Kornbluh, R., Pei, Q. & Joseph, J. High-Speed Electrically Actuated Elastomers with Strain Greater Than 100 %. *Science (80-.).* **287**, 836–839 (2000).
33. Jo, N. J. *et al.* Polyurethane-based Actuators with Various Polyols. *J. Mater. Sci. Technol.* **26**, 763–768 (2010).
34. Pelrine, R. *et al.* Dielectric Elastomer Artificial Muscle Actuators: Toward Biomimetic Motion. *Smart Struct. Mater.* **4695**, 126–137 (2002).
35. Carpi, F. & De Rossi, D. Biomimetic dielectric elastomer actuators. *Proc. First IEEE/RAS-EMBS Int. Conf. Biomed. Robot. Biomechatronics, 2006, BioRob 2006* **2006**, 1073–1078 (2006).
36. Ganet, F. *et al.* Haptic feedback using an all-organic electroactive polymer composite. *Sensors Actuators, B Chem.* **220**, 1120–1130 (2015).
37. Thetpraphi, K. *et al.* Advanced Plasticized Electroactive Polymers Actuators for Active Optical Applications: Live Mirror. *Adv. Eng. Mater.* **22**, (2020).
38. Huang, C. & Zhang, Q. Fully functionalized high-dielectric-constant nanophase polymers with high electromechanical response. *Adv. Mater.* **17**, 1153–1158 (2005).
39. Kim, I. J. *et al.* Development of high dielectric electrostrictive PVDF terpolymer blends for enhanced electromechanical properties. *Nanomaterials* **11**, 1–15 (2021).
40. Su, J., Harrison, J. S. & St. Clair, T. Novel polymeric elastomers for actuation. *IEEE Int. Symp. Appl. Ferroelectr.* **2**, 811–814 (2000).
41. Wang, Y., Sun, C., Zhou, E. & Su, J. Deformation mechanisms of electrostrictive graft elastomer. *Smart Mater. Struct.* **13**, 1407–1413 (2004).
42. Pei, Q., Pelrine, R., Stanford, S., Kornbluh, R. & Rosenthal, M. Electroelastomer rolls and their application for biomimetic walking robots. *Synth. Met.* **135–136**, 129–131 (2003).
43. Smela, E. Conjugated polymer actuators for biomedical applications. *Adv. Mater.* **15**, 481–494 (2003).
44. Yamaguchi, A., Takemura, K., Yokota, S. & Edamura, K. A robot hand using electro-conjugate

fluid: Grasping experiment with balloon actuators inducing a palm motion of robot hand. *Sensors Actuators, A Phys.* **174**, 181–188 (2012).

45. Shintake, J., Rosset, S., Schubert, B., Floreano, D. & Shea, H. Versatile Soft Grippers with Intrinsic Electroadhesion Based on Multifunctional Polymer Actuators. *Adv. Mater.* **28**, 231–238 (2016).
46. Diaconu, I. & Dorohoi, D. Properties of polyurethane thin films. *J. Optoelectron. Adv. Mater.* **7**, 921–924 (2005).
47. Rhone, B. Étude de la réactivité des uréthanes et polyuréthanes : application aux dispositifs médicaux To cite this version : HAL Id : tel-02401862 Université Pierre et Marie Curie Thèse de doctorat Spécialité chimie Etude de la réactivité des uréthanes et polyurét. (2019).
48. Hibon, S. Elaboration de formulations Polyuréthane/Nanocharges minérales: Influence des charges sur la synthèse des prépolymères. 201 (2006).
49. Xie, F. *et al.* Degradation and stabilization of polyurethane elastomers. *Prog. Polym. Sci.* **90**, 211–268 (2019).
50. Zhang, C., Hu, J., Chen, S. & Ji, F. Theoretical study of hydrogen bonding interactions on MDI-based polyurethane. *J. Mol. Model.* **16**, 1391–1399 (2010).
51. Biggs, J. *et al.* Electroactive polymers: Developments of and perspectives for dielectric elastomers. *Angew. Chemie - Int. Ed.* **52**, 9409–9421 (2013).
52. Mohammed, S. & Billah, R. Dielectric Polymers. in *Functional polymers, polymers and polymeric composites: A reference series* (Springer, 2018).
53. Ishai, P. Ben, Talary, M. S., Caduff, A., Levy, E. & Feldman, Y. Electrode polarization in dielectric measurements : a review. *Meas. Sci. Technol.* **102001**, 1–21 (2013).
54. Kwan, C. K. *Dielectric phenomena in solids*. (Elsevier, 2004).
55. Szycher, M. *Szycher's Handbook of Polyurethanes*. (CRS press, 2017).
56. Musteata, V. E., Filip, D., Vlad, S. & Macocinschi, D. Dielectric relaxation of polyurethane biocomposites. *Optoelectron. Adv. Mater. Rapid Commun.* **4**, 1187–1192 (2010).
57. Peiris, T. A. N. related electronic and optoelectronic applications Institutional Repository Microwave-assisted processing of solid materials for sustainable energy related electronic and optoelectronic applications submitted to Loughborough University ' s l. (Loughborough University, 2014).
58. Menczel, J. & Prime, R. *Thermal analysis of polymers*. (John Wiley & Sons, Inc., 2009).
59. Kao, K. chi. *Dielectric Phenomena in Solids With Emphasis on Physical Concepts of Electronic Processes*. (Elsevier, 2004). doi:https://doi.org/10.1016/B978-0-12-396561-5.X5010-5
60. Cole, K. S. & Cole, R. H. Dispersion and Absorption in Dielectrics II. Direct Current Characteristics. **98**, (1942).
61. Davidson, D. W. & Cole, R. H. Dielectric Relaxation in Glycerol, Propylene Glycol, and nPropanol. **1484**, (1951).
62. Havriliak, S. & Negami, S. A complex plane analysis of α-dispersions in some polymer systems. *J. Polym. Sci. Part C Polym. Symp.* **14**, 99–117 (1966).
63. Tsangaris, G. M., Psarras, G. C. & Kouloumbi, N. Electric modulus and interfacial polarization in composite polymeric systems. *J. Mater. Sci.* **33**, 2027–2037 (1998).
64. Samir, Z. *et al.* Dielectric behaviour of carbon nanotubes particles-filled polyester polymer composites. *J. Compos. Mater.* **51**, 1831–1837 (2017).
65. Kanapitsas, A., Pissis, P. & Kotsilkova, R. Dielectric studies of molecular mobility and phase morphology in polymer-layered silicate nanocomposites. *J. Non. Cryst. Solids* **305**, 204–211 (2002).
66. Das, S. & Ghosh, A. Effect of plasticizers on ionic conductivity and dielectric relaxation of PEO-LiClO4 polymer electrolyte. *Electrochim. Acta* **171**, 59–65 (2015).

67. Bordi, F., Cametti, C. & Colby, R. H. Dielectric spectroscopy and conductivity of polyelectrolyte solutions. *J. Phys. Condens. Matter* **16**, (2004).

68. Kremer, F. & Schönhals, A. *Broadband dielectric spectroscopy*. (Springer, 2003).

69. Wang, L. W. & Fecht, H. J. A kinetic model for liquids: Relaxation in liquids, origin of the Vogel-Tammann-Fulcher equation, and the essence of fragility. *J. Appl. Phys.* **104**, (2008).

70. Walters, C. Temperature Dependency of Molecular Mobility in Preserved Seeds. *Biophys. J.* **86**, 1253–1258 (2004).

71. Jonscher, A. K. The 'universal' dielectric response. *Nature* **267**, 673–679 (1977).

72. Li, Z., Du, B., Han, C. & Xu, H. Trap modulated charge carrier transport in polyethylene/graphene nanocomposites. *Sci. Rep.* **7**, 1–8 (2017).

73. Papathanassiou, A. N., Sakellis, I. & Grammatikakis, J. Universal frequency-dependent ac conductivity of conducting polymer networks. *Appl. Phys. Lett.* **91**, 2005–2008 (2007).

74. Cramer, C., Brunklaus, S., Ratai, E. & Gao, Y. New mixed alkali effect in the ac conductivity of ion-conducting glasses. *Phys. Rev. Lett.* **91**, 1–4 (2003).

75. Louati, B., Gargouri, M., Guidara, K. & Mhiri, T. AC electrical properties of the mixed crystal (NH4) 3H(SO4)1.42(SeO4)0.58. *J. Phys. Chem. Solids* **66**, 762–765 (2005).

76. Srivastava, N. & Kumar, M. Ion dynamics behavior in solid polymer electrolyte. *Solid State Ionics* **262**, 806–810 (2014).

77. Kumar, M., Tiwari, T., Chauhan, J. K. & Srivastava, N. Understanding the ion dynamics and relaxation behavior from impedance spectroscopy of NaI doped Zwitterionic polymer system Manindra. *Mater. Res. Express* **1**, (2014).

78. Shkel, Y. M., Klingenberg, D. J., Shkel, Y. M. & Klingenberg, D. J. Material parameters for electrostriction Material parameters for electrostriction. *J. Appl. Phys.* **80**, 4566–4572 (1996).

79. Kracovsky, I. & Romijn, T. A few remarks on the electrostriction of elastomers. *J. Appl. Phys.* **85**, 628–629 (1999).

80. Shkel, Y. M. & Klingenberg, D. J. Material parameters for electrostriction. *J. Appl. Phys.* **80**, 4566–4572 (1996).

81. Guillot, F. M. & Jarzynski, J. Measurement of electrostrictive coefficients of polymer films. *J. Acoust. Soc. Am.* **110**, 2980–2990 (2001).

82. Su, J., Zhang, Q. M. & Ting, R. Y. Space-charge-enhanced electromechanical response in thin-film Polyurethane elastomers. *Appl. Phys. Lett.* **71**, 386–388 (1997).

83. Su, J., Moses, P. & Zhang, Q. M. A bimorph based dilatometer for field induced strain measurement in soft and thin free standing polymer films. *Rev. Sci. Instrum.* **69**, 2480–2483 (1998).

84. Watanabe, M., Suzuki, M., Hirako, Y., Shirai, H. & Hirai, T. Hysteresis in bending electrostriction of polyurethane films. *J. Appl. Polym. Sci.* **79**, 1121–1126 (2001).

85. Lim, H. O., Bark, G. M., Park, H., Chun, H. H. & Jo, N. J. High-field Maxwell stress effect of dielectric actuator based on segmented polyurethane. *Adv. Mater. Res.* **26–28**, 753–756 (2007).

86. Renard, C. *et al.* Plasticized thermoplastic polyurethanes for dielectric elastomers with improved electromechanical actuation. *J. Appl. Polym. Sci.* **134**, 45123 (2017).

87. Guillot, F. M. & Balizer, E. Electrostrictive effect in polyurethanes. *J. Appl. Polym. Sci.* **89**, 399–404 (2003).

88. Wang, H. *et al.* The Origins of Electromechanical Response in Polyurethane Elastomers. in *IEEE International Symposium on Applications of Ferroelectrics* 182–185 (1994).

89. Newnham, R. E., Sundar, V., Yimnirun, R., Su, J. & Zhang, Q. M. Electrostriction: Nonlinear electromechanical coupling in solid dielectrics. *J. Phys. Chem. B* **101**, 10141–10150 (1997).

90. Diaconu, I., Dorohoi, D. & Topoliceanu, F. Electrostriction of a Polyurethane. *IEEE Sens. J.* **6**, 876–880 (2006).

91. Ardimas, Putson, C. & Muensit, N. High electromechanical performance of modified electrostrictive polyurethane three-phase composites. *Compos. Sci. Technol.* **158**, 164–174 (2018).

92. Dang, Z. M., Wang, L., Yin, Y., Zhang, Q. & Lei, Q. Q. Giant dielectric permittivities in functionalized carbon-nanotube/ electroactive-polymer nanocomposites. *Adv. Mater.* **19**, 852–857 (2007).

93. Carpi, F., Gallone, G., Galantini, F. & De Rossi, D. Silicone-poly(hexylthiophene) blends as elastomers with enhanced electromechanical transduction properties. *Adv. Funct. Mater.* **18**, 235–241 (2008).

94. Romasanta, L. J., Lopez-Manchado, M. A. & Verdejo, R. Increasing the performance of dielectric elastomer actuators: A review from the materials perspective. *Prog. Polym. Sci.* **51**, 188–211 (2015).

95. Zhang, Q. M., Bharti, V. & Zhao, X. Giant Electrostriction and Relaxor Ferroelectric Behavior in Electron-Irradiated Poly (vinylidene fluoride-trifluoroethylene) Copolymer. *Science (80-.).* **280**, 2102–2104 (1997).

96. Zhang, Q. M. *et al.* An all-organic composite actuator material with a high dielectric constant. *Nature* **419**, 284–287 (2002).

97. Capsal, J. F., Galineau, J., Lallart, M., Cottinet, P. J. & Guyomar, D. Plasticized relaxor ferroelectric terpolymer: Toward giant electrostriction, high mechanical energy and low electric field actuators. *Sensors Actuators, A Phys.* **207**, 25–31 (2014).

98. Wang, J. W., Shen, Q. D., Bao, H. M., Yang, C. Z. & Zhang, Q. M. Microstructure and dielectric properties of P(VDF-TrFE-CFE) with partially grafted copper phthalocyanine oligomer. *Macromolecules* **38**, 2247–2252 (2005).

99. Park, C., Kang, J. H., Harrison, J. S., Costen, R. C. & Lowther, S. E. Actuating single wall carbon nanotube-polymer composites: Intrinsic unimorphs. *Adv. Mater.* **20**, 2074–2079 (2008).

100. Panahi-Sarmad, M., Zahiri, B. & Noroozi, M. Graphene-based composite for dielectric elastomer actuator: A comprehensive review. *Sensors Actuators A Phys.* **293**, 222–241 (2019).

101. Wongtimnoi, K. *et al.* Improvement of electrostrictive properties of a polyether-based polyurethane elastomer filled with conductive carbon black. *Compos. Sci. Technol.* **71**, 885–892 (2011).

102. Li, Q., Xue, Q., Hao, L., Gao, X. & Zheng, Q. Large dielectric constant of the chemically functionalized carbon nanotube/polymer composites. *Compos. Sci. Technol.* **68**, 2290–2296 (2008).

103. Zhang, B. T., Zheng, X., Li, H. F. & Lin, J. M. Application of carbon-based nanomaterials in sample preparation: A review. *Anal. Chim. Acta* **784**, 1–17 (2013).

104. Fook, T. H. T., Jeon, J. H. & Lee, P. S. Transparent flexible polymer actuator with enhanced output force enabled by conductive nanowires interlayer. *Adv. Mater. Technol.* **5**, 1–9 (2020).

105. Sun, H. *et al.* Interfacial polarization and dielectric properties of aligned carbon nanotubes/polymer composites: The role of molecular polarity. *Compos. Sci. Technol.* **154**, 145–153 (2018).

106. Ramanathan, T. *et al.* Functionalized graphene sheets for polymer nanocomposites. *Nat. Nanotechnol.* **3**, 327–331 (2008).

107. Jomaa, M. H. *et al.* Investigation of elastic, electrical and electromechanical properties of polyurethane/grafted carbon nanotubes nanocomposites. *Compos. Sci. Technol.* **121**, 1–8 (2015).

108. Hedi, J. M. Elaboration, characterization and modeling of electroactive materials based on polyurethane and grafted carbon nanotubes. (INSA-Lyon, 2015).

109. Deshmukh, S. & Ounaies, Z. Single walled carbon nanotube (SWNT)-polyimide nanocomposites as electrostrictive materials. *Sensors Actuators, A Phys.* **155**, 246–252 (2009).

110. Lebrun, L., Guyomar, D., Guiffard, B., Cottinet, P. J. & Putson, C. The Characterisation of the harvesting capabilities of an electrostrictive polymer composite. *Sensors Actuators, A Phys.* **153**, 251–257 (2009).

111. Liu, S. *et al.* Aligned carbon nanotubes stabilized liquid phase exfoliated graphene hybrid and their polyurethane dielectric elastomers. *Compos. Sci. Technol.* **125**, 30–37 (2016).

112. Tian, M. *et al.* Thermally expanded graphene nanoplates/polydimethylsiloxane composites with high dielectric constant, low dielectric loss and improved actuated strain. *Compos. Sci. Technol.* **99**, 37–44 (2014).

113. Pichon, P. Fatigue thermomécanique des élastomères polyuréthane. (INSA-Lyon, 2010).

114. Wongtimnoi, K. Polyuréthanes électrostrictifs et nanocomposites: caractérisation et analyse des mécanismes de couplages électromécaniques. (INSA-Lyon, 2011).

115. Effective Dispersion of Graphene and Graphene Oxide. (2014). Available at: https://www.azonano.com/article.aspx?ArticleID=3935%0AP.

116. Haydale's plasma processing technique. Available at: https://haydale.com/products/functionalised-graphene-and-nanocomposites/.

117. Functionalized GNPs. Available at: https://graphene-supermarket.com/Functionalized-GNPs/.

118. Barium titanate nanopowder. Available at: https://www.us-nano.com/inc/sdetail/416.

119. Oprea, S. Effect of solvent interactions on the properties of polyurethane films. *High Perform. Polym.* **17**, 163–173 (2005).

120. McCrum, N. G., Read, B. E. & Williams, G. *Anelastic and dielectric effects in polymeric solids*. (Wiley, 1967).

121. Wang, Q. & Cross, L. E. Performance analysis of piezoelectric cantilever bending actuators. *Ferroelectrics* **215**, 187–213 (1998).

122. RESNIK, S. L., FAVETTO, G., CHIRIFE, J. & FONTAN, C. F. A World Survey of Water Activity of Selected Saturated Salt Solutions used as Standards at 25°C. *J. Food Sci.* **49**, 510–513 (1984).

123. Jomaa, M. H., Seveyrat, L., Lebrun, L., Masenelli-Varlot, K. & Cavaille, J. Y. Dielectric properties of segmented polyurethanes for electromechanical applications. *Polymer (Guildf).* **63**, 214–221 (2015).

124. Ian M, W. & John Sweeney. *Mechanical Properties of Solid Polymer*. (Wiley, 2012).

125. Espinosa, H. D. & Prorok, B. C. Mechanical properties of MEMS structures size effects on the mechanical behavior of gold thin films. *J. Mater. Sci.* **8**, 4125–4128 (2003).

126. Wang, L., Liang, C. & Prorok, B. C. A comparison of testing methods in assessing the elastic properties of sputter-deposited gold films. *Thin Solid Films* **515**, 7911–7918 (2007).

127. Zou, H. X. *et al.* Design and experimental investigation of a magnetically coupled vibration energy harvester using two inverted piezoelectric cantilever beams for rotational motion. *Energy Convers. Manag.* **148**, 1391–1398 (2017).

128. Ajitsaria, J., Choe, S. Y., Shen, D. & Kim, D. J. Modeling and analysis of a bimorph piezoelectric cantilever beam for voltage generation. *Smart Mater. Struct.* **16**, 447–454 (2007).

129. Inman, D. J. & Singh, R. C. *Engineering vibration*. **3**, (Prentice Hall Englewood Cliffs, NJ, 1994).

130. Eury, S. *et al.* Converse electrostriction in polymers and composites. *Mater. Chem. Phys.* **61**, 18–23 (1999).

131. Wilhelm, C. & Gardette, J. L. Infrared analysis of the photochemical behaviour of segmented polyurethanes: Aliphatic poly(ether-urethane)s. *Polymer (Guildf).* **39**, 5973–5980 (1998).

132. Pellizzi, E. Étude Du Vieillissement Des Mousses De Polyuréthane Ester Et Consolidation Par Les Aminoalkylalkoxysilanes. 1–13 (2012).

133. Rosu, D., Rosu, L. & Cascaval, C. N. IR-change and yellowing of polyurethane as a result of UV irradiation. *Polym. Degrad. Stab.* **94**, 591–596 (2009).

134. Hernandez, R. *et al.* A comparison of phase organization of model segmented polyurethanes with different intersegment compatibilities. *Macromolecules* **41**, 9767–9776 (2008).

135. Castagna, A. M., Fragiadakis, D., Lee, H., Choi, T. & Runt, J. The role of hard segment content on the molecular dynamics of poly(tetramethylene oxide)-based polyurethane copolymers. *Macromolecules* **44**, 7831–7836 (2011).

136. Coates, J. Interpretation of Infrared Spectra, A Practical Approach. *Encycl. Anal. Chem.* 1–23 (2006). doi:10.1002/9780470027318.a5606

137. Singh, R. P., Tomer, N. S. & Bhadraiah, S. V. Photo-oxidation studies on polyurethane coating: Effect of additives on yellowing of polyurethane. *Polym. Degrad. Stab.* **73**, 443–446 (2001).

138. Coleman, M. M., Lee, K. H., Skrovanek, D. J. & Painter, P. C. Hydrogen Bonding in Polymers. 4. Infrared Temperature Studies of a Simple Polyurethane. *Macromolecules* **19**, 2149–2157 (1986).

139. Hsieh, A. J. *et al.* Bottom-up Design toward Dynamically Robust Polyurethane Elastomers. *Polymer (Guildf).* **218**, 123518 (2021).

140. Martin, D. J., Meijs, G. F., Renwick, G. M., McCarthy, S. J. & Gunatillake, P. A. The effect of average soft segment length on morphology and properties of a series of polyurethane elastomers. I. Characterization of the series. *J. Appl. Polym. Sci.* **62**, 1377–1386 (1996).

141. Son, T. W., Lee, W. D. & Lim, S. K. Thermal and Phase Behavior of Polyurethane Based on Chain Extender, 2,2-Bis-[4-(2-hydroxyethoxy)phenyl]propane. **31**, 563–568 (1999).

142. Korley, L. S. T. J., Pate, B. D., Thomas, E. L. & Hammond, P. T. Effect of the degree of soft and hard segment ordering on the morphology and mechanical behavior of semicrystalline segmented polyurethanes. *Polymer (Guildf).* **47**, 3073–3082 (2006).

143. Koberstein, J. T. & Russell, T. P. Simultaneous SAXS-DSC study of multiple endothermic behavior in polyether-based polyurethane block copolymers. *Macromolecules* **19**, 714–720 (1986).

144. Crawford, D. M., Bass, R. G. & Haas, T. W. Strain effects on thermal transitions and mechanical properties of thermoplastic polyurethane elastomers. *Thermochim. Acta* **323**, 53–63 (1998).

145. Lapprand, A., Méchin, F. & Pascault, J.-P. Synthesis and Properties of Self-Crosslinkable Thermoplastic Polyurethanes. *J. Appl. Polym. Sci.* **105**, 99–113 (2007).

146. Król, P. Synthesis methods, chemical structures and phase structures of linear polyurethanes. Properties and applications of linear polyurethanes in polyurethane elastomers, copolymers and ionomers. *Prog. Mater. Sci.* **52**, 915–1015 (2007).

147. Kim, B. K. & Lee, J. C. Waterborne polyurethanes and their properties. *J. Polym. Sci. Part A Polym. Chem.* **34**, 1095–1104 (1996).

148. Kim, E. Y. *et al.* Synthesis and properties of highly hydrophilic waterborne polyurethane-ureas containing various hardener content for waterproof breathable fabrics. *J. Appl. Polym. Sci.* **129**, 1745–1751 (2013).

149. Pissis, P. *et al.* Water effects in polyurethane block copolymers. *J. Polym. Sci. Part B Polym. Phys.* **34**, 1529–1539 (1996).

150. Pissis, P., Anagnostopoulou-Konsta, A., Apekis, L., Daoukaki-Diamanti, D. & Christodoulides, C. Dielectric effects of water in water-containing systems. *J. Non. Cryst. Solids* **131–133**, 1174–1181 (1991).

151. Li, C., Xia, H. & Ni, Q. Q. Actuation Characteristics and Mechanism of Electroactive Plasticized Thermoplastic Polyurethane. *Langmuir* **36**, 14933–14941 (2020).

152. Renard, C. *et al.* Plasticized thermoplastic polyurethanes for dielectric elastomers with improved electromechanical actuation. *J. Appl. Polym. Sci.* **134**, 1–10 (2017).

153. Li, C., Xia, H., Yao, J. & Ni, Q. Q. Electrically induced soft actuators based on thermoplastic polyurethane and their actuation performances including tiny force measurement. *Polymer (Guildf).* **180**, 121678 (2019).

154. Garces, I. T., Aslanzadeh, S., Boluk, Y. & Ayranci, C. Effect of moisture on shape memory polyurethane polymers for extrusion-based additive manufacturing. *Materials (Basel).* **12**, (2019).

155. Gorrasi, G. *et al.* Vapor barrier properties of polycaprolactone montmorillonite nanocomposites: Effect of clay dispersion. *Polymer (Guildf).* **44**, 2271–2279 (2003).

156. Kopsidas, S., Olowojoba, G. B., Kinloch, A. J. & Taylor, A. C. Examining the effect of graphene nanoplatelets on the corrosion resistance of epoxy coatings. *Int. J. Adhes. Adhes.* **104**, 102723 (2021).

157. Hull, D. & Clyne, T. W. *An introduction to composite materials*. (Cambridge University Press, 1996).

158. Kim, H. S., Hong, S. I. & Kim, S. J. On the rule of mixtures for predicting the mechanical properties of composites with homogeneously distributed soft and hard particles. *J. Mater. Process. Technol.* **112**, 109–113 (2001).

159. Guth, E. Theory of Filler Reinforcement Theory of Filler Reinforcement . **20**, (1945).

160. Halpin, J. C. & Kardos, J. L. The Halpin-Tsai Equations: A Review. **16**, (1976).

161. Hill, R. A self-consistent mechanics of composite materials. *J. Mech. Phys. Solids* **13**, 213–222 (1965).

162. Harito, C., Bavykin, D. V. & Walsh, F. C. Incorporation of titanate nanosheets to enhance mechanical properties of water-soluble polyamic acid. *IOP Conf. Ser. Mater. Sci. Eng.* **223**, (2017).

163. Ebadi-Dehaghani, H., Khonakdar, H. A., Barikani, M. & Jafari, S. H. Experimental and theoretical analyses of mechanical properties of PP/PLA/clay nanocomposites. *Compos. Part B Eng.* **69**, 133–144 (2015).

164. Park, S. *et al.* Mechanoelectrical properties of a GnF/PDMS composite controlled by the aspect ratio and concentration of GnF. *Compos. Sci. Technol.* **159**, 77–86 (2018).

165. Lee, C., Wei, X., Kysar, J. W. & Hone, J. Measurement of the elastic properties and intrinsic strength of monolayer graphene. *Science (80-.).* **321**, 385–388 (2008).

166. Tsai, J. L. & Tu, J. F. Characterizing mechanical properties of graphite using molecular dynamics simulation. *Mater. Des.* **31**, 194–199 (2010).

167. Scarpa, F., Adhikari, S. & Srikantha Phani, A. Effective elastic mechanical properties of single layer graphene sheets. *Nanotechnology* **20**, (2009).

168. Lee, C. *et al.* Elastic and frictional properties of graphene. *Phys. Status Solidi Basic Res.* **246**, 2562–2567 (2009).

169. Gong, L. *et al.* Optimizing the reinforcement of polymer-based nanocomposites by graphene. *ACS Nano* **6**, 2086–2095 (2012).

170. Pierson, H. O. *Handbook of Carbon, Graphite, Diamonds and Fullerenes*. (Noyes Publications, 1993).

171. Stauffer, D. & Amnon, A. *Introduction to percolation theory*. (Taylor & Francis Ltd, 1994).

172. Myroshnychenko, V. & Brosseau, C. Effective complex permittivity of two-phase random composite media: A test of the two exponent phenomenological percolation equation. *J. Appl. Phys.* **103**, 1–10 (2008).

173. Grannan, D. M., Garland, J. C. & Tanner, D. B. Critical behavior of the dielectric constant of a random compostie near the percolation threshold. *Phys. Rev. Lett.* **46**, 375–378 (1980).

174. Nan, C. W. Physics of inhomogeneous inorganic materials. *Prog. Mater. Sci.* **37**, 1–116 (1993).

175. El Bouazzaoui, S., Droussi, A., Achour, M. E. & Brosseau, C. Nonuniversal percolation exponents and broadband dielectric relaxation in carbon black loaded epoxy composites. *J. Appl. Phys.* **106**, 104107 (2009).

176. Fredin, L. A., Li, Z., Lanagan, M. T., Ratner, M. A. & Marks, T. J. Substantial recoverable energy storage in percolative metallic aluminum-polypropylene nanocomposites. *Adv. Funct. Mater.* **23**, 3560–3569 (2013).

177. Khurram, A. A., Rakha, S. A., Zhou, P., Shafi, M. & Munir, A. Correlation of electrical conductivity, dielectric properties, microwave absorption, and matrix properties of composites

filled with graphene nanoplatelets and carbon nanotubes. *J. Appl. Phys.* **118**, 044105 (2015).

178. Ichikawa, K. & Macknightt, W. J. polymers. **33**, 4693–4698 (1992).

179. Turnhout, J. Van & Michael, W. Analysis of complex dielectric spectra . I . One-dimensional derivative techniques and three-dimensional modelling. *J. Non. Cryst. Solids* **305**, 40–49 (2002).

180. Allahyarov, E., Löwen, H. & Zhu, L. Dipole correlation effects on the local field and the effective dielectric constant in composite dielectrics containing high-: K inclusions. *Phys. Chem. Chem. Phys.* **18**, 19103–19117 (2016).

List of Figures

List of tables

List of publications

1. Zhang, Y., Perrin, V., Seveyrat, L. & Lebrun, L. On a better understanding of the electromechanical coupling in electroactive polyurethane. *Smart Mater. Struct.* **29**, 055007 (2020).
2. Zhang, Y., Seveyrat, L. & Lebrun, L. Dielectric and electromechanical properties of EAP/oxygen functionalized graphene nanocomposites. in *2020 IEEE 3rd International Conference on Dielectrics (ICD)* 265–268 (2020).
3. Zhang, Y., Seveyrat, L. & Lebrun, L. Correlation between dielectric, mechanical properties and electromechanical performance of functionalized graphene / polyurethane nanocomposites. *Compos. Sci. Technol. (2021).*

FOLIO ADMINISTRATIF

THESE DE L'UNIVERSITE DE LYON OPEREE AU SEIN DE L'INSA LYON

NOM : **ZHANG** DATE de SOUTENANCE : **29 Avril 2021**
(avec précision du nom de jeune fille, le cas échéant)

Prénoms: **Yan**

TITRE : **Toward a better understanding and control of polyurethane composite films behavior for actuators**

NATURE : **Doctorat** Numéro d'ordre : 2021LYSEI025

Ecole doctorale : **Mécanique-Energétique-Génie Civil-Acoustique de Lyon**

Spécialité : **Acoustique**

RESUME :
Les polymères électroactifs (EAPs) trouvent de nombreuses applications en tant qu'actionneurs souples, compte tenu de leur légèreté, de grandes déformations sous champ électrique et de la facilité d'être élaborés sous diverses formes. Parmi les EAPs diélectriques, le polyuréthane est intéressant, de par ses propriétés diélectriques et mécaniques, un faible coût et des propriétés modulables via la composition et l'incorporation de charges.
Les travaux de recherche décrits dans cette thèse ont pour objectif une meilleure compréhension et un meilleur contrôle du comportement de films composites à base de polyuréthane.
La mesure du couplage mécanique est délicate et complexe. Une large gamme de valeurs du coefficient électromécanique, s'étalant sur plusieurs décades, est présentée pour le polyuréthane dans la littérature. Avec deux techniques de mesures (bancs de mesure développés au laboratoire) et des simulations Comsol, il a été obtenu des valeurs de coefficients sur une gamme beaucoup plus réduite, et indiquant un rôle considérable du mécanisme de Maxwell par rapport au phénomène d'électrostriction.
Des conditions d'élaboration et de mesures bien contrôlées sont importantes, en termes notamment de taux d'humidité et de niveaux de champs électriques.
Une étude a ensuite été menée sur le rôle des nanocharges sur les propriétés de composites polyuréthane / nanoplaquettes de graphène fonctionnalisé oxygène. Une augmentation de la constante diélectrique et un faible renforcement mécanique ont été obtenus, mais la performance électromécanique n'est pas améliorée. Les raisons possibles de ces résultats discordants ont été examinées avec des analyses multi-échelles. Une attention particulière a été portée sur les mécanismes de conduction et sur les polarisations dipolaires et interfaciale de type Maxwell Wagner Sillars. La faible performance peut venir de l'adhésion modérée entre le polymère et le graphène, mais aussi de la compétition entre l'augmentation de la constante diélectrique et la diminution du champ électrique réellement vu par le polymère.

MOTS-CLÉS :
Polymères électro-actifs, Polyuréthane, Graphène fonctionnalisé, Couplage électromécanique, Propriétés électriques, Nanocomposites, spectroscopie diélectrique

Laboratoire (s) de recherche : **Laboratoire de Génie Electrique et Ferroélectrique (LGEF) INSA de Lyon**

Directeur de thèse: **Pr. Laurent LEBRUN**
Co-directeur de thèse : **Dr. IGR. Laurence SEVEYRAT**

Président de jury : **Pr. Jean-Yves CAVAILLE**

Composition du jury : **Dr. Sophie BARRAU, MCF**
Pr. Philippe PAPET
Pr. Benoit GUIFFARD
Pr. Jean-Yves CAVAILLE
Dr. Laurence SEVEYRAT, IGR
Pr. Laurent LEBRUN